The Dissertation Committee for Emily Ann Dukes Brady Certifies that this is the approved version of the following Dissertation:

Plastic Flow and Microstructure Evolution in Niobium at Elevated Temperatures

Committee:

Eric M. Taleff, Supervisor

Desiderio Kovar

Filippo Mangolini

Carolyn C. Seepersad

Plastic Flow and Microstructure Evolution in Niobium at Elevated Temperatures

by

Emily Ann Dukes Brady

Dissertation

Presented to the Faculty of the Graduate School of

The University of Texas at Austin

in Partial Fulfillment

of the Requirements

for the Degree of

Doctor of Philosophy

The University of Texas at Austin

December 2021

Dedication

To my parents, who support and encourage me to strive for excellence in everything I do.

Acknowledgements

I am extremely grateful for my supervisor, Dr. Eric Taleff who in addition to guiding my graduate research, took great efforts to improve my presentation and technical writing skills and to teach me how to critically read technical papers. I am also thankful for my dissertation committee members, Dr. Desiderio Kovar, Dr. Filippo Mangolini, and Dr. Carolyn Seepersad. In the classes I took from them, they were excellent teachers. They also helped refine my research.

I would like to thank the National Science Foundation for funding this work through grants DMR-1507417 and DMR-2003312 and for the equipment from grant DMR-9974476. I would like to thank the Center for Integrated Nanotechnologies (CINT) for providing the facilities and expertise training to acquire some of the data presented in this study.

I would like to specially thank the developers and maintainers of OpenXY, especially Dr. David Fullwood and Tim Ruggles who helped me greatly in getting OpenXY to work with a new material and new EBSD system. I would also like to thank Andrew Marshell, Stephen Seddio, and Chris Stephens from Thermo Fisher Scientific who helped in getting the new EBSD system at the University of Texas at Austin working and providing the conversion equations for pattern center values between the Thermo Fisher Scientific software and OpenXY.

I would like to thank my parents, sister, and husband for all their love and support. Finally, I would like to give thanks and glory to God, who deserves all praise.

Abstract

Plastic Flow and Microstructure Evolution in Niobium at Elevated Temperatures

Emily Ann Dukes Brady, PhD

The University of Texas at Austin, 2021

Supervisor: Eric M. Taleff

Plastic flow and microstructure evolution are investigated at elevated temperatures in two unalloyed niobium sheet materials, Type 1 and Type 2 as designated in ASTM B393-18. Tensile tests are conducted at temperatures from 1473 to 1823 K (1200 to 1550°C) at constant true strain rates of 10^{-3} and 10^{-4} s^{-1}. Deformation microstructures are characterized using backscatter electron (BSE) imaging, electron backscatter diffraction (EBSD), and high-resolution EBSD (HR-EBSD). The mechanical behaviors of the Type 1 and Type 2 niobium materials are compared to relevant data from the literature. Elevated temperature deformation in both niobium materials is dominated by the five-power creep mechanism and the associated development of subgrains. The higher impurity content of the Type 2 niobium led to: 1. greater strength, 2. delayed recrystallization, 3. slower grain growth, 4. inhomogeneous microstructures, and 5. slower recovery which resulted in finer and less distinct subgrains compared to the Type 1 niobium. The smaller subgrain size of the Type 2 niobium produces, through the five-power creep mechanism, a higher strength at elevated temperature compared to the Type 1 niobium. This is the first mechanistic explanation supported by direct microstructural data for how impurity content affects

strength in refractory metals. HR-EBSD analysis is performed on the deformed Type 2 niobium material by developing new techniques to: 1. utilize data from a new EBSD instrument, 2. expand the capabilities of the OpenXY open-source cross-correlation software, and 3. enable cross correlation calculations spanning the breadth of heavily deformed grains. This is the first successful implementation of these techniques.

Table of Contents

List of Tables

List of Figures

Chapter 1: Introduction

Niobium is a body-centered cubic refractory metal with a melting temperature of 2741 K (2468 °C) [1]. Because of this high melting temperature, niobium and its alloys are of interest in technological applications, such as rocket nozzles and flame holders for jet engines [2]. For these applications the strength of niobium at elevated temperatures and the creep resistance of niobium are of great importance. An important aspect in the production of unalloyed refractory metals is the control of impurity content. Interstitial impurities such as C, O, and N, are of particular concern. Impurity content affects strength, ductility, and recrystallization behavior. Increasing impurity content is generally observed to increase the strength of refractory metals at elevated temperatures, even above the recrystallization temperature. This is an empirical observation that lacks an accepted mechanistic explanation supported by experimental data. The theories proposed for how impurities impact strength at elevated temperatures in refractory metals are solid solution strengthening and dispersion hardening [3]. W and Mo are thought to produce substitutional solid solution strengthening in niobium while carbides and/or oxides are thought to produce dispersion hardening [4]. A theory by Weertman [5] relates the creep rate to the amount of dispersion hardening present, where the creep rate is proportional to the square of the interparticle spacing between the dispersoids. Neither of these theories, solid solution strengthening nor dispersion hardening, are directly supported by microstructural data. A general goal of the present study is to improve understanding for

how impurity content affects microstructure development and strength at elevated temperature in refractory metals by studying niobium.

The available literature provides creep data for niobium over a limited range of temperatures and offers very little microstructural information from elevated temperature deformation. No creep data are available in the prior literature for unalloyed niobium above 1700 K (1427°C). The microstructural data available from prior literature for niobium after creep deformation indicate grain size, grain shape, dislocation networks, and the presence of substructure [6–9]. Unfortunately, none of the microscopy techniques used in the prior literature can distinguish between grain and subgrain boundaries, leaving these features poorly quantified prior to the present study. A detailed description of the creep data available in the prior literature for unalloyed niobium is provided in Chapter 2, and a detailed description of the available microstructure data in deformed niobium is provided in Chapter 3.

The substructure developed during deformation at elevated temperatures is critical to understanding the mechanisms of deformation. Electron backscatter diffraction (EBSD) and high-resolution EBSD (HR-EBSD) are especially useful techniques for distinguishing between grain and subgrain boundaries. EBSD is a microscopy technique that measures crystallographic lattice orientation by indexing Kikuchi patterns. To collect EBSD data, a sample is placed in a scanning electron microscope (SEM) and tilted to 70 degrees. An EBSD detector is placed very close to the sample, generally 1 to 2 cm from the sample [10]. The electron beam then raster scans across the sample. At each spot the beam touches,

backscattered electrons from the sample hit the EBSD detector and create a Kikuchi pattern. These Kikuchi patterns are imaged with a CMOS sensor or CCD camera, and a computer program correlates the Kikuchi patterns with the crystal lattice orientation at the scan spot. This technique can distinguish the misorientation between locations to an angular resolution of ± 0.5° [11–13]. High resolution EBSD is a post-processing data analysis technique that uses a cross-correlation method to improve the relative angular resolution of an EBSD scan to ± 0.01° [12]. This is of interest for distinguishing subgrain boundaries because subgrain boundaries can have misorientation angles even less than 0.01° [14]. The cross-correlation method takes a reference Kikuchi pattern from each grain and measures the small shifts in the pixels between the reference pattern and each Kikuchi pattern in the same grain [12,15,16]. This technique requires high quality Kikuchi patterns, and all the Kikuchi patterns from a scan must be saved for this analysis. The cross-correlation method is sensitive to the reference Kikuchi pattern used for the cross-correlation calculation. Therefore, it is important that the reference pattern be of good quality and similar to the other Kikuchi patterns within the same grain. If a microstructure has significant dislocation substructure, and therefore has grains in which the Kikuchi patterns vary significantly across the grain, multiple reference patterns within the grain must be used. The currently available software packages that perform HR-EBSD analysis are CrossCourt™ [17] and OpenXY [18]. The commercial CrossCourt software allows for multiple reference Kikuchi patterns in a single grain, but OpenXY currently allows only one reference pattern per grain. However, OpenXY is the only open-source software package that performs HR-EBSD analysis. The present study develops new procedures that

enable the use of OpenXY for HR-EBSD analysis from data produced using a new SEM/EBSD instrument at the University of Texas at Austin, a Thermo Fisher Scientific Scios 2 DualBeam SEM/FIB with a CMOS EBSD detector installed in the Texas Materials Institute.

The present study investigates two unalloyed niobium sheet materials, classified as Type 1 (reactor-grade) and Type 2 niobium (commercial purity) as defined in ASTM B393-18 [19]. These materials were chosen to investigate the effects impurities have on the deformation behavior and microstructure evolution in niobium, and to expand the available data in the literature for elevated temperature deformation of niobium. Tensile tests were conducted at temperatures from 1473 to 1823 K (1200 to 1550°C) for the Type 1 niobium and from 1473 to 1773 K (1200 to 1500°C) for the Type 2 niobium at constant true strain rates of 10^{-3} and 10^{-4} s^{-1} to true strains of 0.3, 0.4, or rupture. Static annealing tests were conducted from 1473 to 1773 K (1200 to 1500°C) in 100 K temperature steps, with the Type 1 niobium annealed for 67 minutes and the Type 2 niobium annealed for 65 minutes. Microstructural characterization was conducted for the statically annealed niobium and the deformed niobium for both materials. Backscatter electron (BSE) imaging, EBSD and HR-EBSD techniques were used to collect microstructural data. EBSD data were analyzed using MTEX [20], a Matlab toolbox. OpenXY [18], a Matlab toolbox, was used to perform the HR-EBSD analysis. The Type 1 and Type 2 niobium mechanical data are compared with unalloyed niobium creep data from the literature. The relationships between microstructure and deformation behavior, and microstructure and impurity content are

explored. These relationships are used to provide the first mechanistic explanation for how impurity content affects strength at elevated temperature in refractory metals.

Chapter 2: Plastic Deformation and Microstructure Evolution in Niobium at Temperatures from 1473 to 1823 K

The following chapter is after the article titled "Plastic Deformation and Microstructure Evolution in Niobium at Temperatures from 1473 K to 1823 K," by Emily A. D. Brady and Eric M. Taleff that was published in Metallurgical and Materials Transactions A in 2021 [21].

BACKGROUND

Niobium has a high melting point of T_M = 2741 ± 10 K (2468 ± 10°C) [1], making it a good candidate for high temperature structural applications. Its alloys are used for flame holders in jet engines and for rocket nozzles [2]. In these high temperature applications, mechanical stresses and temperatures at or above $0.4T_M$ produce creep deformation that affects performance and service life. Despite important technological applications, the creep behavior of niobium is only addressed in the literature across a limited range of temperatures. No published creep data are available for niobium above 1700 K (1427°C). Among the available literature there is little characterization of the microstructures produced by high temperature deformation. This study expands the available data by providing new tensile data for a low-impurity niobium sheet material (ASTM B393-18 Type 1) [19] at temperatures from 1473 to 1823 K (1200 to 1550°C). These data are used to identify the mechanism(s) responsible for plastic deformation. The microstructures produced by static exposure to elevated temperatures and by deformation at elevated temperatures are also characterized.

Creep data for unalloyed niobium are available in the literature from several investigations. For the present study, only data that are reported with the test temperature, stress, and either steady-state or minimum creep rate are considered. Behera *et al.* report compression creep data from niobium at temperatures from 973 to 1773 K (700 to 1500°C) [6]. Brinson and Argent report compression creep data from niobium at temperatures from 1223 to 1473 K (950 to 1200°C) [7]. Stoop and Shahinian report two studies on the tensile creep-rupture behavior of niobium [22,23]. Their first addresses the effects of oxygen impurities in niobium at temperatures from 1311 to 1700 K (1038 to 1427°C) [22]. Their second addresses the effects of nitrogen impurities in niobium at temperatures from 1200 to 1700 K (927 to 1427°C) [23]. Rawson and Argent report compressive and tensile creep data from niobium at temperatures from 1223 to 1478 K (950 to 1205°C) and the effects of oxygen and carbon impurities [8]. Klein and Gulden report tensile creep data from niobium at temperatures up to 1283 K (1010°C) [9]; they report obtaining creep data at higher temperatures, used to calculate activation energies, but do not provide those creep data. The following investigations address only temperatures below half the melting temperature of niobium. Lewis *et al.* report tensile creep data from fine-grained polycrystalline multilayered composite foils of niobium and copper at 873 K (600°C) and extract the creep behavior of the niobium from the composite data [24]. Gregory and Rowe report tensile creep data from niobium at temperatures ranging from 1144 to 1311 K (871 to 1038°C) [25]. Tottle reports creep data from niobium at 873 K (600°C) [26]. Williams and Heal [27] and Heal [28] report niobium creep data at

temperatures ranging from 673 to 873 K (400 to 600°C). Davidson *et al.* report niobium creep data at 1300 K (1027°C) [29].

The present study investigates the nature of plastic deformation and microstructure evolution in a low-impurity niobium sheet material (ASTM B393-18 Type 1) at elevated temperatures. Tensile tests are conducted at constant true-strain rates for temperatures from 1473 to 1823 K (1200 to 1550°C). Tensile data are used to investigate steady-state deformation, determine the mechanism(s) governing plastic flow, and evaluate plastic anisotropy. Microstructures are characterized after exposure to elevated temperatures under both static and dynamic conditions. Tensile test data and microstructure data are used to determine the mechanism(s) that control plastic deformation at elevated temperatures. Data from the present study are compared with data from the literature to determine global trends in the behavior of low-impurity niobium materials at elevated temperatures.

EXPERIMENTAL PROCEDURES

The material investigated is a niobium sheet meeting the ASTM B393-18 Type 1 standard requirements [19] and having a thickness of 0.508 ± 0.020 mm (0.020 ± 0.0008 in). Its chemical composition is presented in Table 2.1, as provided by the material supplier. Tensile specimens were fabricated in a dog-bone geometry with a gauge length of 25.4 ± 0.03 mm (1.00 ± 0.001 in) and a gauge width of 6.35 ± 0.03 mm (0.250 ± 0.001 in). Electrical discharge machining was used to produce each gauge region. Square grip regions were produced with sides of 19.1 ± 0.13 mm (0.75 ± 0.005 in) in length. A hole of 6.4 mm (0.25 in) diameter was centered in each grip region to accommodate a loading pin. The radius between the gauge and grip regions was held to 1.59 mm (0.063 in). To test for anisotropy within the sheet plane, specimens were excised from the sheet at 0, 90, and 45°

with respect to the rolling direction (RD), as shown in Figure 2.1. Tensile specimens were tested in uniaxial tension at temperatures ranging from 1473 to 1823 K (1200 to 1550°C) at constant true-strain rates of 10^{-3} and 10^{-4} s^{-1}. The 0 degree specimens were tested at temperatures from 1473 to 1823 K (1200 to 1550°C) in 50 K increments, while the 90 and 45 degree specimens were tested at 100 K increments between these same temperatures.

Specimens were tested in a high-temperature vacuum furnace attached to an electro-mechanical, ball-screw driven test machine with computer control to apply controlled loads and constant true-strain rates. Gauge length, width, and thickness were measured for each specimen prior to testing. A computer algorithm used the cross-sectional area of the gauge region, initial gauge length, and instantaneous crosshead displacement to control to a constant true-strain rate during tensile tests. The calculation of true strain for the algorithm assumed constant volume and uniform deformation in the gauge length, *i.e.*, no necking. The initial gauge length at the test temperature was calculated using a linear thermal expansion coefficient of $\alpha = 7.1\times10^{-6}$ K^{-1} [30] to account for thermal expansion during heating. Metal bellows sealed the top and bottom of the furnace with the load train passing through the center of each bellows. Tungsten pull rods were used in the hot zone to withstand the high temperatures. Silicon carbide loading pins attached the specimens to the pull rods. Tungsten heating elements produced the elevated temperatures for testing. Furnace temperature was controlled using a thermocouple located separately from the specimen. Calibration experiments were conducted to measure temperature as a function of position within the furnace hot zone where the specimen resides during testing. The

resulting calibration data were used to determine setpoints for furnace control and to estimate the uncertainty in specimen temperature, which is approximately ± 10 K.

Table 2.1: Chemical compositions for the niobium material (ASTM B393-18 Type 1) [19] of the present study and materials reported in the literature are in ppm by weight; balance is Nb. Author(s), temperature ranges, and strain rates are reported.

Sym.	Author(s)	Temp. Range (°C)	Strain Rates (s^{-1})	C	N	O	H	Zr	Ta	Fe	Si	W	Ni	Mo	Hf	Ti	Al
●	Present Study	1200 to 1550	$1x10^{-4}$ to $1x10^{-3}$	9	60	73	3	5	300	5	10	33	<5	<10	10	<5	
◁	Behera et al. [6]*	1100 to 1500	$3x10^{-3}$ to 1					1000		800							500
○	Brinson and Argent [7]*	1100 to 1200	$1.5x10^{-7}$ to $3.6x10^{-7}$	40	50	70 to 120	0	0	1000	50	100	300	0	0	0	0	
◇	Stoop, J. and Shahinian, P. [23]	1260 to 1427	$8.9x10^{-7}$ to $4.9x10^{-6}$	<10	45	26	<5	<100	<500	<50	<50	<100	<20	<20	<100	<50	
▷	Stoop, J. and Shahinian, P. (Heat CH) [22]	1260 to 1427	$9.72x10^{-7}$ to $1.28x10^{-4}$	20	11	25	0.8		530	10	<10	400	<10	30			
▽	Rawson, J.D.W. and Argent, B.B. [8]**	1100 to 1205	$6.52x10^{-8}$ to 5.09×10^{-7}			70 to 130											

*data from compression tests

**data from compression and tensile tests

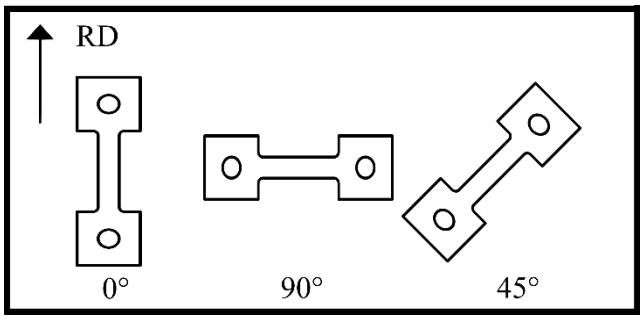

Figure 2.1: Specimen orientations are shown with respect to the sheet rolling direction (RD).

All specimens were tested in a vacuum of approximately 10^{-6} torr to reduce the oxidation of the niobium. After the desired vacuum level was reached, a load of 22 N was applied while heating to the test temperature. Heating to the test temperature occurred in approximately 15 minutes. The 22 N load was sufficient to overcome the force from the bellows under vacuum and provide a small tensile load to the specimen. The specimen was soaked at the test temperature under this small load for one hour. Soaking the specimen at the test temperature allowed the specimen to recrystallize and the pull rods to complete thermal expansion before tensile straining. The recrystallization temperature for niobium ranges from 1123 to 1573 K (850 to 1300°C) [30]. Impurity content and the degree of cold deformation prior to recrystallization can affect the recrystallization temperature. This large recrystallization temperature range is likely because of differences in impurity content and/or the degree of cold deformation in the materials studied. After soaking at temperature, a single true-strain rate was applied until a total strain of 0.2, 0.3, 0.4, or rupture was reached. Load and displacement data were collected during tensile straining. Upon completion of tensile straining, the furnace was turned off. The furnace system

cooled to 873 K (600°C) within 10 minutes. While cooling with specimens that did not rupture, a load of 22 N was applied until the temperature fell to 303 K (30°C). This small load was intended to preserve subgrains and related dislocation structures produced during high-temperature deformation. Faster cooling would better preserve these microstructural features but was not possible because of the vacuum environment. Data from independent calibration experiments were used to correct load data for the force produced by the bellows on the load train under vacuum. Extension data were corrected for elastic deflection of the load train using specimen stiffness calculated from the dynamic, temperature-dependent, unrelaxed elastic modulus of niobium extracted from the published literature and described in the Discussion section. True stress and true strain were then calculated. Some specimens exhibited elongation of the loading pin holes after testing. This accounted for a maximum of 6% but typically less than 4% of the final true strain calculated. Because this effect was small, no corrections were applied for it. The absolute uncertainty in measured stress was estimated to be ± 2 MPa. The relative uncertainty in measured stress between specimens is likely smaller than this.

In addition to elevated temperature uniaxial tension tests, static annealing experiments were conducted at temperatures of 1473, 1573, 1673, and 1773 K (1200 to 1500°C) in vacuum on square specimens excised from the niobium sheet material. Specimens were suspended within the vacuum furnace and held at temperature for 67 minutes, the same time at temperature as the specimens tested at a constant true-strain rate

of 10^{-3} s^{-1} to a true strain of 0.4. These specimens were used to study recrystallization and static grain growth as functions of temperature.

After testing at elevated temperature, specimens were sectioned and mounted for metallographic observation. Silicon carbide papers to 1200 grit were used for grinding, and diamond suspensions to 1 μm were used for polishing. A solution of colloidal silica and hydrogen peroxide (5:1 ratio by volume) was used for the final polish. Photomicrographs were acquired in a scanning electron microscope (SEM) using backscatter electron (BSE) imaging at a voltage of 5 kV and a working distance of 15 mm. The BSE photomicrographs were used to measure the lineal-intercept grain size and the grain aspect ratio as described in ASTM E112-13 [31].

RESULTS

Tensile Tests

Figure 2.2 shows representative stress-strain curves for the niobium sheet material (ASTM B393-18 Type 1) from 1473 to 1823 K (1200 to 1550°C). Tensile data from the 0 degree specimen orientation are plotted as true stress against true strain at a constant true-strain rate of 10^{-3} s^{-1}. The flow stress values at 0.3 true strain are shown as filled circles in Figure 2.2. These are used for a subsequent steady-state creep analysis and are provided in Table 2.2 as $\sigma_{0.3}$. Flow stress decreases as test temperature increases. Flow stress is steady from 0.3 to 0.4 true strain for temperatures between 1473 and 1823 K (1200 and 1550°C) across the strain rates investigated, except for a few cases of early flow localization, such as the 1723 K (1450°C) test shown in Figure 2.2 and noted in Table 2.2. Unlike most room-temperature deformation, strain-rate hardening dominates at elevated temperatures, and a

steady flow stress does not necessarily imply that a neck (flow localization) is developing. All specimens were inspected after tensile testing, and no significant necking was observed in specimens that did not rupture. A representative non-ruptured specimen, shown in Figure 2.3, demonstrates that no significant necking occurred during tensile testing. Table 2.2 presents a summary of the tensile data acquired for this investigation. Specimen orientation (θ), test temperature (T), and constant true-strain rate ($\dot{\varepsilon}$) are tabulated for each specimen. The final true strain, ε_f, imposed in each test is provided. Measurements of specimens after testing demonstrate that the desired true tensile strain for each test was achieved to within ± 10% or better, except when early flow localization or rupture occurred, which is noted in Table 2.2. The flow stress values at true strains of 0.2, 0.3, and 0.35 ($\sigma_{0.2}$, $\sigma_{0.3}$, and $\sigma_{0.35}$) are provided for quantitative comparison. Figure 2.4 presents the effect of strain rate on flow stress at 1473 and 1773 K (1200 and 1500°C). Tensile data for the 0 degree specimen orientation are plotted as true stress against true strain for temperatures of 1473 and 1773 K (1200 and 1500°C) at constant true-strain rates of 10^{-3} and 10^{-4} s^{-1}. Flow stress decreases with decreasing strain rate and increasing temperature, as expected.

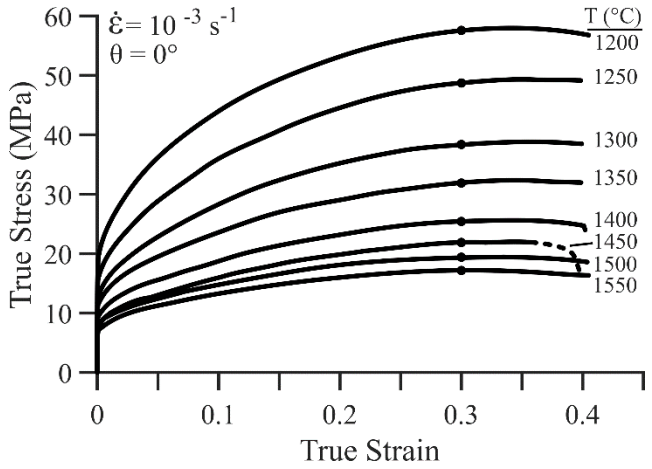

Figure 2.2: Tensile data for the 0 degree specimen orientation tested at a constant true-strain rate of 10^{-3} s^{-1} and temperatures from 1473 to 1823 K (1200 to 1550°C) are plotted as true stress against true strain. Flow localization occurred before the end of the tests at temperatures of 1673 and 1723 K (1400 and 1450°C). Black dots on the curves mark the true stress values used for steady-state creep analysis.

Table 2.2: Tensile data for temperatures from 1473 to 1823 K (1200 to 1550°C) and strain rates of 10^{-3} and 10^{-4} s^{-1} are reported with average flow stress values at true strains of 0.2, 0.3 and 0.35.

θ (°)	T (°C)	T(K)	$\dot{\varepsilon}(s^{-1})$	ε_f	$\sigma_{0.2}$ (MPa)	$\sigma_{0.3}$ (MPa)	$\sigma_{0.35}$ (MPa)
0	1550	1823	1×10^{-4}	0.2	10	–	–
0	1550	1823	1×10^{-4}	**0.4	11	10	4
0	1500	1773	1×10^{-4}	0.4	13	13	13
0	1450	1723	1×10^{-4}	*0.4	15	15	15
0	1400	1673	1×10^{-4}	*0.4	16	17	17
0	1350	1623	1×10^{-4}	0.4	20	21	21
0	1300	1573	1×10^{-4}	0.4	25	27	27
0	1250	1523	1×10^{-4}	0.4	31	33	33
0	1200	1473	1×10^{-4}	0.4	38	40	39
0	1550	1823	1×10^{-3}	0.4	16	17	17
0	1500	1773	1×10^{-3}	0.4	18	19	19
0	1450	1723	1×10^{-3}	*0.4	20	22	22
0	1400	1673	1×10^{-3}	0.4	23	25	26
0	1350	1623	1×10^{-3}	0.4	29	32	32
0	1300	1573	1×10^{-3}	0.4	35	38	39
0	1250	1523	1×10^{-3}	0.4	44	49	49
0	1200	1473	1×10^{-3}	0.4	53	58	58
90	1500	1773	1×10^{-3}	0.4	15	16	16
90	1400	1673	1×10^{-3}	0.4	22	24	24
90	1300	1573	1×10^{-3}	0.4	33	36	36
90	1200	1473	1×10^{-3}	0.4	56	60	60
45	1500	1773	1×10^{-3}	*0.4	16	17	17
45	1400	1673	1×10^{-3}	0.4	21	22	22
45	1300	1573	1×10^{-3}	0.4	30	33	33
45	1200	1473	1×10^{-3}	0.4	50	55	55
90	1500	1773	1×10^{-3}	0.3	16	17	–
90	1500	1773	1×10^{-3}	0.3	16	16	–
90	1400	1673	1×10^{-3}	0.3	24	27	–
45	1500	1773	1×10^{-3}	0.3	17	18	–
90	1500	1773	1×10^{-2}	0.3	22	24	–
45	1500	1773	1×10^{-2}	0.3	23	25	–

* flow localization before test ended

** flow localization and rupture before test ended

Figure 2.3: A Type 1 niobium tensile specimen is shown before and after testing at 1673 K (1400°C) at a constant true-strain rate of 10^{-3} s^{-1} to a total true strain of 0.4. This specimen is representative of non-ruptured specimens and exhibits no significant necking.

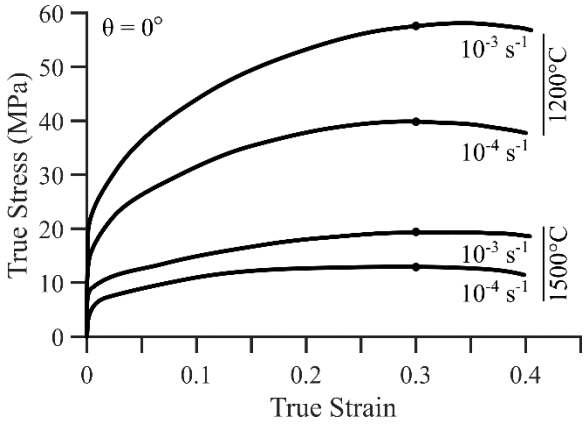

Figure 2.4: Tensile data for the 0 degree specimen orientation tested at 1473 and 1773 K (1200 and 1500°C) at constant true-strain rates of 10^{-3} and 10^{-4} s^{-1} are plotted as true stress against true strain. Black dots on the curves mark the true stress values used for steady-state creep analysis.

Figure 2.5 probes plastic anisotropy within the sheet plane. Tensile data for 0, 90 and 45 degree specimen orientations are plotted as true stress against true strain at a constant true-strain rate of 10^{-3} s^{-1} for temperatures of 1473 and 1773 K (1200 and 1500°C). For all orientations, a rise in test temperature causes flow stress to decrease. Data from Figure 2.5 and Table 2.2 demonstrate that the flow stress for the 45 degree orientation is consistently lower than the 0 and 90 degree orientations at temperatures of 1673 K

(1400°C) and lower. For temperatures of 1573 K (1300°C) and higher, the flow stress for the 0 degree orientation is consistently higher than the 90 and 45 degree orientations. The maximum difference in flow stress with specimen orientation at 1473 K (1200°C) is twice the absolute uncertainty in stress measurement, which is estimated to be 2 MPa. At 1773 K (1500°C), the differences in flow stress with specimen orientation are either within or only slightly greater than the absolute uncertainty in stress measurement. These results indicate that any plastic anisotropy is small, particularly at the highest test temperatures. However, the small differences observed between orientations, demonstrated in Figure 2.5 and Table 2.2, could also be caused by variations in material behavior between the different locations within the original niobium sheet from which specimens were extracted.

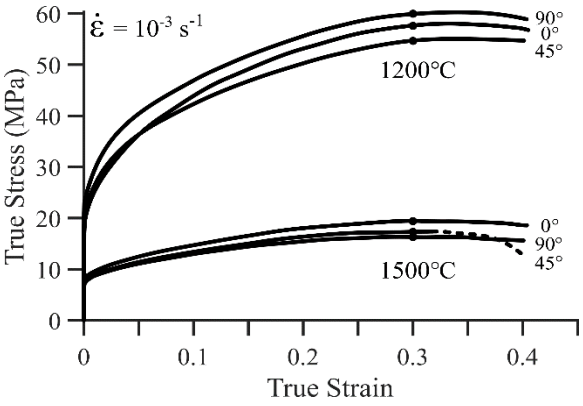

Figure 2.5: Tensile data for 0, 90, and 45 degree specimen orientations tested at 1473 and 1773 K (1200 and 1500°C) at a constant true-strain rate of 10^{-3} s^{-1} are plotted as true stress against true strain. Black dots on the curves mark the true stress values used for steady-state creep analysis.

Microstructure

Figure 2.6 compares the microstructures of the statically annealed and deformed specimens using BSE images. The deformed specimens have the 0 degree orientation and were tested at a constant true-strain rate of 10^{-3} s^{-1} to a true strain of 0.4. The statically

annealed specimens were annealed for the same time, 67 minutes, as the deformed specimens were at temperature. Statically annealed specimens are on the top row, and deformed specimens are on the bottom row. Each column presents a constant test temperature. The lineal-intercept grain size, *d*, measured for each static annealing condition is reported in Figure 2.6 [31]. The grain size in the specimen statically annealed at 1773 K (1500°C) is more than triple that of the specimen annealed at 1473 K (1200°C). The statically annealed specimens have equiaxed grains. The average grain aspect ratio is within the range of 0.9 to 1.1 for all the statically annealed specimens [31].

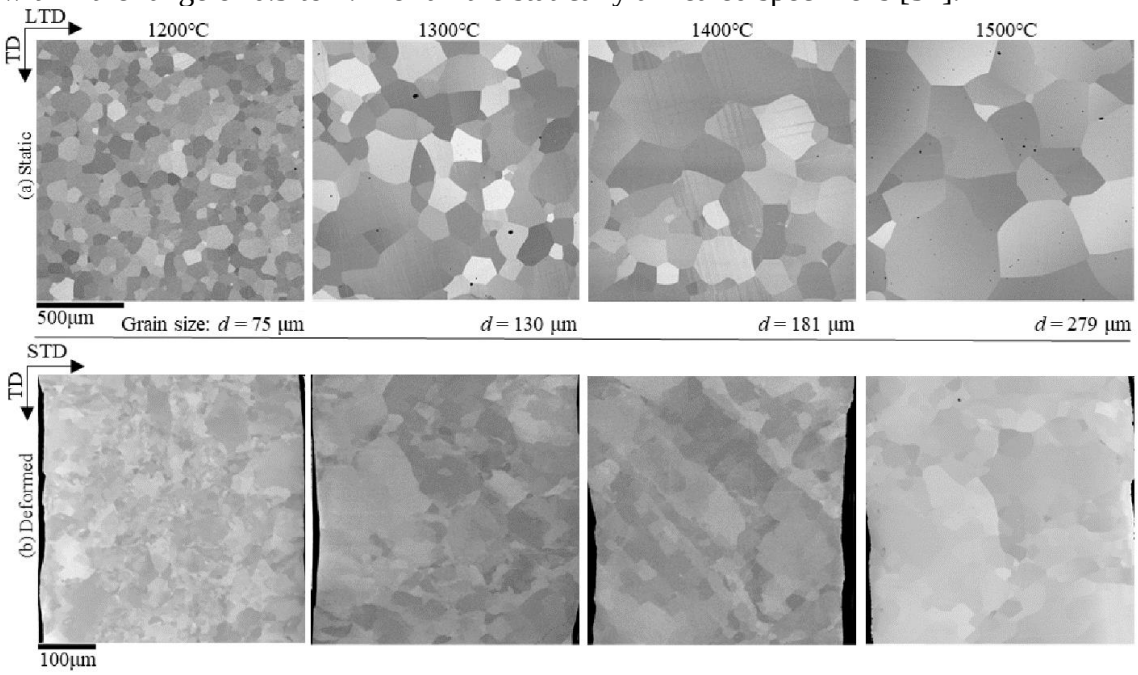

Figure 2.6: These BSE images show (a) statically annealed niobium (top row) and (b) niobium tensile tested (bottom row) in the 0 degree orientation at temperatures from 1473 to 1773 K (1200 to 1500°C). Tensile specimens were tested at a constant true-strain rate of 10^{-3} s^{-1} to a true strain of 0.4. Annealed specimens were held at temperature for the same time as the tensile-tested specimens, 67 minutes. The tensile direction (TD) and the long-transverse direction (LTD) of the sheet are shown for the static specimens. The TD and the short transverse direction (STD) are shown for the deformed specimens.

In the deformed specimens a substructure consisting of subgrains and/or related dislocation structures is apparent. Such substructure is an expectation for five-power creep [32]. Brinson and Argent [7] and Stoop and Shahinian [22] observed subgrains in some niobium specimens after creep testing. Brinson and Argent observed abnormally large grains without internal substructure in specimens tested at temperatures 1273 to 1473 K (1000 to 1200°C) [7]. That observation might be consistent with dynamic abnormal grain growth [33–37]. It is not clear whether abnormal grains were produced in the present investigation. Because BSE imaging cannot reliably distinguish between grain and subgrain boundaries, the grain sizes in the deformed specimens could not be measured. Future studies will use electron backscatter diffraction (EBSD) mapping to overcome this issue. The deformed specimen microstructures exhibit grains/subgrains that vary drastically in size and shape, making their microstructures distinct from those in the statically annealed specimens. In the specimen deformed at 1673 K (1400°C), boundaries appear to be aligned along a 45 degree angle to the tensile direction (TD), perhaps suggesting slip bands. Slip lines were observed in the niobium material tested by Brinson and Argent [7].

DISCUSSION

To better understand the creep behavior of low-impurity niobium, a steady-state creep analysis is pursued. A steady flow stress at constant temperature and true-strain rate is taken to represent an approximately steady-state condition. At all test temperatures the flow stress becomes steady by approximately a true strain of 0.3. The applicability of steady state is evaluated by comparing the flow stresses at $\varepsilon = 0.3$ and 0.35, as reported in Table 2.2. The difference in flow stress between these two strains is consistently less than the absolute uncertainty in stress measurement, approximately ± 2 MPa. Considering all

experiments without early rupture, the maximum difference in flow stress between these two strains is 1.9%. This indicates that it is reasonable to attempt a steady-state creep analysis.

The stress exponent and activation energy for creep at the temperatures and strain rates investigated are determined and compared with values from the literature to explore the mechanism(s) responsible for deformation in low-impurity niobium. The phenomenological equation for steady-state creep is used to determine the stress exponent, n, and the activation energy for steady-state creep, Q_c. The phenomenological equation for steady-state creep is, [32,38,39]

$$\dot{\varepsilon} = A\left(\frac{\sigma}{E}\right)^n exp\left(-\frac{Q_c}{RT}\right), \qquad (2.1)$$

where $\dot{\varepsilon}$ is the true-strain rate, A is a material dependent parameter, σ is the flow stress in the same units as E, E is the temperature-dependent unrelaxed dynamic Young's elastic modulus, R is the universal gas constant, and T is temperature in Kelvin. To calculate activation energy using Equation 2.1, the unrelaxed-dynamic elastic modulus as a function of temperature is needed.

All the data available in the literature for the Young's elastic modulus of polycrystalline niobium are gathered and plotted in Figure 2.7 as a function of absolute temperature [23,26,27,40–46]. Table 2.3 summarizes these data and provides the key for symbols used in Figure 2.7. Techniques used to measure the elastic modulus of niobium are categorized in Table 2.3 as dynamic, quasistatic, and unspecified. Elastic moduli measured using dynamic techniques are plotted as filled symbols in Figure 2.7. Quasistatic and unspecified techniques are plotted as open symbols, except the data from Hazelton. Hazelton only reports elastic modulus as a straight line plotted against temperature [46], and these data are similarly presented as a straight dashed line in Figure 2.7. Quasistatic

techniques do not separate time-dependent effects, such as anelasticity and time-dependent plasticity, from the elastic modulus and produce values erroneously lower than those measured by dynamic techniques, particularly at elevated temperature. This error is evident in the quasistatic elastic modulus data at elevated temperatures, and Tottle's data are the most extreme case. Time-dependent effects may be negligible at room temperature but become increasingly significant as temperature increases. For this reason, only data from dynamic measurements are considered above room temperature.

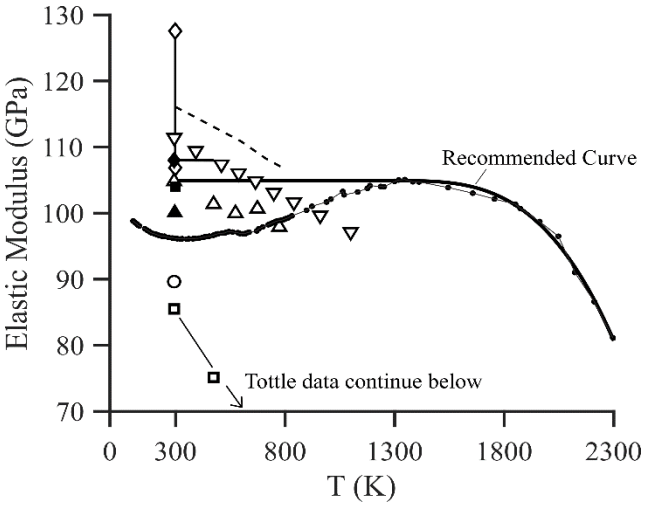

Figure 2.7: Elastic modulus data for polycrystalline niobium are plotted as a function of absolute temperature. A recommended curve for the unrelaxed, temperature-dependent dynamic elastic modulus is shown. Symbols are defined in Table 2.3.

Niobium is a very elastically anisotropic body-centered-cubic (BCC) crystal at room temperature, with an anisotropy ratio of 1.99 according to data from References [47–50]. This high anisotropy ratio provides an explanation for the wide range of elastic moduli reported at room temperature. The directionally dependent elastic modulus of single-crystal niobium at room temperature varies from 80.7 GPa along the <111> to 152 GPa along the <100> [47]. The elastic moduli reported for polycrystalline niobium at room

temperature in Figure 2.7 are between these bounding values. This suggests that the wide variation in elastic moduli reported for polycrystalline niobium at room temperature is likely a result of differences between the crystallographic textures of the materials tested.

Table 2.3: Tensile data for temperatures from 1473 to 1823 K (1200 to 1550°C) and strain rates of 10^{-3} and 10^{-4} s^{-1} are reported with average flow stress values at true strains of 0.2, 0.3 and 0.35.

Symbol	Author (s)	Temperature Range (K)	Technique	Notes
	Armstrong, P.E. and Brown, H.L. [40]	106 to 2296	dynamic	Strong [110] recrystallization texture along rod axis
	Livesey, D. J. [41]	293 to 473	dynamic	
	Reynolds, M. B. [42]	298	dynamic	
	Wriedt, H.A. and Oriani, R.A. [43]	296	dynamic	
	Laverty, D.P. and Evans, E.B. [44]	294 to 1099	quasistatic	
	Tottle, C. R. [26]	293 to 823	quasistatic	
	Harwood, J.J [45]	298	unspecified	
	Hazelton, W.S. [46]	298 to 793	unspecified	
	Stoop, J. and Shahinian, P. [23]	298	unspecified	
	Williams, L.R. and Heal, T.J. [27]	293 to 773	unspecified	

The data in Figure 2.7 from dynamic measurements are used to determine temperature-dependent values for the unrelaxed, dynamic, temperature-dependent Young's elastic modulus of polycrystalline niobium. Considering the effects of texture on

the measurement of elastic modulus at room temperature, the value of 104.9 GPa recommended in Reference [47] is adopted for room temperature. Livesey [41] reports elastic modulus values up to 473 K (200°C), and Armstrong and Brown [40] report elastic modulus values up to 2296 K (2023°C), both using dynamic measurement techniques. As temperature increases above 300 K (27°C) the anisotropy ratio for niobium decreases [47–50]. The most likely reason for the low elastic modulus reported near room temperature by Armstrong and Brown [40] is the strong <110> fiber texture in the material used for their measurements. Texture becomes less important as temperature increases because anisotropy decreases. The elastic modulus increase reported by Armstrong and Brown up to 1300 K (1027°C) is likely a result of the decreasing elastic anisotropy of niobium with increasing temperature. Thus, this change in elastic modulus from 300 to 1300 K (27 to 1027°C) is not representative of randomly textured polycrystalline material. In creating a recommended elastic modulus curve for randomly textured polycrystalline niobium as a function of temperature, the slope between room temperature and 1300 K (1027°C) is interpreted as zero. At 1300 K (1027°C) the Armstrong and Brown values for elastic modulus reach approximately 104.9 GPa and then begin to decrease with increasing temperature. From 293 to 1300 K (20 to 1027°C), the room temperature elastic modulus of 104.9 GPa is recommended [47]. At 1300 K (1027°C) and above, the recommended modulus curve is fit to Armstrong and Brown's data, which are the only data available at these temperatures. The recommended temperature-dependent, unrelaxed, dynamic Young's elastic modulus above 1300 K (1027°C) is,

$$E = 104.9 - 8.3513\times10^{-9}\,(T - 1300)^{3.154}\,, \qquad (2.2)$$

where elastic modulus, E, is in GPa and temperature, T, is in Kelvin. This equation for the unrelaxed, dynamic elastic modulus is recommended for temperatures from 1300 to 2300 K (1027 to 2027°C).

To measure the stress exponent, true-strain rate is plotted against true stress normalized by the temperature-dependent, unrelaxed, dynamic elastic modulus on dual logarithmic scales in Figure 2.8. The slope of the data in Figure 2.8 at a constant temperature is the stress exponent, n. The stress exponent ranges from 6.5 at 1573 K (1300°C) to 4.1 at 1823 K (1550°C). These stress exponents straddle the value expected for pure metals undergoing steady-state dislocation climb creep, n = 5 [32,39], also known as five-power creep. To calculate the activation energy for creep, the natural logarithm of true-strain rate is plotted against the inverse of absolute temperature in Figure 2.9 for data at constant σ/E. The strain rates plotted in Figure 2.9 were determined using the constant temperature curves in Figure 2.8 at the constant σ/E values noted in Figure 2.9. The slope of each curve in Figure 2.9 is $-Q_c/R$. The average activation energy calculated from Figure 2.9 is 454 kJ/mol.

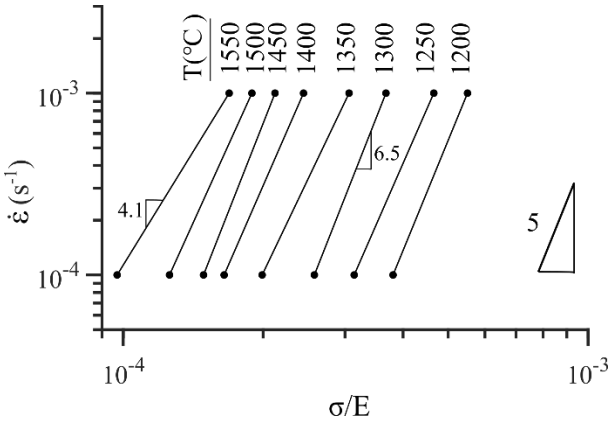

Figure 2.8: Data from the 0 degree specimen orientation are plotted as true-strain rate against true stress normalized by the temperature-dependent, unrelaxed dynamic elastic modulus on dual logarithmic scales. The slopes of these data provide the stress exponent for creep, which varies from n = 4.1 to 6.5.

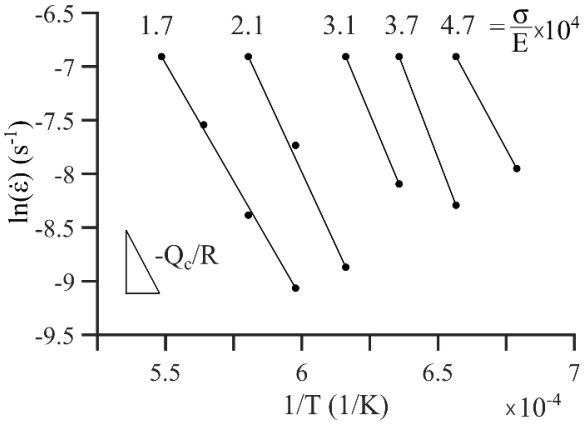

Figure 2.9: The natural logarithm of true-strain rate is plotted against the inverse of absolute temperature for constant *σ/E* values. The slopes of these data are proportional to the activation energy for creep.

Activation energies for creep from literature are compared in Figure 2.10 with the activation energies measured in the present study [7–9,22,24,25,51]. The horizontal line at 454 kJ/mol is the average value of the activation energies from the present study. This is close to the activation energy for lattice self-diffusion in niobium, which is approximately

440 kJ/mol [47]. A wide range of values for activation energy are reported in the literature; these are bounded by the dotted curves in Figure 2.10. Such a wide range of values may be a result of differences in impurity levels for the various niobium materials. Brinson and Argent observed abnormally large grains during some experiments, meaning that a constant microstructure was not maintained during testing [7]. Because of this change in microstructure, Brinson and Argent could not calculate reliable activation energies and instead calculated apparent activation energies, which are reported in Figure 2.10 [7]. The activation energies near 700 kJ/mol reported by Klein and Gulden are outliers not included in the bounding curves [9]. Klein and Gulden considered these activation energies to be unrealistically high and likely caused by unusual creep behavior associated with dynamic strain aging [9]. The datum from Behera et al. is an outlier on the low end of activation energies [6]. A general decrease in activation energy is observed at temperatures below half the melting temperature. The melting temperature of niobium is T_M = 2741 ± 10 K (2468 ± 10°C) [1]. The drop in activation energies below $0.5T_M$, marked by a vertical dashed line, likely indicates a change in creep mechanism.

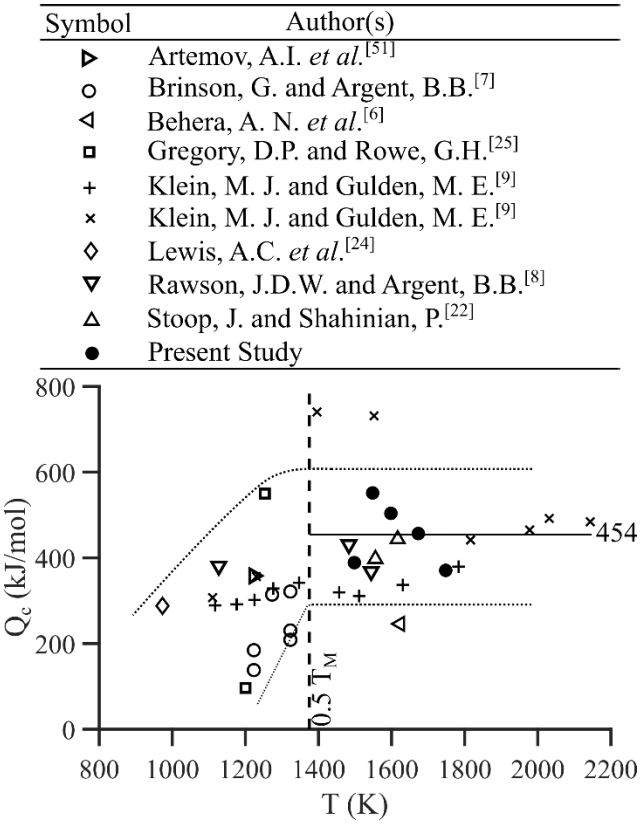

Figure 2.10: Activation energies for the creep of polycrystalline niobium reported in the literature and measured in the present study are plotted as a function of absolute temperature.

In Figure 2.11, the Zener-Hollomon parameter is plotted against stress normalized by the temperature-dependent, unrelaxed, dynamic elastic Young's modulus on dual logarithmic scales for the 0 degree specimen orientation. The Zener-Hollomon parameter is defined as [52],

$$Z = \dot{\varepsilon}\ exp\left(\frac{Q_c}{RT}\right), \qquad (2.3)$$

where Q_c is 454 kJ/mol. The slope of these data, n = 5.59, is a measure of the stress exponent for steady-state creep across the temperatures and strain rates investigated. The result of fitting Equation 2.1 to the data in Figure 2.11 is,

$$\dot{\varepsilon} = 1.82 \times 10^{31} \left(\frac{\sigma}{E}\right)^{5.59} exp\left(\frac{-Q_c}{RT}\right) . \qquad (2.4)$$

Equation 2.4 is plotted as a solid line in Figure 2.11.

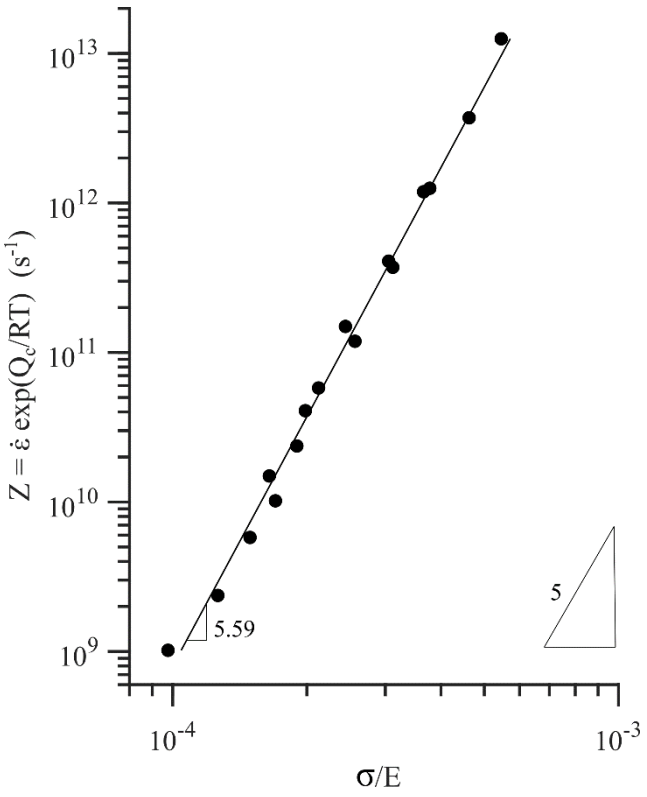

Figure 2.11: Tensile data for the 0 degree specimen orientation at temperatures from 1473 to 1823 K (1200 to 1550°C) and strain rates of 10^{-3} and 10^{-4} s^{-1} are plotted as Z (Zener-Hollomon parameter) against true stress normalized by the temperature dependent, unrelaxed dynamic elastic modulus on dual logarithmic scales. The slope of these data, 5.59, is the stress exponent for creep.

To compare the data from the present study to data available in the literature, the independently measured lattice diffusivity is used to normalize true-strain rate, $\dot{\varepsilon}$. The lattice self-diffusion coefficient used is that reported in Reference [47] as:

$$D = 8 \times 10^{-7} exp\left(\frac{-Q_1}{RT}\right) + 3.7 \times 10^{-4} exp\left(\frac{-Q_2}{RT}\right) , \qquad (2.5)$$

where D is diffusivity in m^2/s, Q_1 is 349.6 kJ/mol, and Q_2 is 438.4 kJ/mol. This equation for diffusivity is for temperatures from 1353 to 2693 K (1080 to 2420°C).

Figure 2.12 compares data from this study with relevant data from the literature by plotting true-strain rate normalized by diffusivity against true stress normalized by the temperature-dependent, unrelaxed, dynamic Young's elastic modulus on dual logarithmic scales [7,8,22,23]. The authors, temperatures, strain rates, and material compositions for these data are presented with corresponding symbols in Table 2.1. All the strain rates reported in the literature are slower than the strain rates investigated in the present study, except for the data from Behera *et al.* [6], which reports faster strain rates than the present study. The present investigation uses niobium sheet material, while most of the data from literature are from niobium rod material. Only Rawson and Argent tested niobium sheet material [8]. None of the niobium rod materials tested in the literature meet the impurity standards for ASTM B392-18 Type 1 niobium rod [53]. Notable differences in impurities are evident in carbon, tungsten, iron, zirconium, and silicon content. The niobium material investigated by Behera *et al.* [6] contains a much higher impurity content than the other materials from the literature listed in Table 2.1. These data are plotted in Figure 2.12 for comparison, but were not used to produce the fitted line. Data from the literature for materials with oxygen impurities higher than 0.02 wt% and nitrogen impurities high enough to create a two-phase microstructure are not included. The nitrogen impurity level necessary to create a two-phase microstructure ranges from approximately 0.1 to 0.4 wt%, depending on test temperature [23]. Such high levels of oxygen and nitrogen reduce the creep rate and are not indicative of the creep behavior for low-impurity niobium [22,23]. Only data for temperatures greater than $0.5T_M$ are included in Figure 2.12. Data from the literature are plotted as hollow symbols. Fitting a modified phenomenological equation for creep to the data of Figure 2.12 produces,

$$\frac{\dot{\varepsilon}}{D} = (9.55 \times 10^{28} m^{-2}) \times \left(\frac{\sigma}{E}\right)^{4.23}, \quad (2.6)$$

where $\dot{\varepsilon}$ is the true-strain rate in s^{-1}, and D is the lattice self-diffusivity in m^2/s. Equation 2.6 is plotted as a solid line in Figure 2.12. This line demonstrates a slope of $n = 4.23$, which is reasonably close to the expected stress exponent for creep in pure metals, $n = 5$. The data presented in Figure 2.12 are consistent with deformation by five-power creep, also known as dislocation climb-controlled creep [32,38,39].

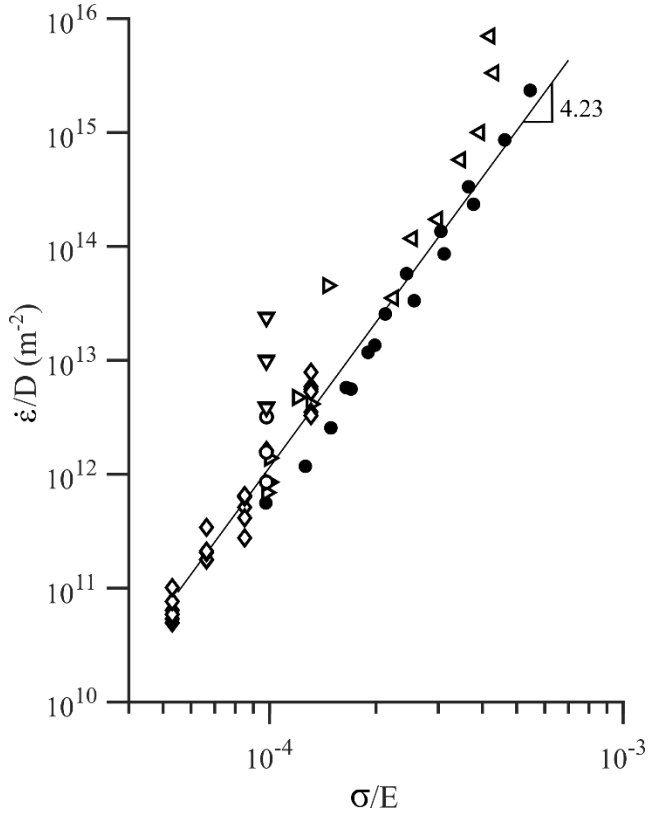

Figure 2.12: Data from the literature are plotted with data from the present study as the true-strain rate normalized by the independently measured lattice self-diffusivity, from Reference [47], against the true-stress normalized by the temperature dependent, unrelaxed dynamic elastic Young's modulus on dual logarithmic scales. Symbols are defined in Table 2.1.

CONCLUSIONS

Elevated temperature tensile tests are used to determine the mechanism responsible for deformation of low-impurity niobium sheet material at elevated temperatures. These tensile data are compared to the available, relevant data from the literature. Microstructures from static annealing and from deformation at elevated temperatures are reported and characterized. The following conclusions are drawn:

1. A compilation of all available data in the literature for the Young's elastic modulus of polycrystalline niobium is used to recommend dynamic, unrelaxed Young's elastic modulus values from room temperature up to 2300 K (2027°C) for randomly textured polycrystalline niobium. A value of 104.9 GPa is recommended from room temperature up to 1300 K (1027°C). Recommended values above 1300 K (1027°C) are given by Equation 2.2.
2. The variation of flow stress with tensile direction within the sheet plane of the niobium material is negligible at 1773 K (1500°C). For temperatures of 1673 K (1400°C) and lower, the flow stress for the 45 degree specimen orientation is slightly less than the 0 and 90 degree specimen orientations.
3. At temperatures of $0.5T_M$ and higher, the average activation energy for creep is 454 kJ/mol. This value is consistent with activation energies reported for creep in the literature (Figure 2.10) and the activation energy for lattice self-diffusion [47]. Below $0.5T_M$, the values from literature indicate a decreasing activation energy with decreasing temperature.

4. Data from the present study plotted in Figure 2.11 as the Zener-Hollomon parameter *versus* σ/E on dual logarithmic scales produce a stress exponent of 5.59 for temperatures from 1473 to 1823 K (1200 to 1550°C).

5. Data from the present study and the literature collapse onto nearly a single curve when $\dot{\varepsilon}/D$ is plotted as a function of σ/E using dual logarithmic scales in Figure 2.12, where D is the independently measured coefficient for lattice self-diffusion in niobium [47].

6. Dislocation substructure and/or subgrains are apparent in the deformed niobium. Subgrains are expected for five-power creep [32,39].

7. Based on the stress exponent, the activation energy for creep, the presence of substructure following deformation, and comparisons with data from the literature, the deformation of low-impurity niobium is by five-power creep for the strain rates and temperatures investigated.

8. Significant static grain growth is observed in the niobium material. Recrystallization and grain growth during annealing for 67 minutes at 1773 K (1500°C) produces a grain size more than triple that produced by annealing at 1473 K (1200°C).

Chapter 3: The Effects of Impurity Content on Plastic Deformation and Microstructure Evolution in Niobium at Temperatures from 1473 to 1773 K

The following chapter is after the article titled "The effects of impurity content on plastic deformation and microstructure evolution in niobium at temperatures from 1473 to 1773 K," by Emily A. D. Brady and Eric M. Taleff that will be submitted for review to Metallurgical and Materials Transactions A in 2021 [54].

BACKGROUND

With a melting temperature of T_m = 2741 K (2468 °C) [1], niobium and its alloys are important to high temperature applications such as rocket nozzles and flame holders for jet engines [2]. These technical applications require high strength at elevated temperature and often a good resistance to creep deformation. Such practical applications motivate improving our fundamental understanding for the behaviors of unalloyed niobium at elevated temperatures. Standard grades of unalloyed niobium are classified by their impurity contents, such as the low-impurity reactor grade Type 1 and commercial grade Type 2 materials defined in ASTM B393-18 [19]. Increases in impurity content generally increase the strength of refractory metals at elevated temperatures [3]. But for this effect there is no clear mechanistic explanation available that is directly supported by microstructural data. The relationships between impurity content and strength in refractory metals described in the literature are generally empirical [3,55,56]. The only theories put forth for how impurities provide strengthening at elevated temperature are based on solid solution strengthening and/or dispersion strengthening [3]. Additions of W and Mo are thought to produce substitutional solid solution strengthening in niobium and increase the

recrystallization temperature [4]. An increase in the recrystallization temperature is expected to increase the retention of work hardening to higher temperatures. Carbides and oxides are suggested as sources of dispersion strengthening in refractory metals [3]. Microstructural data from Chang [3] show the presence of carbides in alloyed niobium, and a theoretical relationship between dispersoids and the creep rate is suggested by Weertman [5], where creep rate, $\dot{\varepsilon}$, is proportional to the square of interparticle spacing and inversely proportional to dislocation climb distance. But no microstructural data are available to directly support this theory. The present investigation provides new data intended to improve the mechanistic understanding for how impurity content affects the strength of unalloyed niobium at elevated temperatures.

The present authors recently reviewed all available data for the elastic modulus and plastic flow behaviors of low-impurity niobium at elevated temperatures and presented new data for the elevated-temperature deformation of a modern Type 1 niobium material [21]. These Type 1 niobium mechanical test data are in good agreement with the low-impurity niobium data from the literature, and all exhibit deformation controlled by the five-power creep mechanism, also known as dislocation-climb-controlled creep [21]. From the available literature data, only a few references provide any microstructural data for unalloyed niobium after deformation above $0.5T_m$. Behera et al. [6] report microstructural data for grain size, grain shape, and some flow localization in niobium after deformation. Brinson and Argent [7] report microstructural data that demonstrate a few slip lines in niobium after deformation. They also report data from niobium tested slightly below $0.5T_m$ for grain size and demonstrate the presence of dislocation substructure after

deformation. Klein and Gulden [9] also present microstructural data that demonstrate the presence of substructure in niobium after deformation. Rawson and Argent [8] present microstructural data that showcase dislocation networks in pure niobium after deformation. Microstructural data previously provided by the present authors for low-impurity Type 1 niobium [21] (ASTM B393-18) [19] include grain size, grain shape, and evidence for the presence of substructure after deformation. Unfortunately, the microstructural characterization techniques used for data in the literature do not distinguish grains from subgrains, which leaves the substructures produced by deformation at elevated temperatures unquantified.

The present investigation addresses the effects of impurity content in niobium by testing a Type 2 niobium sheet material, which has a higher impurity content than the previously investigated Type 1 [21] material (ASTM B393-18) [19]. Microstructural characterization after static annealing and after deformation at elevated temperatures was conducted on both the Type 1 niobium previously tested in Chapter 2 [21] and the Type 2 niobium tested for the present study. The deformation behavior of the Type 2 niobium is analyzed and compared to the deformation behavior of the Type 1 niobium and to relevant creep data from the literature. The relationships between impurity content and microstructure and between microstructure and deformation behavior in unalloyed niobium are explored. Special attention is given to the effects of impurity content on substructure and of subgrain size on deformation behavior. These effects provide a mechanistic connection between impurity content and mechanical behavior at elevated temperatures in refractory metals.

EXPERIMENTAL PROCEDURES

The material investigated is a niobium sheet material meeting the Type 2 designation of ASTM B393-18 [19] with a thickness of 1.52 ± 0.10 mm (0.060 ± 0.004 in). Its chemical composition is listed in Table 3.1, as provided by the supplier. Two test specimen types were produced, one for static annealing and another for tensile tests at elevated temperatures. Specimens for static annealing were sheared as one-inch by one-inch rectangular blanks with a small hole punched in the corner to accommodate the molybdenum wire used to hang the specimen in a vacuum furnace during testing. Specimens for tensile testing were dog-bone-shaped coupons produced by first excising rectangular blanks from the sheet using waterjet machining. Through holes were then drilled for loading pins. The reduced section of the gauge region was produced by electrical discharge machining (EDM) to avoid introducing unnecessary deformation into the material. The tensile specimens had square grip regions of 19.1 ± 0.13 mm (0.75 ± 0.005 in) on each side with a centered hole of diameter 6.4 mm (0.25 in) to accommodate loading pins. The gauge region had a length of 25.4 ± 0.03 mm (1 ± 0.001 in), a width of 6.35 ± 0.03 mm (0.25 ± 0.001 in), and a shoulder radius of 1.59 mm (0.63 in) between the gauge and grip regions. Specimens were excised with the tensile direction at either 0 or 90 degrees with respect to the rolling direction, as shown in Figure 3.1. Figure 3.1 identifies the sheet rolling direction (RD), sheet long transverse direction (LTD), tensile direction (TD), tensile long transverse direction (TLTD), and short transverse direction (STD) with respect to the sheet material and the tensile specimen orientation.

Table 3.1: Chemical compositions of the niobium materials in ppm by weight

	C	N	O	H	Zr	Ta	Fe	Si	W	Ni	Mo	Hf	Ti	Nb
Type 2	36	10	96	5	1	548	4	7	89	2	10		6	bal.
Type 1	9	60	73	3	5	300	5	10	33	<5	<10	10	<5	bal.

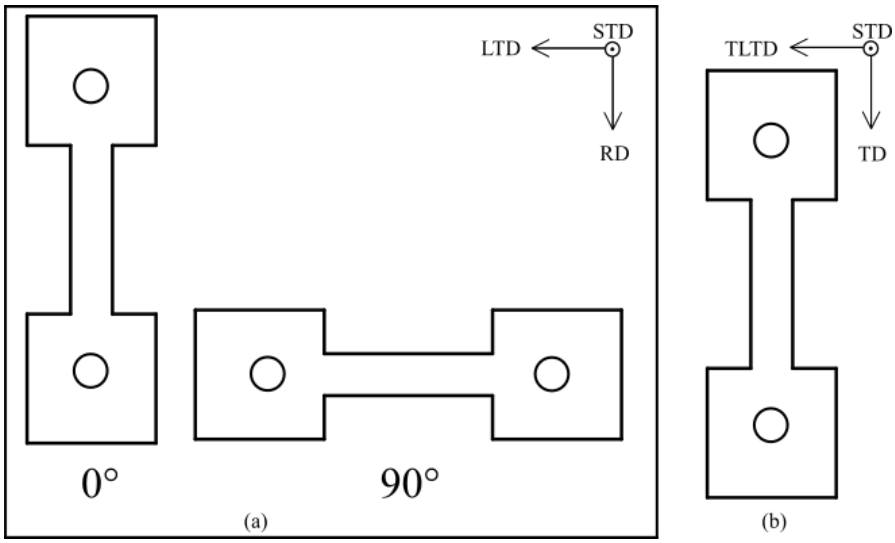

Figure 3.1: (a) The rolling direction (RD), long-transverse direction (LTD), and short-transverse direction (STD) are defined for the sheet material relative to the two orientations of tensile coupons. (b) The directions defined with reference to the tensile coupon include the tensile direction (TD) and the tensile long-transverse direction (TLTD).

Uniaxial tensile tests were conducted at temperatures from 1473 to 1773 K (1200 to 1500°C) in increments of 50 K at constant true-strain rates of 10^{-3} and 10^{-4} s^{-1}. Specimens were tested using an electro-mechanical, ball-screw-driven universal test machine attached to a vacuum furnace heated by tungsten heating elements. Computer control applied either a controlled load or a constant true-strain rate to a tensile specimen, which was held in tungsten pull rods by SiC pins. Specimen elongation was measured from crosshead

displacement. Assuming no flow localization and constant volume in the specimen gauge region, a computer algorithm calculated and applied a constant true-strain rate during tensile elongation. To calculate the initial gauge length at temperature, a linear thermal expansion coefficient of $\alpha = 7.1 \times 10^{-6}\ K^{-1}$ [30] was used to account for thermal expansion while heating to temperature. Metal bellows sealed the top and bottom of the furnace, with pull rods going through the center of each. Load was measured from a load cell outside the furnace. The forces from bellows extension and air pressure on the bellows were measured and used to correct all load cell readings. Before testing, the temperature profile within the region of the furnace that contains the test specimen was measured with a thermocouple independent of the furnace control thermocouple. These measurements were used to determine the control settings required to achieve desired specimen temperatures and estimate temperature variations along the specimen gauge region, approximately ± 10 K for the temperatures investigated.

For testing at elevated temperatures, the furnace was evacuated after inserting a test specimen. Only after purging with argon three times and reaching a vacuum of approximately 10^{-6} torr was power applied to heat the furnace. A small load of approximately 22 N, an engineering stress of 2.3 MPa, was applied to each tensile specimen during heating to accommodate thermal expansion in the load train and avoid buckling the specimen. The time to reach each test temperature was approximately 15 minutes. Once at temperature, the furnace was held at temperature for one hour to allow for complete thermal expansion of the pull rods before tensile testing. This hold time was also intended to ensure recrystallization of the niobium material. The recrystallization

temperature of niobium is documented to be between 1123 and 1573 K (850 and 1300°C) [30]. After holding at temperature, a constant true-strain rate of 10^{-3} or 10^{-4} s^{-1} was applied to the specimen until either a true strain of approximately 0.3 or rupture was achieved. For specimens that did not rupture, the final load on the specimen was then held constant using computerized load control. This final load was held until the furnace cooled to 1173 K (900°C) or lower; this step was intended to preserve the deformed microstructure developed in the specimen during testing. After reaching 1173 K (900°C) or lower, the applied load was reduced to approximately 22 N until cooling was complete. Because specimens were tested in vacuum, quenching to better preserve the microstructures developed at elevated temperatures was not possible. Once the furnace reached 303 K (30°C), the furnace was opened, the small load was removed from the specimen, and the specimen was removed from the furnace.

The load-elongation data obtained from the tensile tests were corrected to account for known experimental effects. Load data were corrected for the force from the bellows under vacuum, which was measured as a function of bellows extension through an independent experiment. Elongation data were corrected for the flexibility of the load train by calculating specimen stiffness using the known temperature-dependent, unrelaxed, dynamic elastic modulus for niobium [21]. In tensile tests at 1723 and 1773 K (1450 and 1500°C), plastic deformation produced some elongation of the loading-pin holes. To remove this effect from the specimen elongation measurements, the gauge length of each specimen was measured after testing. These measurements were used to correct the final specimen strain calculated from crosshead displacement. Little to no plastic deformation

or elongation was observed at loading-pin holes in specimens tested at 1673 K (1400°C) and lower temperatures. The maximum error in calculated specimen elongation was approximately 5% or less for these specimens, and no correction was applied. True stress and true strain were calculated from the corrected data. The absolute uncertainty in true stress was estimated to be a maximum of 1 MPa.

Static annealing tests were conducted at 1573 and 1773 K (1300 and 1500°C) in the same vacuum furnace used for tensile tests. After stabilizing at temperature for 1 hour, the specimens were held at temperature for an additional 5 minutes, the same time at temperature as the tensile specimens tested at a constant true-strain rate of 10^{-3} s^{-1} to a total true strain of 0.3. The 1573 K (1300°C) annealed specimen came from the undeformed grip region of the tensile specimen tested at a constant true-strain rate of 10^{-3} s^{-1}. The static annealing test at 1773 K (1500°C) used a rectangular specimen.

After testing, specimens were ground with silicon carbide papers of decreasing coarseness to 1200 grit, polished with diamond suspensions down to 1 μm, and then final polished with a solution of colloidal silica and hydrogen peroxide (5:1 ratio by volume). Electron backscatter diffraction (EBSD) data were collected using two conditions: 1. a working distance of approximately 10 mm at 20 kV with 2 x 2 binning on a Thermo Fisher Scientific CMOS EBSD system in a Scios 2HiVac Dual beam Scanning Electron Microscope (SEM) or 2. a working distance of 22.2 mm at 30 kV with 4 x 4 binning on a EDAX CMOS EBSD system in an In-Situ Ion Irradiation SEM. A majority of the EBSD scans used a step size of 2 μm or less. Early in the EBSD data collection, smaller grains were noted near machined surfaces. Because these grains were much smaller than the

grains away from the machined surface, these smaller grains are likely a result of the machining process and not representative of the general microstructure. The regions with smaller grains near machined surfaces extend approximately 500 μm into the material from the machined surface and are approximately 16% of the total area in the gauge region. To calculate grain sizes representative of the material, these machined surfaces were generally avoided in EBSD data collection. EBSD was also performed on a Type 1 niobium (ASTM B393-18) [19] material that was previously subjected to similar thermo-mechanical testing, the experimental details for which are provided in Chapter 2 [21]. EBSD data were processed using MTEX, a Matlab^{TM} Toolbox [57]. EBSD data were corrected for specimen alignment by applying the required specimen symmetry from pole figures (PFs). Some filling was applied to isolated unindexed points, which generally comprised less than 16% of any EBSD scan. Where unindexed points clustered together, these regions were left unfilled and are presented as blacked out regions. Grain size, grain aspect ratio and other microstructural information were calculated from the corrected EBSD data. Grain boundaries were defined by a minimum misorientation angle of 5 degrees and a minimum grain area of 11.7 μm^2. Grain areas, A_i, were measured, and grain size was calculated using the lineal intercept diameter, $l_i = \sqrt{\pi A_i / 4}$, as described in ASTM E112-13[1] [31]. Most grain sizes reported were calculated using only grains completely inside a scan area. However, minimum grain sizes were calculated for specimens with grain sizes too large to

[1] To follow the published standard and be as consistent as possible with data from the literature, the equation reported in ASTM E113-13 and repeated in the text above is used. However, the authors believe that this equation from ASTM E113-13 should more correctly be written as $l_i = \sqrt{(4A_i/\pi)}$.

provide enough grains fully within the scan area to assure a reliable measurement of grain size. These measurements used grains only partially within the scan areas, as well as any grains fully within the scan area. Minimum grain size measurements are denoted with a "≥" in front of the grain size value. Backscatter electron (BSE) images were collected to supplement and compare with EBSD data. BSE images were collected with a working distance of 15 mm at 10kV in an SEM. The lineal intercept method from ASTM E112-13 [31] was used to measure subgrain size on select TD(RD)/TLTD inverse pole figure (IPF) maps. A misorientation threshold of five degrees was used to segment grains in these IPF maps. There are three different ways to plot IPF maps, with respect to the TD, STD, or TLTD. The map with the best contrast was selected for subgrain boundary measurements. For this study, the STD referenced IPF maps had the best contrast among the three possible IPF maps. A grid was overlaid on the chosen IPF maps, and subgrain boundary intercepts were measured along the horizontal and vertical grid lines. Subgrain boundaries were determined by visual inspection of the chosen IPF maps. Standard deviation, *s*, for the subgrain size measurement was calculated using $s = \sqrt{\sum_{i=1}^{N} |x_i - \mu| / N}$ where x_i is the length of a subgrain along an intercept line, μ is the mean of x_i, and N is the number of subgrain lengths measured.

RESULTS

Tensile Tests

Figure 3.2 shows engineering and true stress-strain curves for tensile tests conducted at a constant true-strain rate of 10^{-3} s^{-1} and temperatures from 1473 to 1773 K (1200 to 1500°C). A filled circle at the end of a curve indicates rupture. A double vertical line at the end of a curve indicates where flow stress, measured as a true stress, dropped below 99% of the maximum flow stress. At this point necking was considered sufficiently severe to prevent accurate calculations of true stress and strain. The engineering stress-strain curves demonstrate that stress decreases as temperature increases. Early necking and rupture occur at temperatures below 1573 K (1300°C). Continuous hardening occurs for tests at all temperatures, as is evident from Figure 3.2 (b). Steady state deformation, which would be indicated by a nearly constant true stress, is not achieved for any of the test conditions presented in Figure 3.2. The stress drop as temperature increases from 1673 to 1723 K (1400 to 1450°C) is greater than for similar temperature changes above 1523 K (1250°C). This might indicate a change in deformation behavior between 1673 and 1723 K (1400 and 1450°C) at 10^{-3} s^{-1}.

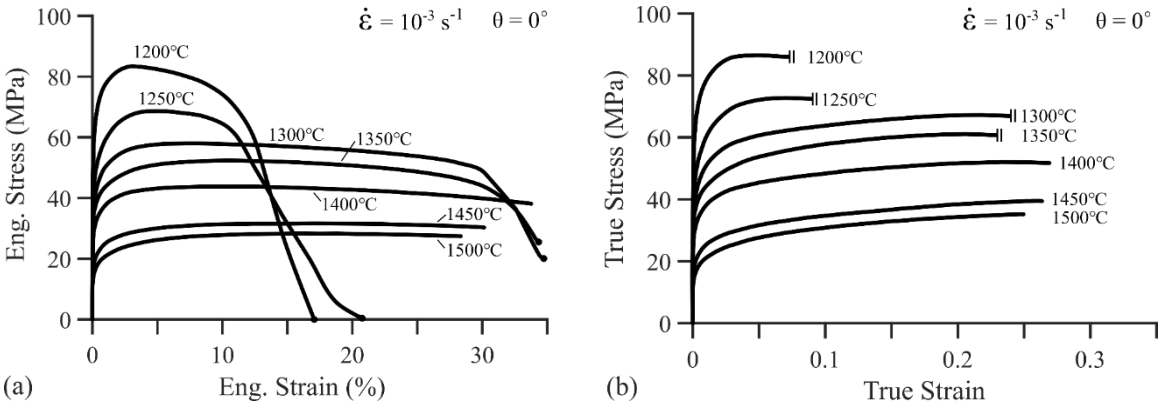

Figure 3.2: Tensile data are shown for Type 2 Nb tested at a constant true-strain rate of 10^{-3} s^{-1} and temperatures from 1473 to 1773 K (1200 to 1500°C). Data are shown as (a) engineering stress versus engineering strain and (b) true stress versus true strain. A filled circle at the end of a curve indicates specimen rupture. Double vertical lines indicate that data are truncated because of significant necking. No symbol at the end of a curve indicates that the test ended without rupture.

Figure 3.3 shows engineering and true stress-strain curves for tensile tests conducted at a constant true-strain rate of 10^{-4} s^{-1} across all temperatures. Consistent with observations at 10^{-3} s^{-1}, stress decreases as temperature increases. Likewise, early necking and rupture occur at temperatures below 1573 K (1300°C). At 1473 and 1523 K (1200 and 1250°C), the shapes observed in the necked regions for specimens tested at 10^{-4} s^{-1} are similar to those at 10^{-3} s^{-1}. As with tests at 10^{-3} s^{-1}, continuous hardening occurs for tests at 10^{-4} s^{-1} and all test temperatures. None of the tensile tests in this investigation achieved steady-state deformation. As temperature increases from 1623 to 1673 K (1350 to 1400°C) the stress drop is greater than for other similar temperature changes. This effect occurs at a temperature approximately 50 K lower than observed in the data at 10^{-3} s^{-1}. Table 3.2 presents a synopsis of the mechanical test data. The specimen orientation, test temperature and the applied true-strain rate are reported for each test. Flow stresses at true strains of 0.05, 0.1, 0.15, and 0.2 are provided for comparison. Specimens that necked during testing

are marked with a "Y" in the last column. For specimens that ruptured during testing, elongation to failure, e_f, is given as engineering strain in percent.

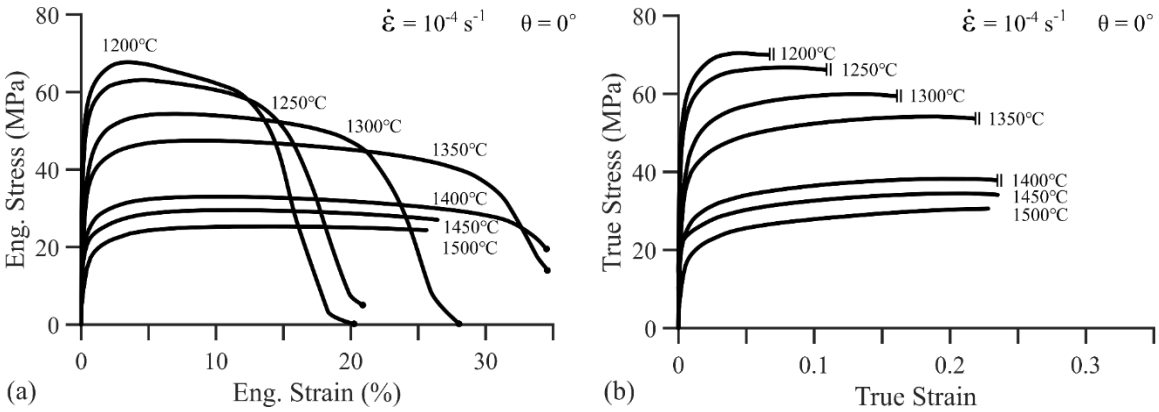

Figure 3.3: Tensile data are shown for Type 2 Nb tested at a constant true-strain rate of 10^{-4} s^{-1} and temperatures from 1473 to 1773 K (1200 to 1500°C). Data are shown as (a) engineering stress versus engineering strain and (b) true stress versus true strain. The symbols used at the end of data curves have the same meaning as described for Figure 3.2.

Table 3.2: Specimen orientation, test temperature, applied true-strain rate, average flow stresses (at true strains of 0.05, 0.1, 0.15, and 0.2), elongation to failure, and evidence of necking

θ (deg)	T (K) / T (°C)	$\dot{\varepsilon}$ (s^{-1})	$\sigma_{0.05}$ (MPa)	$\sigma_{0.1}$ (MPa)	$\sigma_{0.15}$ (MPa)	$\sigma_{0.2}$ (MPa)	e_f (%)	Necked
0	1773 / 1500	1×10^{-4}	26	28	29	30	—	
0	1765 / 1492	1×10^{-4}	23	25	26	27	—	
0	1723 / 1450	1×10^{-4}	30	33	34	34	—	
0	1673 / 1400	1×10^{-4}	34	36	38	38	—	
0	1623 / 1350	1×10^{-4}	49	52	54	54	29.3	Y
0	1573 / 1300	1×10^{-4}	57	59	60	—	21.5	Y
0	1523 / 1250	1×10^{-4}	66	66	—	—	13.2	Y
0	1473 / 1200	1×10^{-4}	70	—	—	—	11.8	Y
0	1773 / 1500	1×10^{-3}	28	31	33	34	—	Y
0	1723 / 1450	1×10^{-3}	32	35	37	38	—	
0	1673 / 1400	1×10^{-3}	45	48	50	52	—	
0	1623 / 1350	1×10^{-3}	54	58	60	61	—	Y
0	1573 / 1300	1×10^{-3}	61	64	66	67	—	Y
0	1523 / 1250	1×10^{-3}	72	—	—	—	10.5	Y
0	1473 / 1200	1×10^{-3}	87	—	—	—	8.7	Y
90	1773 / 1500	1×10^{-3}	29	33	35	37	28.3	Y

Figure 3.4 presents true stress plotted against true strain at 1473 and 1773 K (1200 and 1500°C) to demonstrate the effects of temperature and strain rate on flow stress. As expected, flow stress decreases with decreasing strain rate. Consistent with Figures 3.2 and 3.3, flow stress decreases as temperature increases at both 10^{-3} and 10^{-4} s^{-1}. Figure 3.5 presents true stress plotted against true strain at 1773 K (1500°C) and 10^{-3} s^{-1} for two specimen orientations, 0 and 90 degrees. The flow stress for the 90 degree orientation is slightly higher than for the 0 degree orientation. The maximum flow stress difference between the 0 and 90 degree orientations is 2.6 MPa, which is less than three times the absolute uncertainty in stress measurement of 1 MPa. Because this difference is small, there is little difference expected between the flow behavior from the 0 and 90 degree orientations under other test conditions. This is consistent with previous results from the Type 1 Nb material [21]. Neither specimen necked, which suggests that orientation does

not affect necking behavior under these conditions. These results led to a decision to focus experiments on the 0 degree orientation.

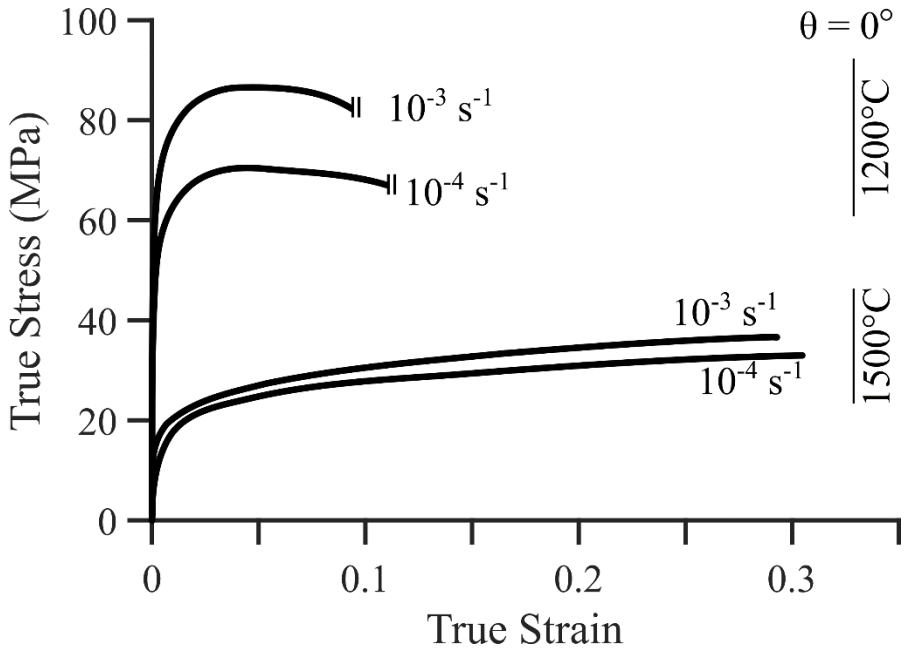

Figure 3.4: True stress is plotted against true strain for Type 2 Nb tested in the 0 degree orientation at two temperatures, 1473 and 1773 K (1200 and 1500°C), and two strain rates, 10^{-3} and 10^{-4} s^{-1}. The symbols used at the end of data curves have the same meaning as described for Figure 3.2.

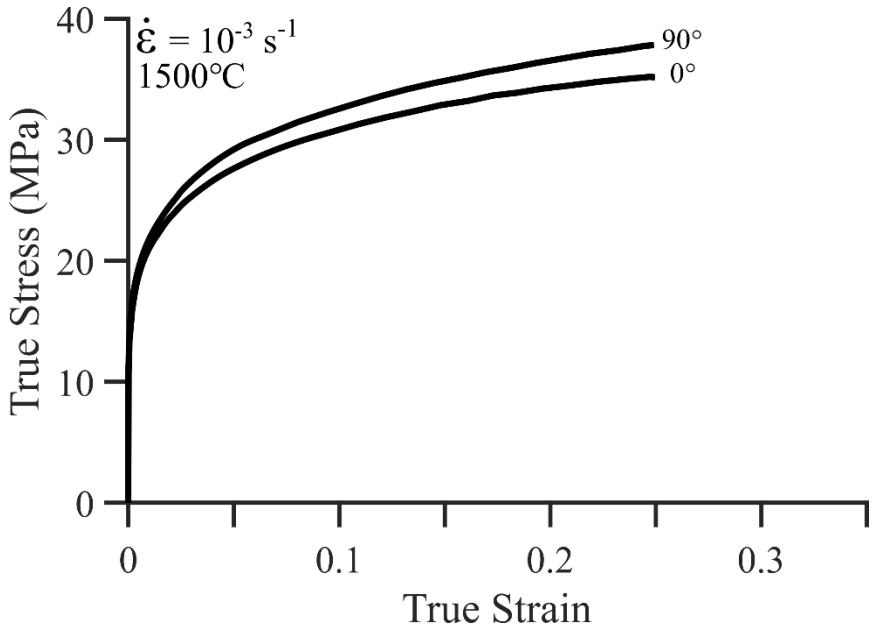

Figure 3.5: True stress is plotted against true strain for Type 2 Nb tested at 1773 K (1500 °C) and 10^{-3} s^{-1} in two different orientations.

Microstructures

Figure 3.6 presents EBSD data from Type 1 Nb statically annealed at (top) 1573 K (1300°C) and (bottom) 1773 K (1500°C). Specimens were annealed for 67 minutes, the same time at temperature as tensile tests conducted at 10^{-3} s^{-1} to a true strain of 0.4. The data are presented as (a) inverse pole figures (IPFs) showing microtexture from (b) IPF maps of the RD-LTD sheet plane and (c) IPF maps of the RD-STD sheet plane. All IPF maps for this study are presented with respect to the STD. The IPF maps shown in (c) for the RD-STD sheet plane span the entire sheet thickness, with sheet surfaces located where labeled in the figure. Grain size, *d*, and grain aspect ratio, *a.r.*, are presented as *d/a.r.* above or below the corresponding IPF map. Minimum grain sizes are reported for the RD-STD IPF maps because these did not present enough complete grains to calculate grain size. Both annealing temperatures produced full recrystallization of the Type 1 niobium. Static annealing produced the different recrystallization textures shown in (a). Because the two

specimens were extracted from different locations in the sheet material, the different textures shown in (a) might have been affected by inhomogeneity in the sheet material. Static grain growth is evident from the data at 1573 and 1773 K (1300 and 1500°C). The grain size after annealing at 1773 K (1500°C) is almost triple the grain size for 1573 K (1300°C). In the RD-STD plane, there are approximately 1 to 3 grains spanning the entire thickness of the sheet material at both temperatures. Because of these coarse grain sizes, BSE data were collected for additional grain observations. These data from large areas of the RD-STD plane (a minimum of 12 images from different areas for each temperature with a minimum area of 0.1 mm^2 per image) showed only 1 to 4 grains spanning the entire sheet thickness at both temperatures. Because it is not possible to distinguish between low- and high-angle boundaries in BSE images, the grain sizes measured using this technique are typically smaller than those measured from EBSD data [58]. Given this, the number of grains observed to span the sheet thickness is consistent between the BSE and EBSD measurements.

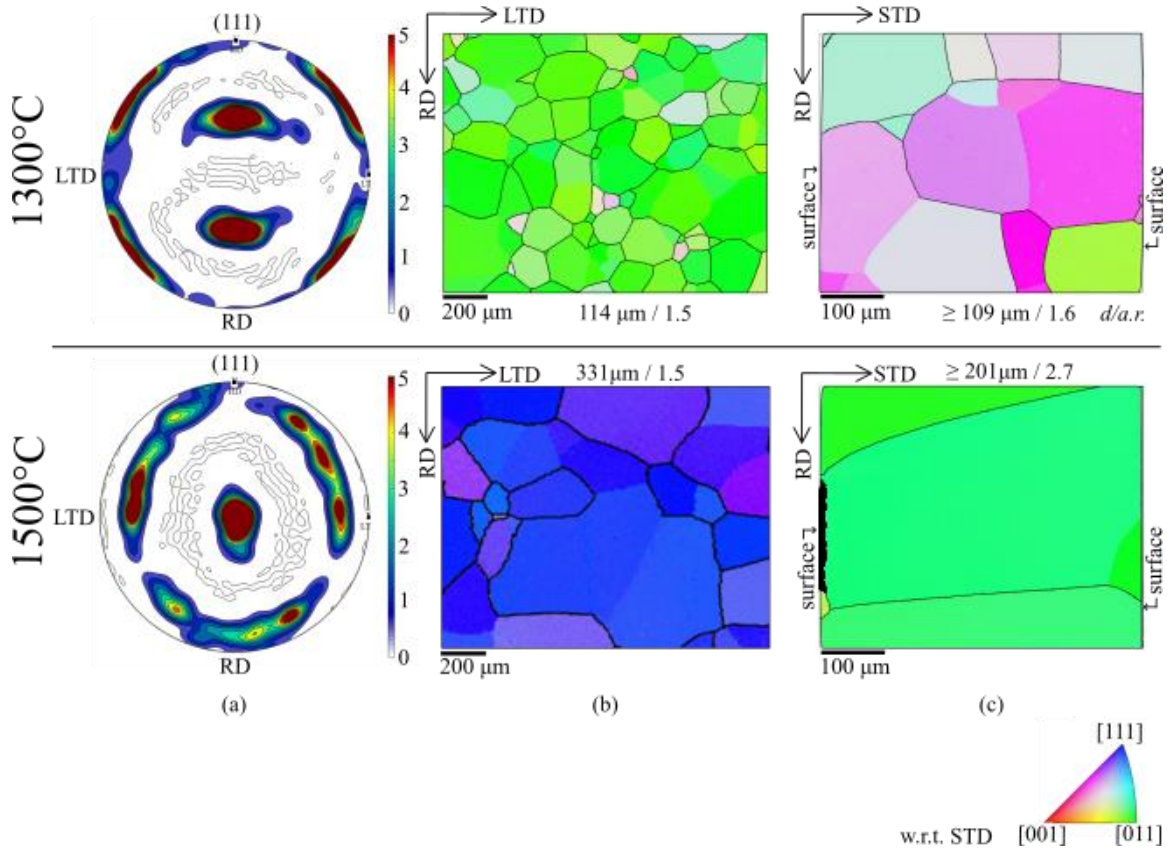

Figure 3.6: Microstructure data are shown from Type 1 Nb statically annealed for 67 minutes at (top) 1573 K (1300°C) and (bottom) 1773 K (1500 °C). Measurements for grain size (*d*) or minimum grain size (≥*d*) and the grain aspect ratio (*a.r.*) are provided as *d/a.r.*. EBSD data are shown as (a) inverse pole figures (IPFs) for the RD-LTD view, (b) IPF maps of the RD-LTD view, and (c) IPF maps of the RD-STD view. The RD-STD IPF maps encompass the entire thickness of the specimen. All IPF maps are plotted with respect to the STD.

Figure 3.7 presents EBSD data from Type 2 niobium statically annealed at (top) 1573 K (1300°C) and (bottom) 1773 K (1500°C). Specimens were annealed for 65 minutes, the same time at temperature as tensile tests conducted at 10^{-3} s^{-1} to a true strain of approximately 0.3. These data are presented in the same format as Figure 3.6. IPF maps shown in (c) for the RD-STD sheet plane span the entire sheet thickness, with sheet surfaces located where labeled in the figure. Grain size, *d*, and grain aspect ratio, *a.r.*, are reported

as *d/a.r.* above or below the corresponding IPF map. The textures shown in (a) are similar to the Type 1 niobium recrystallization texture at 1773 K (1500°C). These demonstrate a <111>|| STD fiber component within the recrystallization texture. Because the recrystallization textures are similar for both Type 2 niobium specimens, we suspect that the starting material for the Type 2 niobium is more homogeneous than the Type 1 niobium. Compared to the Type 1 niobium, grain growth increased less rapidly between 1573 and 1773 K (1300 and 1500°C) in the Type 2 niobium. The Type 2 niobium grain size in the RD-LTD sheet plane for the 1773 K (1500°C) specimen is a little over 1.5 times the grain size of the 1573 K (1300°C) specimen. For both annealing temperatures the Type 2 niobium grain size is smaller than the Type 1 niobium grain size. The Type 1 niobium grain size is five times that of the Type 2 niobium after annealing at 1573 K (1300°C) and nine times that of the Type 2 niobium after annealing at 1773 K (1500°C). The higher impurity content of the Type 2 niobium likely produced more boundary pinning and slower grain boundary migration, which slows grain growth, compared to the Type 1 niobium. The RD-STD sections shown in (c) demonstrate bimodal microstructures, with fine grains near the sheet surfaces and coarse grains near the sheet centerline. Grains are generally elongated along the RD. Grains along the centerline are significantly coarser after annealing at the higher temperature. Relative to the sheet thickness shown in (c), the material sections shown in (b) are near the sheet surface where grain size is smaller.

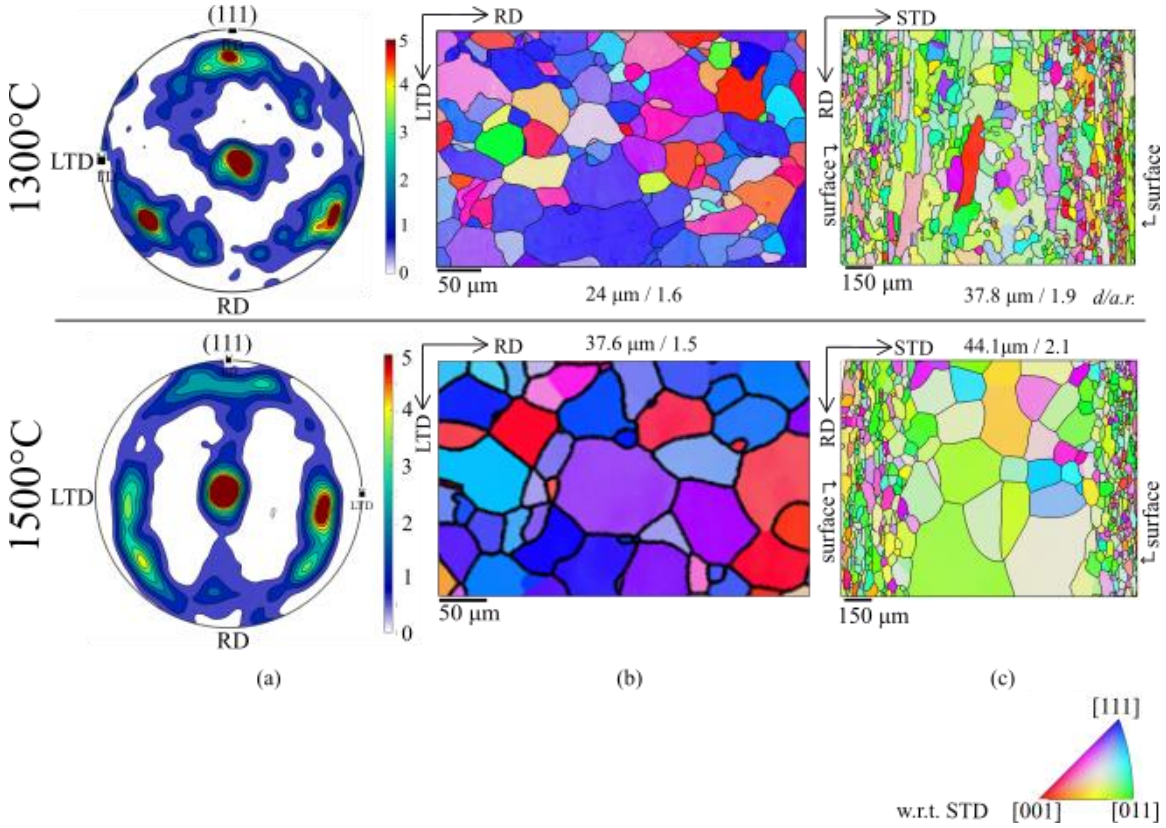

Figure 3.7: Microstructure data are shown from Type 2 Nb statically annealed for 65 minutes at (top) 1573 K (1300°C) and (bottom) 1773 K (1500 °C). Measurements for grain size (*d*) and the grain aspect ratio (*a.r.*) are provided as *d/a.r.*. EBSD data are shown as (a) IPFs for the RD-LTD view, (b) IPF maps of the RD-LTD view, and (c) IPF maps of the RD-STD view. The RD-STD IPF maps encompass the entire thickness of the specimen. All IPF maps are plotted with respect to STD.

Figure 3.8 presents EBSD data from Type 1 niobium in the 0 degree orientation deformed at 10^{-3} s^{-1} to a true strain of approximately 0.4 at (top) 1573 K (1300°C) and (bottom) 1773 K (1500°C). These data are presented in a format similar to Figure 3.6. IPF maps shown in (c) for the TD(RD)-STD specimen plane span the entire sheet thickness, with sheet surfaces located as labeled in the figure. The dark regions in the corners of images in (c) are artifacts from conductive paint obscuring underlying material. Minimum grain size, *d*, and grain aspect ratio, *a.r.*, are reported as *d/a.r.* above or below the

corresponding IPF map. The different temperatures produced similar textures, shown in (a). These textures contain the <111>|| STD fiber component of the texture from the Type 1 niobium annealed at 1773 K (1500°C). The grains shown in (b) are elongated along the TD(RD) in specimens tested at both temperatures. Significantly more grain growth occurred during the test at the higher temperature. Although only minimum grain sizes could be measured from Figure 3.8, the grain sizes after mechanical testing are apparently smaller than after static annealing at the same temperature and time. A clear difference in the microstructures after mechanical testing, compared to static annealing alone, is the presence of a distinct substructure containing subgrains. The presence of subgrains confirms the five-power creep mechanism previously identified as controlling deformation in the Type 1 niobium material [21]. Please see Chapter 2 [21] for additional details on the mechanical behavior of Type 1 niobium.

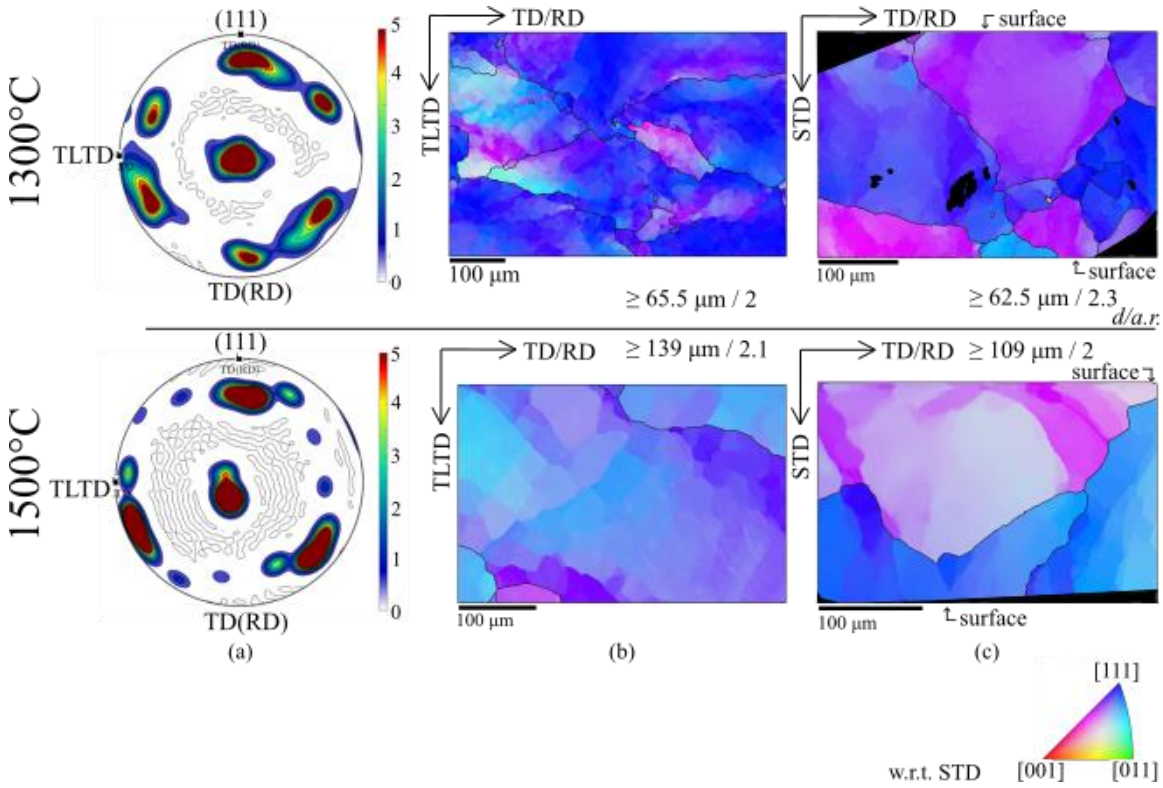

Figure 3.8: Microstructure data are shown from Type 1 Nb tested in the 0 degree orientation at a constant true strain rate of 10^{-3} s^{-1} to a total strain of approximately 0.4 at (top) 1573 K (1300°C) and (bottom) 1773 K (1500 °C). Measurements for grain size (*d*) or minimum grain size (≥*d*) and the grain aspect ratio (*a.r.*) are provided as *d/a.r.*. EBSD data are shown as (a) IPFs for the TD-TLTD view, (b) IPF maps of the TD-TLTD view, and (c) IPF maps of the TD-STD view. The TD-STD IPF maps encompass the entire thickness of the specimen. All IPF maps are plotted with respect to the STD.

Figure 3.9 presents EBSD data from Type 2 niobium in the 0 degree orientation deformed at 10^{-3} s^{-1} to a true strain of approximately 0.3 at (top) 1573 K (1300°C) and (bottom) 1773 K (1500°C). These data are presented in a format similar to Figure 3.6. The IPF map shown in (c) at 1573 K (1300°C) spans the entire thickness of the specimen, with sheet surfaces located where labeled in the figure. Grain size, *d*, and grain aspect ratio, *a.r.*, are reported as *d/a.r.* above or below the corresponding IPF map. Grain size was not

measured for the observation plane shown in (c) from the specimen tested at 1773 K (1500°C) because of a coarse grain size limiting the number of grains observed. The textures shown in (a) are different between the specimens tested at 1573 and 1773 K (1300 and 1500°C). The texture of the specimen tested at 1573 K (1300°C) retains the <111>|| STD fiber component previously observed in other specimens. The texture of the specimen tested at 1773 K (1500°C) is more complex. The microstructure of the specimen tested at 1573 K (1300°C) presents characteristics of incomplete recrystallization. These are most evident in (b). From (c) it is apparent that the specimen section shown in (b) is from near the sheet surface. The coarse grains near the center of (c) suggest more complete recrystallization at the sheet center than near the surface, leading to a bimodal microstructure in the specimen tested at 1573 K (1300°C). This is similar to the bimodal microstructure observed after static annealing, shown in Figure 3.7. The grain size is largest in the specimen tested at the highest temperature, as shown in (b). The grain sizes in both deformed specimens are approximately three times greater than those in the specimens statically annealed at the same temperature. This is opposite the trend observed for the Type 1 niobium, where plastic deformation suppressed grain growth. Substructures with easily identifiable subgrains are present at both temperatures, but the subgrain boundaries are less distinct than those in the Type 1 niobium. The microstructure of the specimen tested at 1773 K (1500°C) is complex. It demonstrates grains elongated along the TD(RD) in (b) and regions of very coarse grains in (c). To better understand this complex microstructure, additional BSE data were collected.

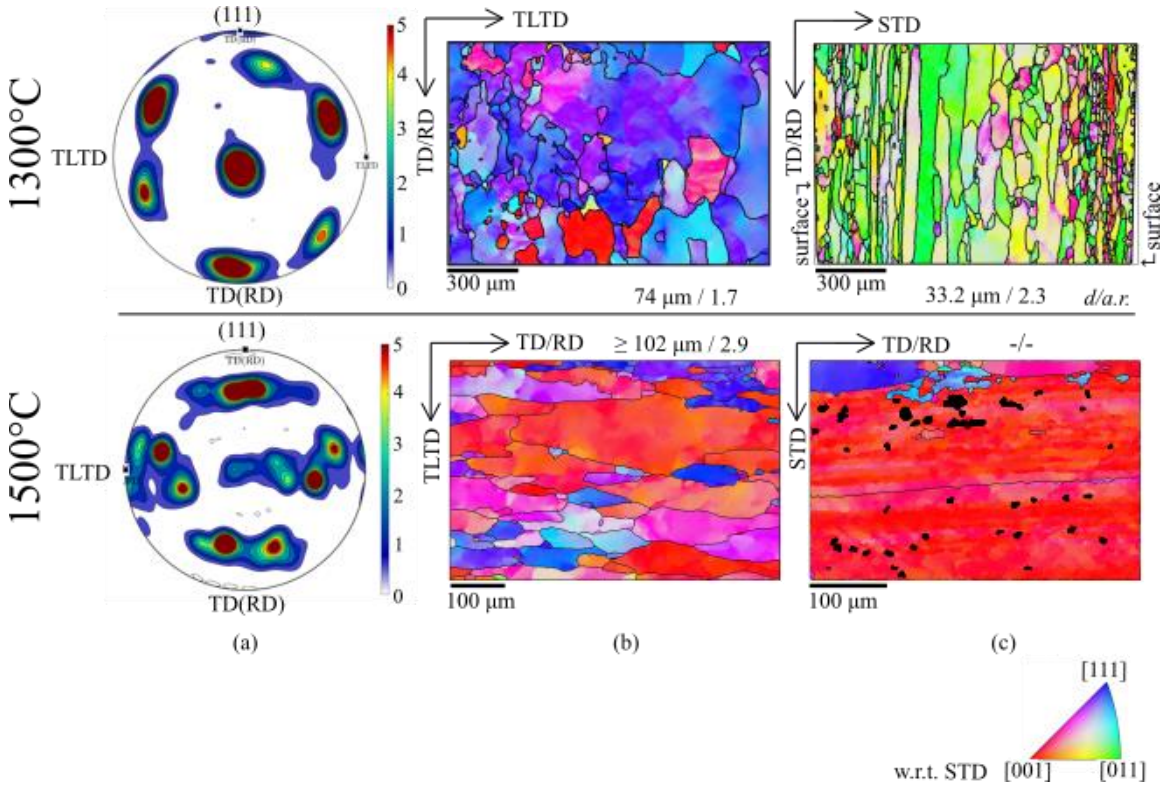

Figure 3.9: Microstructure data are shown from Type 2 Nb tested in the 0 degree orientation at a constant true strain rate of 10^{-3} s^{-1} to a total strain of approximately 0.3 at (top) 1573 K (1300°C) and (bottom) 1773 K (1500 °C). Measurements for grain size (*d*) or minimum grain size (≥*d*) and the grain aspect ratio (*a.r.*) are provided as *d/a.r.*. EBSD data are shown as (a) IPFs for the TD-TLTD view, (b) IPF maps of the TD-TLTD view, and (c) IPF maps of the TD-STD view. The TD-STD IPF map for the 1573 K (1300 °C) test encompasses the entire thickness of the specimen. All IPF maps are plotted with respect to the STD.

Figure 3.10 shows an example of the BSE data collected from the TD(RD)-STD specimen plane (Figure 3.9 (c)) for the Type 2 niobium in the 0 degree orientation deformed at 10^{-3} s^{-1} and 1773 K (1500°C). This BSE image spans nearly the entire sheet thickness, with the sheet surfaces located where labeled in the figure. The TD(RD)-STD specimen plane shows a banded microstructure. Because it is not possible to distinguish between low- (subgrain) and high-angle (grain) boundaries in BSE images, Figure 3.10 can be better

interpreted using guidance from the EBSD data in Figure 3.9. This guidance suggests that Figure 3.10 shows many subgrains with a wide distribution in sizes. An important observation is the inhomogeneity of this microstructure produced by alternating bands of coarse and fine structures.

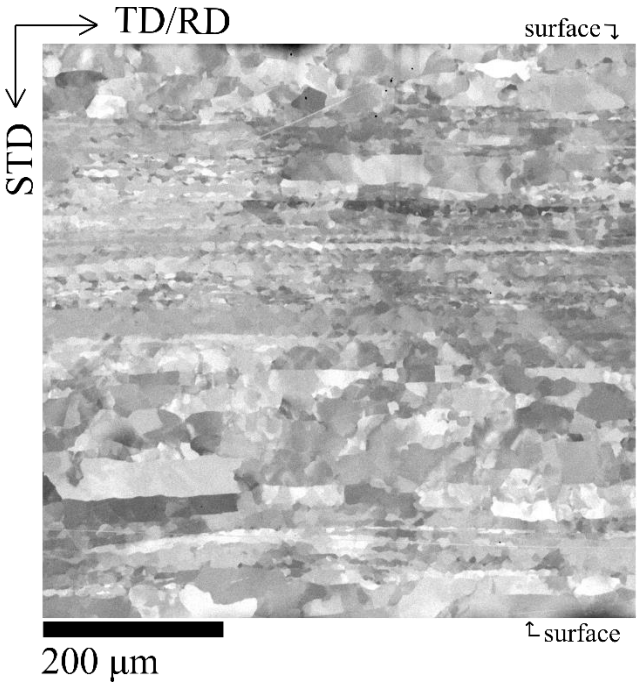

Figure 3.10: A BSE image of Type 2 niobium tested in the 0 degree orientation at a constant true-strain rate of 10^{-3} s^{-1} and 1773 K (1500°C) to a total true strain of approximately 0.3 is shown. This image encompasses nearly the entire thickness of the specimen.

Figure 3.11 presents EBSD data from Type 2 niobium deformed at 10^{-3} s^{-1} at 1773 K (1500°C) to a true strain of approximately 0.3 of a (top) 90 degree orientation and a (bottom) 0 degree orientation. These data are presented in a similar format as Figure 3.6. The IPF map shown in (c) for the 90 degree orientation spans the entire thickness of the specimen, with sheet surfaces located as labeled in the figure. These two different specimen

orientations produced similar textures, as shown in (a). Because the recrystallization texture after annealing at 1773 K (1500°C), Figure 3.7 (a) bottom, has a strong rotational symmetry about the STD, the similarity in the deformation textures shown in Figure 3.11 (a) is not unexpected. The deformation textures are sharper than the recrystallization texture. In the TD(RD)-TLTD specimen plane shown in (b), the grains from the 0 degree orientation are elongated along the TD(RD), while the grains from the 90 degree orientation are approximately equiaxed. This is why the grain aspect ratio for the 0 degree orientation is double that for the 90 degree orientation. The fine grains near the machined surface of the 90 degree specimen, labeled in (b), contrast with the coarse grains away from the machined surface. This skews the grain size measured in (b) for the 90 degree specimen toward small values, making a comparison with the grain size in the 0 degree specimen problematic. This also demonstrates that specimen machining affects microstructure to a depth of only a few hundred micrometers from the machined surface. The TD-STD specimen plane shown in (c) demonstrates a bimodal grain size for the 90 degree orientation, with smaller grains near the sheet surface and larger grains along the centerline. This is similar to the recrystallized Type 2 niobium shown in Figure 3.7 (c). This contrasts with the unusual banded microstructure shown for the 0 degree specimen in (c) and Figure 3.10.

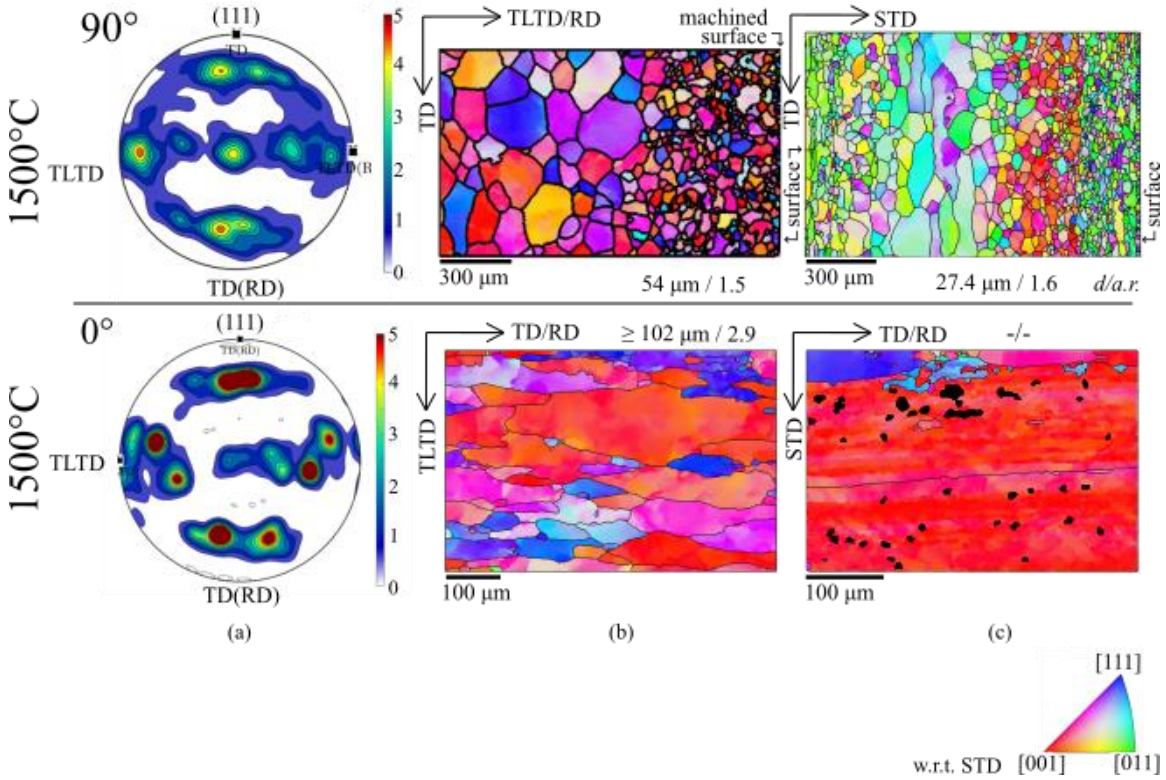

Figure 3.11: Microstructure data are shown from Type 2 Nb tested at 1773 K (1500 °C) in the (top) 90 degree and (bottom) 0 degree orientations at a constant true strain rate of 10^{-3} s^{-1} to a total strain of approximately 0.3. Measurements for grain size (*d*) or minimum grain size (≥*d*) and the grain aspect ratio (*a.r.*) are provided as *d/a.r.*. EBSD data are shown as (a) IPFs for the TD-TLTD view, (b) IPF maps of the TD-TLTD view, and (c) IPF maps of the TD-STD view. The TD-STD IPF map for the 90 degree test encompasses the entire thickness of the specimen. All IPF maps are plotted with respect to the STD.

Subgrain size was measured from IPF maps for Type 1 and Type 2 niobium materials tested in tension at 1773 K (1500°C) and 10^{-3} s^{-1}. The lineal intercept method from ASTM E112-13 [31] was used for these measurements. The tensile strains in the measured specimens were 0.4 for the Type 1 niobium, see Figure 3.8 (b), and 0.3 for the Type 2 niobium, see Figure 3.9 (b). The subgrain size in the Type 1 niobium is $\lambda = 27.3$ µm with a standard deviation of 19.3 µm. The subgrain size in the Type 2 niobium is $\lambda = 18.4$ µm with a standard deviation of 14.8 µm.

DISCUSSION

A primary motivation for the present study was to determine how the impurity content differences between the Type 1 and Type 2 niobium materials affect the microstructures evolved during deformation and how those microstructures control deformation behaviors. The literature provides some guidance on how impurity content affects the mechanical behavior of niobium at elevated temperature. Stoop and Shahinian [22,23] observed that above $0.5T_m$ oxygen impurities strengthen niobium but nitrogen impurities have no effect on creep strength. They surmised that oxygen may react to form "complex clusters" that increase creep resistance, although the formation of oxide dispersoids seems more likely, while nitrogen does not. The review by Chang [3] on the strengthening of refractory metals notes the effectiveness of oxide and carbide dispersoids in raising the recrystallization temperature. Such dispersoids would also be expected to increase creep strength. This information suggests that the higher carbon and oxygen contents of the Type 2 niobium should produce a higher creep strength than that of the Type 1 niobium. The Type 2 niobium has four times as much carbon and only 1.3 times as much oxygen as the Type 1 niobium, as shown in Table 3.1. This suggests that carbon content is the most important impurity difference between the Type 1 and Type 2 niobium materials. The Type 2 niobium material also contains more Ta, by a factor of almost two, and more W, by a factor of almost three, than the Type 1 niobium. Because W is a weaker carbide former than either Ta or Nb [47,59], the W is most likely in solid solution. The Type 2 niobium probably contains dispersed carbides containing Ta and Nb, which are both strong carbide formers [47,59]. Although the imaging and characterization of these possible carbide dispersoids is beyond the scope of the present study, the expectation of their existence is important to interpreting the microstructures of the two niobium materials and how these microstructures influence the deformation behaviors observed.

The EBSD and BSE data from Type 1 and Type 2 niobium provide new understanding for how impurity content affects microstructure evolution. Because microstructure controls mechanical behavior, the impurity content differences between the Type 1 and Type 2 niobium may also explain the differences in mechanical behavior between these materials. Compared to the Type 1 niobium, the higher impurity content of the Type 2 niobium: 1. impedes recrystallization, 2. slows grain growth, 3. leads to inhomogeneous microstructures, and 4. slows recovery, allowing the retention of finer subgrains during deformation.

The microstructural data indicate that an increased impurity content impedes recrystallization. The Type 1 niobium exhibits full recrystallization at both 1573 and 1773 K (1300 and 1500°C) as shown in Figures 3.6 and 3.8. Incomplete recrystallization is observed in the Type 2 niobium deformed at 1573 K (1300°C) shown in Figure 3.9. This specimen was annealed for 1 hour before tensile straining to promote recrystallization before deformation. We believe this specimen was not fully recrystallized before deformation, leading to the microstructures shown in Figure 3.9. Static annealing at 1573 K (1300°C) for approximately 1 hour was fully sufficient to recrystallize the Type 1 niobium, see Figures 3.6 and 3.8, but it was not necessarily sufficient to fully recrystallize the Type 2 niobium. While static annealing for 65 minutes did produce a fully recrystallized microstructure in the Type 2 niobium, see Figure 3.7, annealing for only 60 minutes prior to tensile testing produced a partially recrystallized microstructure, see Figure 3.9. These results suggest that impurities suppress recrystallization in the Type 2 niobium.

Grain growth is faster in the Type 1 niobium compared to the Type 2 niobium. This is most likely a result of their impurity difference. Grain sizes in the Type 1 niobium are significantly larger than in the Type 2 niobium after equivalent static annealing treatments, as shown in Figures 3.6 and 3.7. The increase in the rate of static grain growth with

increasing temperature is greater for the Type 1 than the Type 2 niobium. The grain size after annealing at 1773 K (1500°C) for approximately 1 hour is triple that after 1573 K (1300°C) for the Type 1 niobium, but this difference is only 1.5 times for the Type 2 niobium. The material with a higher impurity content, the Type 2 niobium, demonstrates smaller grain sizes and slower grain growth. This effect is likely because of increased grain boundary pinning, which slows grain growth in the Type 2 niobium.

The greater impurity content of the Type 2 niobium leads to more inhomogeneous microstructures than observed in the Type 1 niobium. A banded microstructure was observed in the Type 2 niobium deformed at 1773 K (1500°C), shown in Figure 3.10. This banded microstructure suggests inhomogeneous microstructure evolution, particularly for subgrains. This inhomogeneous microstructure evolution may have also occurred at 1573 K (1300°C) and obstructed recrystallization during deformation. The inhomogeneity of the deformed microstructure suggests the possibility of an inhomogeneous distribution of impurity content in the Type 2 niobium material. However, a bimodal microstructure is evident after recrystallization, with coarse grains along the sheet center and finer grains near the sheet surfaces. This bimodal microstructure is likely a result of through-thickness inhomogeneity of the plastic deformation developed during low-temperature rolling of the sheet material prior to recrystallization, rather than an inhomogeneous distribution of impurities. No banded microstructures were observed in the Type 1 niobium.

The microstructures observed after deformation in the Type 2 niobium are generally finer than those in the Type 1 niobium. This is likely a result of an increasing resistance to recovery with increasing impurity content. This allows the retention of finer subgrains during deformation. Subgrains were observed and measured in both the Type 1 and Type 2 niobium after deformation. The subgrains observed in the Type 1 niobium had clearer and more distinct boundaries than the smaller subgrains observed in the Type 2 niobium.

This suggests that recovery is faster in the Type 1 niobium. The observation of subgrains in both materials is consistent with a significant role for the fiver-power creep mechanism in deformation [60]. The subgrain sizes measured for the Type 1 and Type 2 niobium after deformation at 1773 K (1500°C) and 10^{-3} s^{-1} are λ_1 = 27.3 μm and λ_2 = 18.4 μm. These suggest that five-power creep [60] should produce a flow stress in the Type 2 niobium that is approximately $\sigma_2/\sigma_1 \approx \lambda_1/\lambda_2 = 1.4$ times higher than the Type 1 niobium, a prediction that will be further explored. These observed differences in recovery and subgrain sizes are consistent with the higher impurity content of the Type 2 niobium relative to the Type 1 niobium.

New data are presented from mechanical tests of the Type 2 niobium. These data indicate distinct differences from the behaviors of Type 1 niobium previously reported [21]. The Type 2 niobium did not present the characteristics of steady-state deformation for the temperatures and strain rates tested in this study. Most important among the requirements for steady-state deformation are a steady-state microstructure leading to a steady-state flow stress at a constant temperature and applied true-strain rate. Figure 3.12 presents data from the Type 2 niobium as strain rate plotted against stress on dual logarithmic scales at (a) a true strain of 0.05 and (b) a true strain of 0.15. Note from Figures 3.2 and 3.3 that only data at 1573 K (1300°C) and higher temperatures are available for $\varepsilon = 0.15$. The slopes of the data in Figure 3.12 are equivalent to a stress exponent, which varies widely from 7.6 to 53. The anomalous behavior at 1673 K (1400°C) between the fast and slow strain rates, previously noted from Figures 3.2 and 3.3, is apparent in the low stress exponent measured at 1673 K (1400°C) from Figure 3.12.

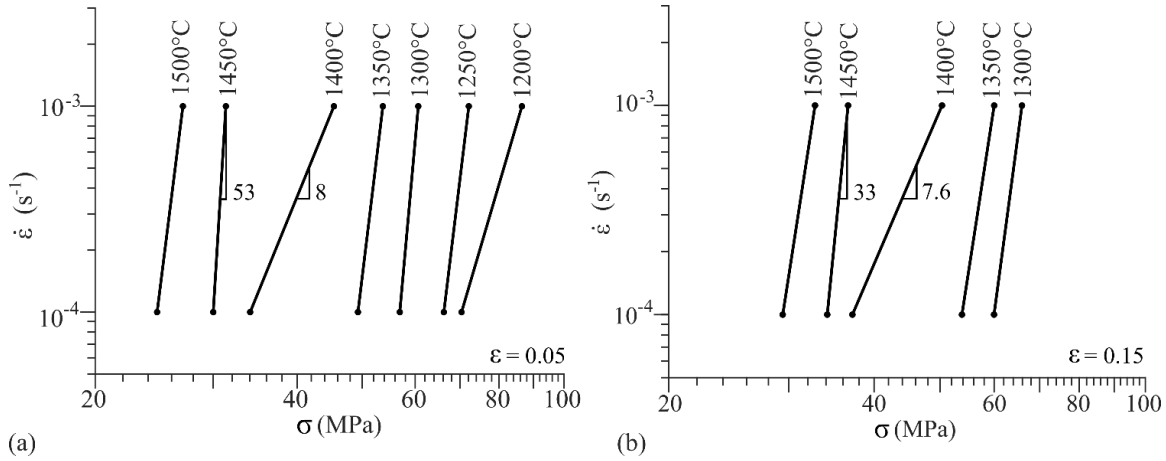

Figure 3.12: True-strain rate is plotted against true stress on dual logarithmic scales at (a) a true strain of 0.05 and (b) a true strain of 0.15 for Type 2 niobium with the 0 degree specimen orientation. The minimum and maximum stress exponents are marked next to their respective data in each plot.

To better understand the relationships between flow stress, temperature, and strain rate from the data of Figure 3.12, an empirical analysis using the Zener-Hollomon parameter is pursued. This analysis requires normalization of strain rate and flow stress at a specific strain. Strain rate is normalized using the Zener-Hollomon parameter [52]:

$$Z = \dot{\varepsilon}\ exp\left(\frac{Q_z}{RT}\right), \qquad (3.1)$$

where $\dot{\varepsilon}$ is true-strain rate, Q_z is an activation energy for plastic flow, R is the universal gas constant, and T is absolute temperature. Because the data for Type 2 niobium did not produce steady-state deformation, measuring an activation energy from those data is problematic. Attempts to do so did not produce a reasonable result. An activation energy for the steady-state deformation of Type 1 niobium was previously measured as Q_c = 454 kJ/mol [21], which is close to the activation energy of self-diffusion in niobium, 440 kJ/mol [47]. For the analysis of Type 2 niobium data, it was assumed that $Q_z = Q_c$ = 454 kJ/mol. The previous study of Type 1 niobium analyzed all the available data from the literature for the elastic modulus of polycrystalline niobium [21]. That study recommended

using a value of 104.9 GPa for the unrelaxed dynamic elastic Young's modulus from room temperature up to 1300 K (1027°C) and then the following equation for the decreasing modulus values at higher temperatures,

$$E = 104.9 - 8.3513\times10^{-9}\,(T - 1300)^{3.154}\,, \qquad (3.2)$$

where E is in GPa and T is in K.

Figure 3.13 presents the Zener-Hollomon parameter plotted against stress normalized by the temperature dependent unrelaxed dynamic elastic modulus on dual logarithmic scales for true strains of 0.05 and 0.15. Data from all the tests of the Type 2 niobium are presented. A line fit to these data demonstrates a slope of 5.8, which can be interpreted as a stress exponent. The data at a true strain of 0.15 show higher stresses than the data at a true strain of 0.05. This is consistent with the continuous hardening demonstrated in Figures 3.2 and 3.3. The data present a wide scatter about the fitted line. The scatter in data from the Type 2 niobium are much greater than previously observed for Type 1 niobium in a similar analysis [21]. This is likely a result of the highly inhomogeneous deformation microstructures developed in the Type 2 niobium leading to variations in flow stress. Figure 3.13 suggests that the seemingly anomalous temperature dependence of plastic flow near 1673 K (1400°C) noted for Figures 3.2, 3.3, and 3.12 might be interpreted as simply scatter in the test data.

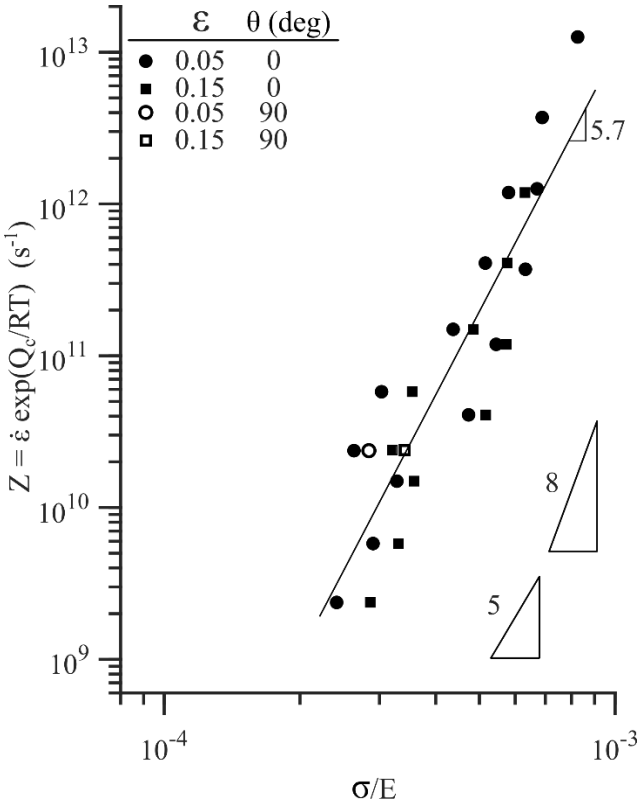

Figure 3.13: The Zener-Hollomon parameter is plotted against stress normalized by the temperature-dependent unrelaxed dynamic elastic modulus on dual logarithmic scales for all Type 2 Niobium data at true strains of 0.05 and 0.15.

Figure 3.14 presents the Zener-Hollomon parameter plotted against the stress normalized by the temperature dependent unrelaxed dynamic elastic modulus on dual logarithmic scales for both Type 1 and Type 2 niobium in the 0 degree specimen orientation. The Type 1 niobium data are taken from Chapter 2 [21] at a true strain of approximately 0.4. The Type 2 niobium data are taken at true strains of 0.15, and 0.25 for a single test at 1773 K (1500°C). The line fit to the Type 1 niobium data is the same as reported in Chapter 2 [21]. The line for the Type 2 niobium data was fit using only those data shown in Figure 3.14 but produced a slope nearly equal that of the line shown in Figure 3.13. The slopes of these data are the stress exponents for the Type 1 and Type 2 niobium.

The Type 2 niobium has a higher stress exponent than the Type 1 niobium. However, both stress exponents, 5.6 and 5.8, are near the value of 5 expected for five-power creep. Five-power creep is reported in Chapter 2 [21] as the controlling deformation mechanism for Type 1 niobium. A stress exponent close to 5 for the Type 2 niobium suggests possible deformation by five-power creep, even though steady state deformation is not reached. For all temperatures and strain rates investigated, the Type 2 niobium has higher flow stresses than the Type 1 niobium. Measuring the ratio of flow stresses between the two materials at the same temperature, strain rate, and total strain quantifies the strength difference between these materials. From Figure 3.14, σ/E is measured at 1773 K (1500°C) with a strain rate of 10^{-3} s^{-1} for both the Type 1 and Type 2 niobium, as shown by the arrows in Figure 3.14. To match the strains used for these measurements as closely as possible, the datum from Type 2 niobium was measured at a true strain of 0.25, which is the largest usable strain from the respective tensile test. At 1773 K (1500°C) and 10^{-3} s^{-1}, $(\sigma/E)_1 = 1.9\times10^{-4}$ for Type 1 niobium and $(\sigma/E)_2 = 3.4\times10^{-4}$ for Type 2 niobium. The ratio of flow stresses between Type 2 and Type 1 niobium is thus $\sigma_2/\sigma_1 = 1.8$, as noted in Figure 3.14. This is a significant difference in strengths.

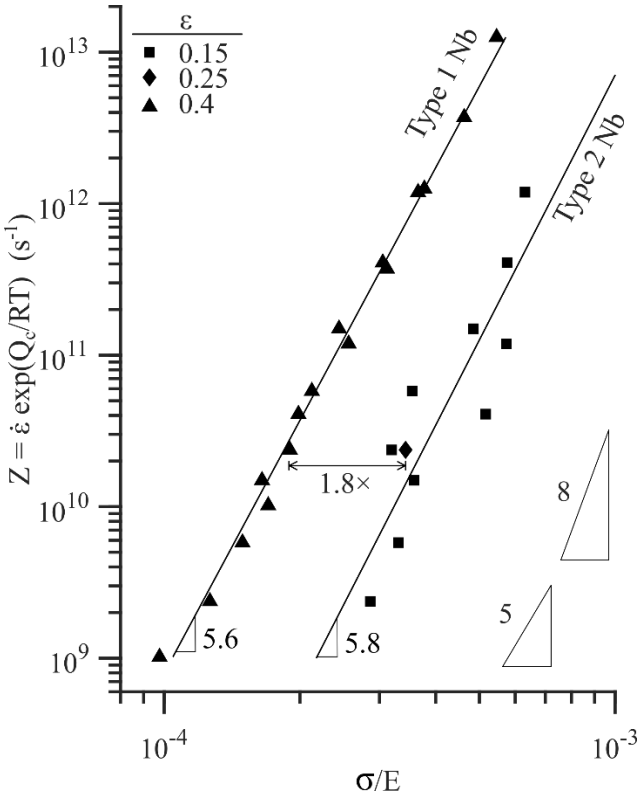

Figure 3.14: The Zener-Hollomon parameter is plotted against stress normalized by the temperature-dependent unrelaxed dynamic elastic modulus on dual logarithmic scales for both Type 1 and Type 2 niobium materials tested in the 0 degree orientation. The Type 1 niobium data are taken at 0.4 true strain. The Type 2 niobium data are taken at true strains of 0.15 and 0.25.

An explanation for this strength difference may be found in the subgrain sizes. For five-power creep, stress normalized by the temperature-dependent elastic modulus is inversely proportional to subgrain size, $\sigma/E \propto 1/\lambda$ [60]. This suggests that the ratio of stresses, σ_2/σ_1, should be approximately equal to the inverse of the ratio of the subgrain sizes, λ_1/λ_2, where λ_1 and λ_2 are the subgrain sizes developed in the Type 1 and Type 2 niobium materials at the conditions under which σ_2 and σ_1 are measured. Subgrain sizes were measured from Type 1 and Type 2 niobium deformed at 1773 K (1500°C) and 10^{-3} s^{-1}, the same conditions under which the stresses were measured, and are $\lambda_1 = 27.3$ μm and λ_2

= 18.4 μm. This produces a subgrain ratio of λ_1/λ_2 = 1.4, which is only slightly less than the stress ratio of σ_2/σ_1 = 1.8. The difference between σ_2/σ_1 and λ_1/λ_2 is likely a result of the large uncertainty in measuring subgrain sizes, as suggested by the large standard deviations for these measurements. Thus, the five-power creep mechanism offers a reasonable explanation for the higher strength of the Type 2 niobium compared to the Type 1 niobium, that of the Type 2 niobium retaining finer subgrain structure during deformation. As discussed for the microstructure data, the higher impurity content in the Type 2 niobium compared to the Type 1 niobium reduced recovery and grain/subgrain growth in the Type 2 material and led to more inhomogeneous microstructures. These results reveal the important role of impurity content on microstructure evolution and flow behaviors in niobium during deformation at elevated temperature.

Figure 3.15 presents strain rate normalized by the independently measured lattice self-diffusion coefficient [47] plotted against stress normalized by the temperature dependent unrelaxed dynamic elastic modulus [21] on dual logarithmic scales. Type 1 and Type 2 niobium are plotted as filled symbols with all the relevant data available from the literature plotted as hollow symbols. Table 3.3 provides a legend for Figure 3.15 and lists the sources of literature data. Additional details on these data and their relevance are provided in Chapter 2 [21]. The independently measured diffusivity is taken from Reference [47] as,

$$D = 8 \times 10^{-7} exp\left(\frac{-Q_1}{RT}\right) + 3.7 \times 10^{-4} exp\left(\frac{-Q_2}{RT}\right), \qquad (3.3)$$

where Q_1 is 349.6 kJ/mol, Q_2 is 438.4 kJ/mol and D is diffusivity in m^2/s. The normalization of Figure 3.15 was previously shown to bring together all the extant data for low-impurity niobium onto a single curve. This was the result expected from deformation under five-power creep and may be understood through the phenomenological equation for creep. The phenomenological equation for creep is [32,38,39],

$$\dot{\varepsilon} = A\,{}^{D}/_{b^2}\left(\frac{\sigma}{E}\right)^{n}, \qquad (3.4)$$

where b is the Burgers vector magnitude, A is a material dependent constant, and n is the stress exponent, which is approximately 5 for five-power creep. Equation 3.4 suggests using the $\dot{\varepsilon}/D$ normalization. This is quite convenient because measured values of activation energy for creep vary wildly between different studies. Low-impurity niobium data from the literature and the Type 1 niobium data fit reasonably along a single curve, suggesting that similar subgrain sizes developed in these materials under similar test conditions. The normalizations of Figure 3.15 produce a stress exponent of n = 5.1 for the Type 2 niobium, slightly lower than those produced in Figures 3.13 and 3.14. The higher strength of the Type 2 niobium compared to the low-impurity niobium materials arises because of its finer subgrain sizes under equivalent deformation conditions, a result of recovery in subgrain boundaries slowed by higher C and O impurity content.

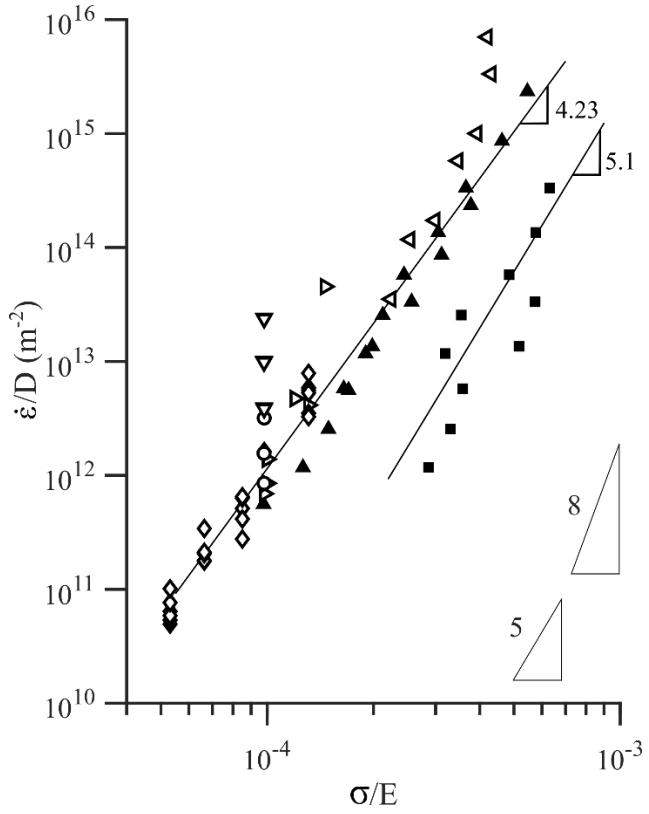

Figure 3.15: Strain rate normalized by independently measured diffusivity is plotted against stress normalized by the temperature-dependent unrelaxed dynamic elastic modulus on dual logarithmic scales for all available unalloyed niobium data. A plot legend and a list of data sources are provided in Table 3.3.

Table 3.3: Legend for symbols used in Figure 3.15.

Symbol	Author(s)	Reference
▷	Stoop, J. and Shahinian, P. (Heat CH)	[22]
○	Brinson and Argent	[7]
◁	Behera, A. N. *et al.*	[6]
◇	Stoop, J. and Shahinian, P.	[23]
▽	Rawson, J.D.W. and Argent, B.B.	[8]
▲	Type 1 Niobium	[21]
■	Type 2 Niobium, $\varepsilon = 0.15$	present study

A remaining mystery of the Type 2 niobium material is the abrupt decrease in flow stress with increasing temperature near 1673 K (1400°C), shown in Figures 3.2 and 3.3, which is accompanied by the low stress exponent shown for 1673 K (1400°C) in Figure 3.12. These effects might be interpreted as a change in deformation mechanism near 1673 K (1400°C). However, the Type 2 niobium data collapse onto approximately a single curve in Figures 3.13 through 3.15, which suggests a single deformation mechanism across the test temperatures. There might be changes in microstructure evolution, or even microstructure inhomogeneity, near 1673 K (1400°C), where microstructure was not characterized for the present study. The most likely suspect in such an effect is the dissolution or softening of some dispersoids in the vicinity of 1673 K (1400°C). The carbides most likely to form in the Type 2 niobium have high melting temperatures and are less likely to soften or dissolve than the oxides. The WO_3 oxide has a melting temperature of 1743 K (1470°C) [61], for example, and is one possible culprit. This might point to a difference in behaviors of oxide and carbide dispersoids with increasing temperature. The resolution of this mystery is left to future investigations. Using software to predict the thermal stability of expected oxides and carbides is recommended for future investigations.

CONCLUSIONS

The conclusions from the present study are:

1. Subgrains were observed and measured in Type 1 niobium after deformation at elevated temperatures, confirming that deformation was by five-power creep. This is consistent with all available data from the literature for low-impurity niobium.

2. Type 2 niobium does not reach steady state deformation under the test conditions studied and is approximately 1.8 times stronger than the Type 1 niobium. This is a result of the higher impurity content in the Type 2 niobium, primarily C and O, which likely form fine carbide and oxide dispersoids.
3. There is negligible plastic anisotropy within the Type 2 niobium sheet between the 0 and 90 degree orientations at 1773 K (1500°C).
4. The Type 2 niobium demonstrates a stress exponent near 5 and a deformation substructure containing subgrains. These observations are consistent with the five-power (dislocation-climb-controlled) creep mechanism of pure metals and Class II (M) alloys [32,60,62,63] .
5. Compared to the Type 1 niobium, the Type 2 niobium demonstrates: (i) delayed recrystallization, (ii) slower grain growth, (iii) inhomogeneous deformed microstructures, and (iv) slower recovery that leads to finer subgrains with less distinct boundaries. All these effects are consistent with the fine dispersoids expected from the higher C and O content of the Type 2 niobium.
6. The data presented demonstrate that the strengths of the Type 1 and Type 2 niobium are controlled by the substructure evolved during deformation, specifically the subgrain size. The high impurity content of the Type 2 niobium kept its subgrain size small. From the ratio of subgrain sizes between the Type 1 and Type 2 niobium after deformation at 1773 K (1500°C) and 10^{-3} s^{-1}, the five-power creep mechanism reasonably predicts the measured ratio of strengths between these materials. This

provides the first mechanistic explanation supported by data for how increased impurity content in a refractory metal increases strength at elevated temperature.

Chapter 4: HR-EBSD Technique Implementation

To better understand the mechanisms of deformation in niobium at elevated temperatures, it is necessary to understand the substructure developed during deformation. Subgrain boundaries can have very small misorientation angles, even less than 0.01° [14], but misorientations on the order of 0.01° and larger are expected to be relevant to deformation behaviors in niobium. The angular resolution of standard EBSD, ± 0.5° [11–13], is not sufficient to distinguish such low angle subgrain boundaries. HR-EBSD can improve the measurement of relative misorientation angles to ± 0.01° [12]. A goal of the present study is to use OpenXY to perform HR-EBSD analysis on deformed niobium. OpenXY [18] is an open source software toolbox for Matlab™ [64] that implements cross-correlation calculations for EBSD data to produce HR-EBSD results. The challenges encountered in using OpenXY to perform HR-EBSD analysis on the deformed niobium were: 1. OpenXY did not work for niobium, 2. data from the Thermo Fisher Scientific Scios 2 EBSD system, a new SEM/EBSD instrument installed in the Texas Materials Institute and used to acquire data for the present study, was not compatible with OpenXY, and 3. OpenXY could not be applied to heavily deformed grains that require more than one reference Kikuchi pattern. The solutions implemented to overcome these challenges are now described.

TECHNIQUE DEVELOPMENT

To perform HR-EBSD analysis using OpenXY a file is needed that describes the material in the EBSD scan. OpenXY did not have a material file for niobium. Thus, I created the needed material file. This material file includes the structure factors, F_{hkl}, the spacing between crystal planes, d_{hkl}, and the elastic stiffness constants, C_{11}, C_{12}, and C_{44}. The F_{hkl} for atomic electron scattering cannot be calculated using Crommer-Mann constants. Instead, the atomic scattering amplitudes for electrons were used to calculate the structure factors. These values were taken from the International Tables for Crystallography Vol C Chapter 4 [65]. The calculation of d_{hkl} values required the lattice parameter, which was taken from reference [66]. The elastic stiffness constants for niobium are from reference [47]. The OpenXY material file for niobium is provided in Appendix A along with details on how the F_{hkl} and d_{hkl} values were calculated. The material file I created for niobium is now included in the standard distribution of OpenXY, which is available to the larger research community.

The following are necessary to perform HR-EBSD analysis on an EBSD data set for niobium using OpenXY: the niobium material file, the Kikuchi patterns from the entire EBSD scan, a data file providing all EBSD data for pattern locations and indexing results (typical file types are .ctf, .cpr, and .ang), and a grain file generated to identify individual grains. The Thermo Fisher Scientific software provides the Kikuchi patterns and an EBSD data file but does not produce a grain file. The grain file is produced by segmenting the EBSD data to identify separate grains and assign each measurement position to a specific

grain. The grain file includes the Euler angles, x and y positions, image quality, confidence index, fit, grain ID, whether or not the point is in a grain on the edge of a scan, and the phase name. I produced a software script that uses MTEX [20], an open source software toolbox for Matlab^{TM} [64], to produce grain files from data acquired using the Thermo Fisher Scientific SEM/EBSD system. This script is provided in Appendix B.

Data from the Thermo Fisher Scientific system requires converting the EBSD data file it produces to the ".ang" format. It also requires the addition of pattern center values for the data to be used with OpenXY. The Thermo Fisher Scientific system saves the EBSD data in a proprietary file format (.ebsd). This must be converted to the .ang format. This conversion is performed by the EBSDFileConverter software provided by Thermo Fisher Scientific. The Thermo Fisher Scientific system provides pattern center values as x, y, and L as positions on the EBSD detector screen in millimeters. In contrast, OpenXY defines pattern center values as x, y, and z, and these values are based on cropped Kikuchi patterns (20 x 20 mm) and are given as fractions of the image width. With the help of Thermo Fisher Scientific, equations were developed to convert the Thermo Fisher Scientific pattern center values to the pattern center values used in OpenXY. These conversion equations are listed below:

$$PC_x = 0.5 + 0.5\left(\frac{PC_{TFx} - 15.8}{20}\right), \qquad (4.1)$$

$$PC_y = 1 - \left(\frac{PC_{TFy}}{20}\right), \qquad (4.2)$$

$$PC_z = (^{PC_{TFL}}/_{20}), \quad (4.3)$$

where PC represents pattern centers used in OpenXY and PC_{TF} represents pattern centers reported by Thermo Fisher Scientific software. These pattern center values are not saved in the converted .ang file and must be documented independently by the user. For the Thermo Fisher Scientific system, acquisition parameters that were successful for HR-EBSD analysis were: 1 x 1 binning, an exposure time of 115 ms, a gain of 0, an accelerating voltage of 20 kV, a working distance of approximately 10 mm, and a beam current of approximately 1.7×10^{-5} nA.

To make the Kikuchi patterns compatible with OpenXY, it was necessary to apply image processing to all the pattern images and change the image file names. Currently the Thermo Fisher Scientific software saves the Kikuchi patterns in a proprietary .zip-type file format (.pat). These Kikuchi patterns are unpacked using the third-party software "Thermo Extract PAT". Unfortunately, the Kikuchi patterns saved are not the Kikuchi pattern images after correction with a background image but are the uncorrected Kikuchi patterns. This means that it is critical for the user to save a background image from the same EBSD scan to properly process the Kikuchi pattern images. The background image must be saved before the scan is started because it is not saved in the Thermo Fisher Scientific EBSD data file and cannot be accessed after a scan is complete. The extracted Kikuchi pattern image files produced by the "Thermo Extract PAT" software are saved as 16-bit greyscale TIF files that contain data only 8-bits deep. When viewed directly, these images appear as all black, but appropriate image processing will reveal the data contained in these images.

Note that the “Thermo Extract PAT” software provides an option to produce 8-bit files, but this option should not be used. Both background subtraction and brightness/contrast corrections must be applied to all the Kikuchi pattern images extracted from the .pat file. The script written and used to correct the Kikuchi pattern images using the ImageJ [67] open source software package is provided in Appendix C. OpenXY was not able to properly read in the Kikuchi pattern files with the naming scheme “X = #, Y = #.tif” created from the “Thermo Extract PAT” software, where X and Y are the x and y positions from the EBSD data file. With help from the developers and maintainers of OpenXY, a naming scheme for Kikuchi pattern image files was created that OpenXY was able to read in successfully. The naming scheme adapted is “Name_r[#y]c[#x].tif”, where [#y] and [#x] are replaced with the integer values designating the y and x position within a scan from which the specific Kikuchi pattern in the named file was acquired. The script used to convert all the Kikuchi pattern file names to this new naming scheme is provided in Appendix D. Detailed instructions on how to collect and process HR-EBSD data using a Thermo Fisher Scientific EBSD system and OpenXY software are provided in Appendix E.

When the Kikuchi patterns acquired using EBSD shift significantly within a single grain, an effect that can be caused by large deformation gradients within the grain, the cross-correlation calculations used for HR-EBSD analysis may not work properly. This became an issue when using OpenXY to perform HR-EBSD analysis on the deformed Type 2 niobium, which has finer and less distinct subgrains than the Type 1 niobium. To simulate selecting multiple reference patterns within the same grain, the HR-EBSD analysis was run

multiple times on the same dataset. Each time the HR-EBSD analysis was run, a new reference pattern was selected from an area that did not produce proper cross-correlation results in the previous run. This new technique of piece-wise HR-EBSD analysis was repeated until cross-correlation calculations were successful across the entire EBSD dataset. The HR-EBSD results from these separate calculations were joined to produce a single output file of HR-EBSD data for the original EBSD scan. Appendix F provides a full description for how regions of data from the EBSD data file were mapped to multiple HR-EBSD analyses and how the results of those piece-wise analyses were combined to produce a single output file of HR-EBSD data. The Matlab™/MTEX script which compiled the HR-EBSD datasets is provided in Appendix G.

TECHNIQUE IMPLEMENTATION

After collecting the EBSD data and Kikuchi patterns from the Thermo Fisher Scientific system, MTEX is used to segment the grains. The grains are segmented to create the grain file needed by OpenXY[2] for HR-EBSD analysis. This grain file identifies for OpenXY the grain to which each scan position belongs. Figure 4.1 shows an IPF map produced using MTEX, for which the segmented grain boundaries are indicated by black curves.

[2] The OpenXY version used is the version current as of March 2021

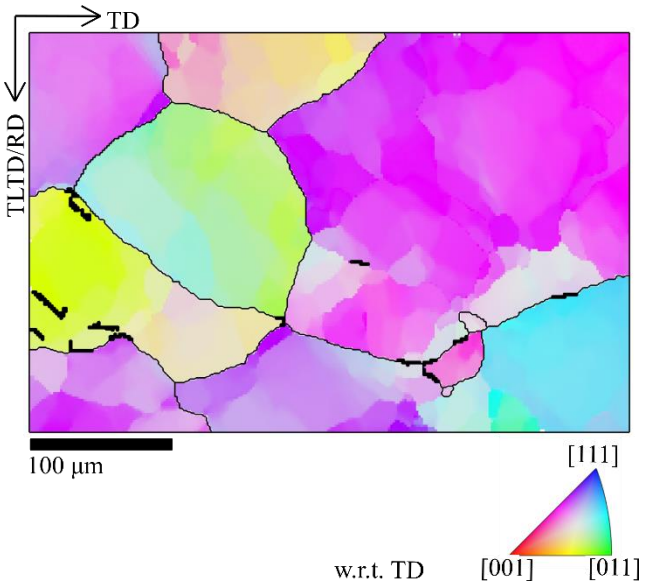

Figure 4.1: An IPF map is shown with respect for the TD of Type 2 niobium tested at 1773 K (1500°C) at 10^{-3} s^{-1} with a 90 degree orientation. These results were produced from standard EBSD data.

HR-EBSD analysis is then performed using OpenXY, which uses the EBSD data and the grain file generated by MTEX. MTEX is used to produce IPF maps, reference orientation deviation (ROD) maps, and other important data visualization from the HR-EBSD results produced by OpenXY. From the IPF maps, it is apparent where in the dataset the cross-correlation method worked properly and where it did not. For the example in Figure 4.2, the Type 2 niobium tested at 1773 K (1500°C) at 10^{-3} s^{-1} for a 90 degree orientation, the IPF map generated from OpenXY HR-EBSD results has areas where the cross-correlation calculations clearly worked well. It also demonstrates areas where the cross-correlation calculations clearly failed. These areas are characterized by abrupt changes in the orientation calculated between adjacent or nearby points. These are evident as a visual pixilation in the IPF map, as shown in Figure 4.2. The cross-correlation calculations fail when the chosen reference Kikuchi pattern is too far away in orientation from the pattern of the position at which the calculation is attempted. This issue arises

especially in highly deformed grains containing large strain gradients. To correct areas where the cross-correlation method does not work, the same EBSD data and same grain file are used to perform multiple independent HR-EBSD analyses using OpenXY. Each HR-EBSD analysis addresses a small area with similar orientations and uses a reference Kikuchi pattern from that area. The example EBSD dataset is analyzed using eight separate HR-EBSD calculation applications. Eight separate HR-EBSD analyses are needed to ensure the cross-correlation method works over the entire scan area. The number of HR-EBSD analyses needed will undoubtedly vary for different datasets. The data from each of the eight runs is presented in Figure 4.3, where the blacked-out regions represent data not used in the specific HR-EBSD run.

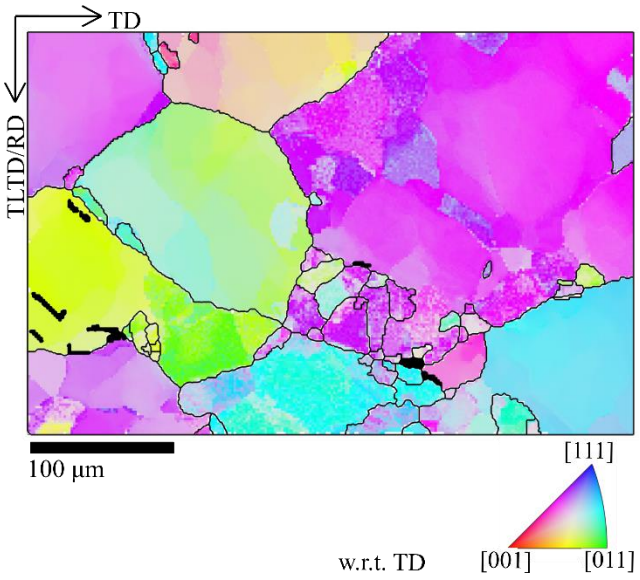

Figure 4.2: An IPF map is presented from the first HR-EBSD analysis demonstrating the areas where the cross-correlation calculation worked and areas where the cross-correlation calculations failed.

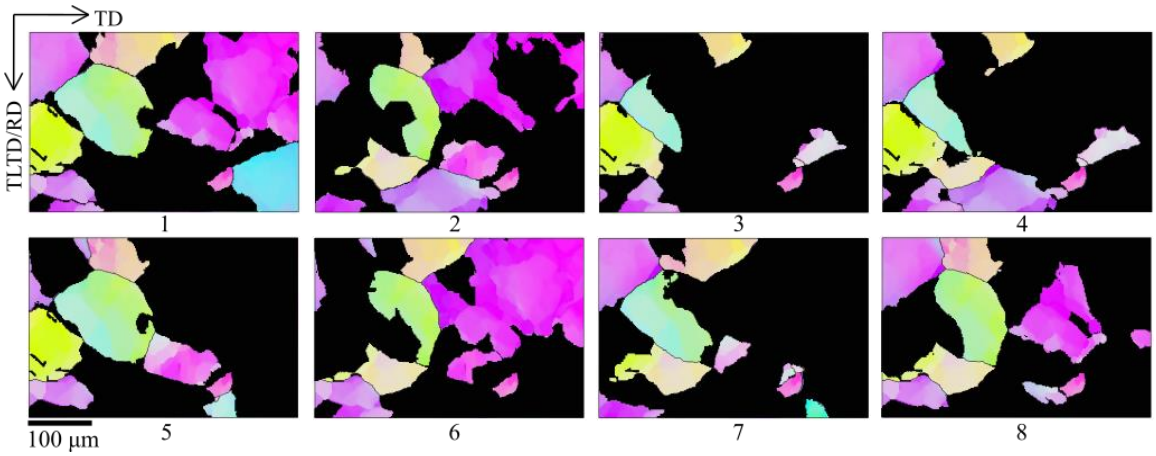

Figure 4.3: Data used for each of the eight HR-EBSD analyses are presented. The data not used for each analysis are in black, and the data used are in the IPF colorization. The number of the HR-EBSD analysis is listed below the respective IPF map.

This EBSD dataset requires multiple HR-EBSD analyses because of a significant strain gradient leading to large variations in Kikuchi patterns within a single grain. The Kikuchi patterns from different areas in a large grain shown in Figure 4.4 demonstrate that the Kikuchi patterns within this grain vary significantly. This explains why the cross-correlation method was unable to accurately correct all the points within that grain using only one reference Kikuchi pattern. From these HR-EBSD analyses, a single HR-EBSD result is created using the data taken from each of the HR-EBSD analyses shown in Figure 4.3. To avoid overlapping data when multiple HR-ESBD analyses provide good results, priority is given to the earliest HR-EBSD data analysis by the enumeration presented in Figure 4.3. For example, if a point is good in HR-EBSD data analyses 1, 3, and 8, then the data from HR-EBSD analysis 1 is used in the final HR-EBSD data file.

IPF and reference orientation deviation (ROD) maps are produced from the HR-EBSD data using MTEX. Figure 4.5 shows an IPF map from the HR-EBSD result. This IPF map is similar to the result from the standard EBSD data. However, when the standard

EBSD and HR-EBSD result are compared in Figure 4.6, it is shown that the HR-EBSD data enables the detection of two new grain boundaries. One of these newly detected boundaries is marked in Figure 4.6. This new grain boundary is likely detected because it has a misorientation in the EBSD data of just slightly less than 5 degrees, the misorientation threshold used for grain segmentation in the MTEX analysis. The improvement of measurement for relative misorientation angles provided by the HR-EBSD analysis pushes the boundary over the 5 degree misorientation threshold, making it detected by MTEX in the HR-EBSD data. This conveys the importance of HR-EBSD analysis for determining grain sizes in deformed materials. This new grain boundary directly impacts the ROD map shown in Figure 4.7. The standard EBSD ROD map shows much deviation from the grain average orientation in the bottom right corner of the scan, while the HR-EBSD ROD map shows much less deviation from the average orientation in the newly segmented grain. This is because the standard EBSD ROD map perceives the two grains as one grain, which results in large deviations from the average orientation calculated for the large single grain.

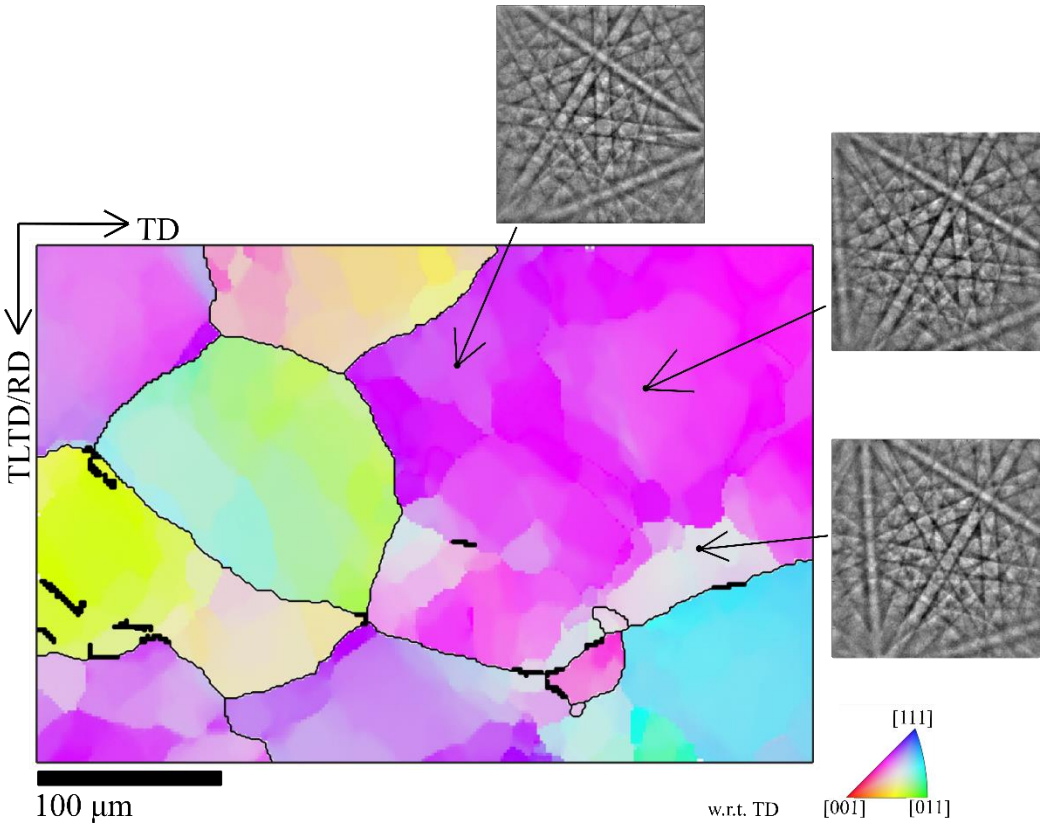

Figure 4.4: An IPF map is shown with respect to the TD for Type 2 niobium tested at 1773 K (1500°C) at 10^{-3} s^{-1} with a 90 degree orientation. Kikuchi patterns are presented for three different locations within a single grain, marked by a dot and an arrow pointing to the dot.

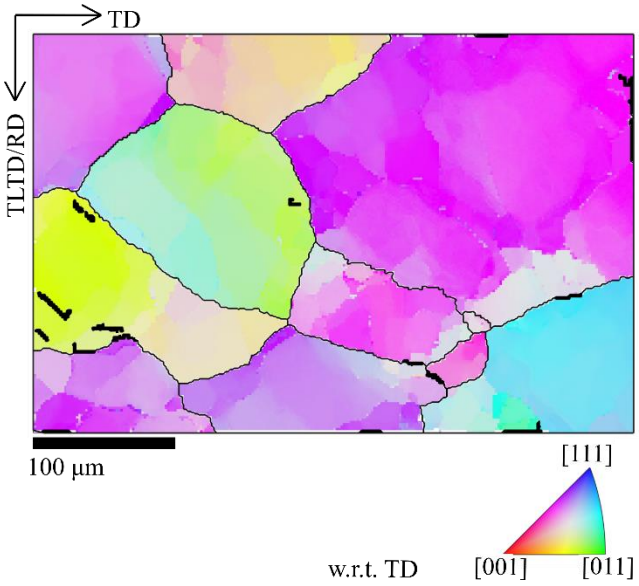

Figure 4.5: An IPF map is shown with respect to the TD for Type 2 niobium tested at 1773 K (1500°C) at 10^{-3} s^{-1} with a 90 degree orientation. These results are from eight HR-EBSD analyses of a single EBSD dataset.

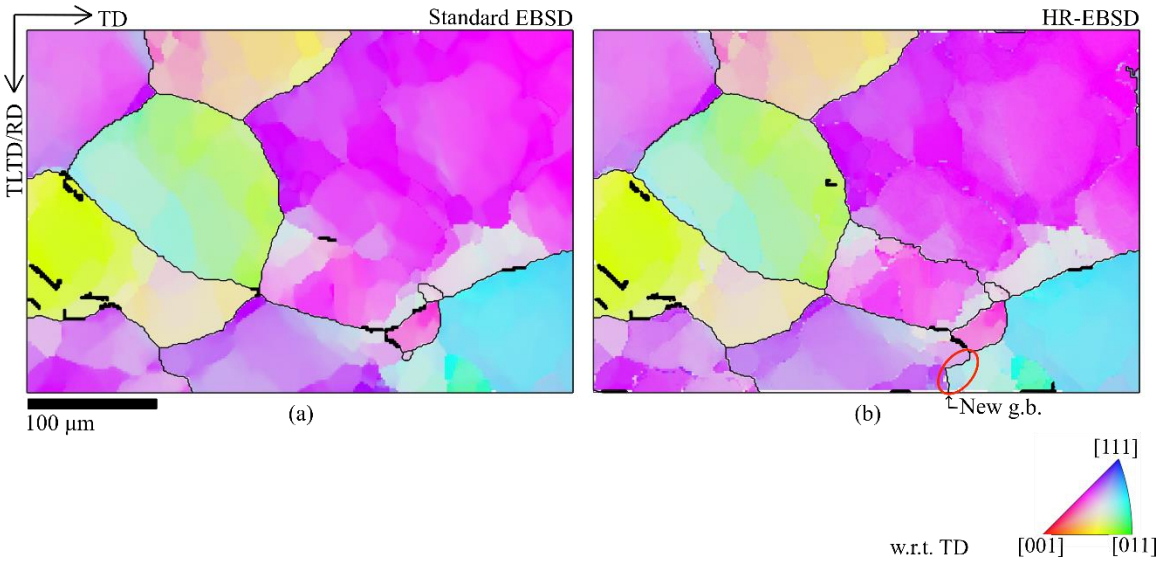

Figure 4.6: IPF maps are shown with respect to the TD for Type 2 niobium tested at 1773 K (1500°C) at 10^{-3} s^{-1} with a 90 degree orientation. On the left (a) are results from the standard EBSD data, and on the right (b) are results from the HR-EBSD analysis. A new grain boundary, identified using the HR-EBSD data, is circled in red and labeled in (b).

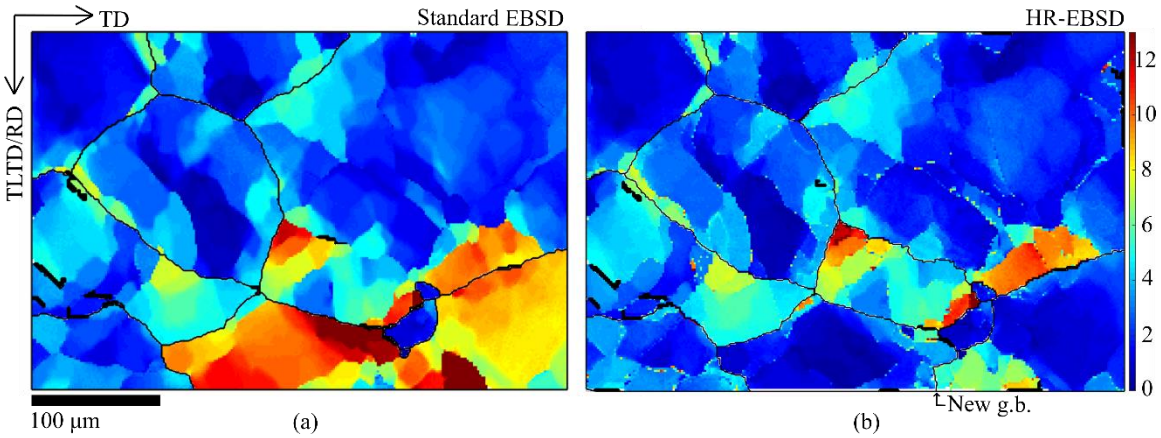

Figure 4.7: ROD maps are presented for Type 2 niobium tested at 1773 K (1500°C) at 10^{-3} s^{-1} with a 90 degree orientation. On the left (a) are results from the standard EBSD data, and on the right are (b) results from the HR-EBSD analysis. A new grain boundary, identified using the HR-EBSD data, is labeled in (b).

This HR-EBSD analysis technique provides a method for detecting subgrain boundaries in deformed materials. Figure 4.8 shows the HR-EBSD IPF map of the deformed Type 2 niobium shown previously. It also shows a map of grain boundaries (indicated as black curves) and subgrain boundaries (indicated as blue curves) and an HR-EBSD IPF map overlaid with the grain and subgrain boundaries identified. The grain and subgrain boundary segmentations are performed on the HR-EBSD data in MTEX using a 5 degree misorientation threshold for the grain boundaries and a 0.2 degree misorientation threshold for the subgrain boundaries. To determine a reasonable subgrain misorientation threshold, misorientation angles from 0.1 to 0.5 degrees were tested. The 0.2 degree threshold is the smallest misorientation that produces reasonable subgrain boundary segmentation for this dataset. The subgrain average area was measured from Figure 4.8 and converted to a lineal intercept size using the equation [31] described in

Chapter 3 [54] to produce a value of 15.6 μm with a standard deviation of 7.8 μm. This measurement is close to the subgrain size measured in Chapter 3, λ_2 = 18.4 μm, for the Type 2 niobium with a 0 degree orientation tested under the same conditions. Figure 4.8 demonstrates the successful identification and segmentation of subgrains in the deformed Type 2 niobium. This achieves the primary goal of the technique development undertaken in this work and is the first known demonstration of subgrain quantification using EBSD data. The technique of producing OpenXY HR-EBSD results and using MTEX to segment subgrain boundaries is expected to be useful in probing the relationships at the intersections of subgrain and grain boundaries. These relationships are a great avenue for future work.

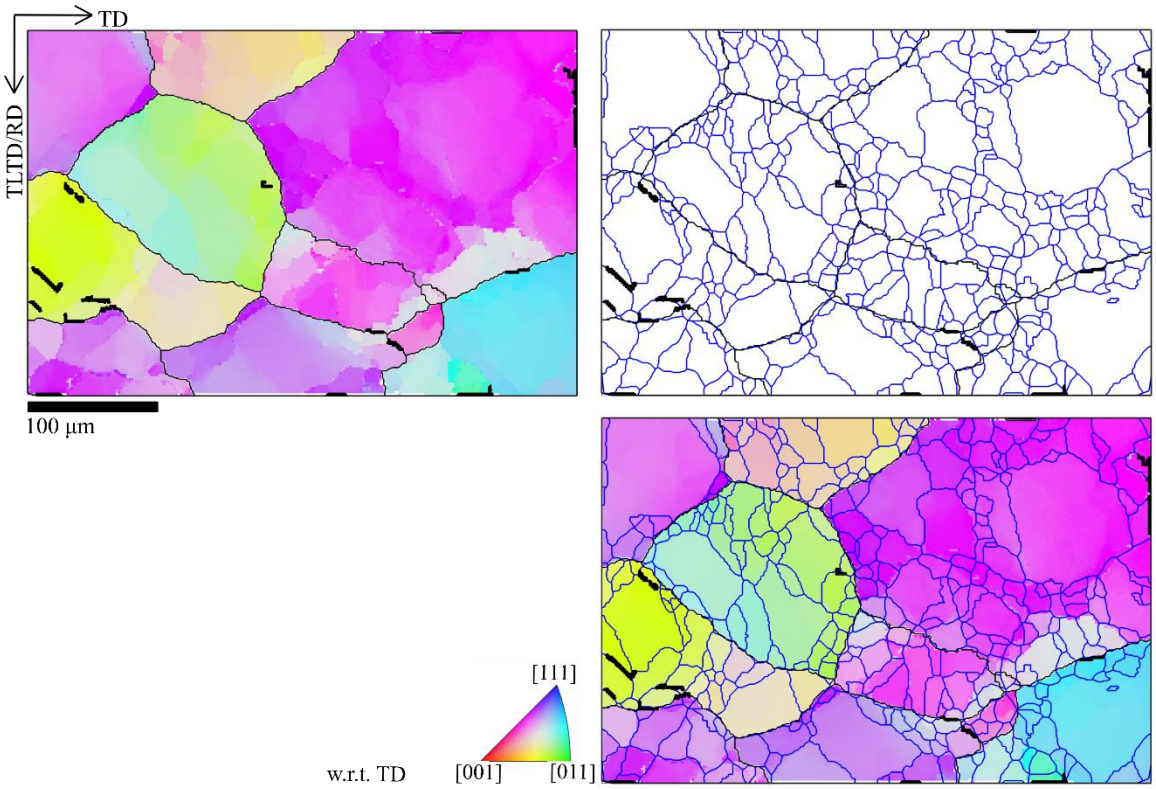

Figure 4.8: Results of subgrain segmentation from HR-ESBD data using MTEX are presented. On the left is the IPF map with grain boundaries indicated as black curves. At the upper right is a map of grain and subgrain boundaries. Grain boundaries (misorientation threshold of 5 degrees) are indicated as black curves. Subgrain boundaries (misorientation threshold of 0.2 degrees) are indicated as blue curves. At the bottom right, the grain and subgrain boundaries are overlaid onto the IPF map.

Chapter 5: Conclusions and future work

CONCLUSIONS

The following are major results and conclusions from this work:

1. A recommended temperature-dependent unrelaxed dynamic Young's elastic modulus for randomly textured polycrystalline niobium is produced from a compilation of all the available data for elastic modulus of polycrystalline niobium in the literature.
2. Based on the stress exponent, the activation energy, good agreement with high-purity niobium data from the literature, and the presence of subgrains after deformation, high-purity niobium and Type 1 niobium deform by the five-power creep mechanism.
3. Even though the Type 2 niobium does not reach steady-state deformation for the conditions investigated, because of a stress exponent close to 5 and the presence of subgrains after deformation, the Type 2 niobium likely undergoes five-power creep deformation.
4. Type 2 niobium is approximately 1.8 times stronger than the Type 1 niobium. This is a result of the Type 2 niobium's higher impurity content, particularly the C and O which likely form fine dispersoids.
5. Compared to the Type 1 niobium, the higher impurity content of the Type 2 niobium results in slower recrystallization, slower grain growth, slower recovery, and inhomogeneous deformed microstructures. Because of the slower recovery,

the Type 2 niobium has finer and less distinct subgrains compared to the Type 1 niobium.

6. The five-power creep mechanism accurately predicts the ratio of strengths at 1773 K (1500°C) and 10^{-3} s^{-1} from the ratio of subgrain sizes, demonstrating that the strengths of the Type 1 and Type 2 niobium are controlled by the substructure evolved during deformation, which is controlled by the impurity content. This is the first mechanistic explanation with supporting data for how increased impurity content increases strength in refractory metals at elevated temperature.

7. An HR-EBSD technique that compiles multiple corrected HR-EBSD files into a single data file was successfully implemented. This technique addresses microstructures where the Cross-Correlation method is unable to accurately index an entire grain because of the large variation in Kikuchi patterns inside the grain. The resulting HR-EBSD data were used to produce the first known quantitative measurement of subgrains by segmentation from EBSD data.

SUGGESTIONS FOR FUTURE WORK

1. Apply the HR-EBSD technique developed to other studies and systems.
2. Investigate the effect impurity content has on the deformation behaviors in other refractory metals, such as tantalum and molybdenum, to determine if the behaviors in those materials can also be explained using the five-power creep mechanism, as done for niobium.

3. Investigate niobium alloys to determine if the new understanding developed for the relationship between microstructure and high-temperature plastic flow, based on the five-power creep mechanism, can also explain the increased deformation resistance in alloys.
4. TEM work on the deformed niobium would be useful to identify the carbides and oxides that are predicted by previous studies and the present study.

Appendices

Appendix A

F_{hkl} and d_{hkl} calculations, and niobium material file

To calculate the spacing between crystal planes, d_{hkl}, the equation for a cubic system was used:

$$1/d_{hkl}^2 = (h^2 + k^2 + l^2)/a^2 , \quad \text{(A.1)}$$

where a is the lattice parameter. For niobium the lattice parameter was taken from "Elements of X-Ray Diffraction" 2nd edition by B.D. Cullity pg 507 [66].

To calculate the structure factor, F_{hkl}, for body-centered cubic materials the following equation was used:

$$F_{hkl} = 2 * f_a e^{2\pi(hx+ky+lz)} , \quad \text{(A.2)}$$

where f_a is the atomic scattering factor, and the real part of $e^{2\pi(hx+ky+lz)}$ is equal to 1 (real part: $F_{hkl} = 2 * f_a$). This equation is for when h+k+l is even. When h+k+l is odd F_{hkl} is 0.

The atomic scattering factor is a function of $sin\theta/\lambda$, which can be solved for using the following equation:

$$sin\theta/\lambda = 1/2d_{hkl} , \quad \text{(A.3)}$$

The EBSD atomic scattering factor cannot be calculated using Cromer-Mann Constants like in X-Ray diffraction. Instead, atomic scattering amplitudes for EBSD as a function of $sin\theta/\lambda$ can be found in the International Tables for Crystallography Vol C Chapter 4 (Table 4.3.1.1) [65] for neutral atoms.

Atomic scattering factors were calculated by interpolating values from Table 4.3.1.1 to solve for f_a, then used to solve for F_{hkl}:

$$F_{hkl} = 2 * f_a , \quad \text{(A.4)}$$

Table A.1: Example calculations of d_{hkl} and F_{hkl} for Niobium

h	k	l	$1/d_{hkl}^2$	d_{hkl}	Sin(θ)/λ	f(Nb)	H+K+L	F_{hkl}

0	-1	1	1.83E-01	2.338189993	0.213840621	4.918575	0	9.837
0	-2	0	3.66E-01	1.65335	0.302416306	3.509884	-2	7.020
1	-2	-1	5.49E-01	1.349954622	0.37038282	2.785516	-2	5.571
0	-2	2	7.32E-01	1.169094997	0.427681242	2.325231	0	4.650
0	-3	1	9.15E-01	1.045670354	0.478162165	2.001935	-2	4.004
2	-2	-2	1.10E+00	0.954562068	0.523800408	1.770186	-2	3.540
1	-3	-2	1.28E+00	0.883752749	0.565769103	1.584816	-4	3.170
0	-4	0	1.46E+00	0.826675	0.604832613	1.436536	-4	2.873

Below is the niobium material file created for OpenXY.

```
Material          Niobium
Fhkl        9.837 7.020 5.571 4.650 4.004 3.540 3.170 2.873
hkl         0 -1 1 0 -2 0 1 -2 -1 0 -2 2 0 -3 1 2 -2 -2 1 -3 -2 0 -4 0
C11         245
C12         132
C44         28.4
lattice           cubic
dhkl        2.338e-10 1.653e-10 1.35e-10 1.169e-10 1.046e-10 9.546e-11
8.838e-11 8.267e-11
axs         3
C13
C33
C66
Burgers           2.86e-10
a1          3.3067
b1          3.3067
c1          3.3067
```

Appendix B

Grain File Script

Below is the grain file script run in Matlab R2019b using the MTEX version 5.6.0.

```
function export_GrainFile(ebsd,fName, edgesList, phaseList, varargin)
% Export EBSD data to TSL/EDAX text file (ang).
%
% Syntax
%   export_ang(ebsd,fName,varargin)
%
% Input
%  ebsd  - @EBSD
%  fName - Filename, optionally including relative or absolute path
%  edgesList - list of edges; 1 for grains at edges, 0 for interior
grains
%  phaseList - list of phases
%
% Flags
%  flipud - Flip ebsd spatial data upside down (not the orientation
data)
%  fliplr - Flip ebsd spatial data left right (not the orientation
data)
%

setMTEXpref('EulerAngleConvention','Bunge')
fprintf('EBSD data x(2) is %d\n', ebsd.prop.x(2));
fprintf('EBSD data y(2) is %d\n', ebsd.prop.y(2));

roundOff = 3; %Rounding coordinates to 'roundOff' digits

scrPrnt('SegmentStart','Exporting ''txt'' file');

% pre-processing
scrPrnt('Step','Collecting data');

ebsd.phaseMap = ebsd.phaseMap - (min(ebsd.phaseMap)+1); %Adapt *.ang
phase map convention
if check_option(varargin,'flipud') %Flip spatial ebsd data
  ebsd = flipud(ebsd);
  scrPrnt('Step','Flipping EBSD spatial data upside down');
end
if check_option(varargin,'fliplr') %Flip spatial ebsd data
  ebsd = fliplr(ebsd);
  scrPrnt('Step','Flipping EBSD spatial data left right');
end

%clearing previous ebsdGrid variable *see if this fixes things
clearvars ebsdGrid
% get gridified version of ebsd map
```

```
ebsdGrid = ebsd.gridify;


fprintf('EBSD grid data x(2) is %d\n', ebsdGrid.prop.x(2));
fprintf('EBSD grid data y(2) is %d\n', ebsdGrid.prop.y(2));

% Open txt file
scrPrnt('Step','Opening file for writing');
filePh = fopen(fName,'w'); %Open new txt file for writing

% Write header
scrPrnt('Step','Writing file header');

% Write SEM info
fprintf(filePh,'# Header: ProjectName \n');
fprintf(filePh,'# \n');
fprintf(filePh,'# Partition Formula: \n');
fprintf(filePh,'# Grain Tolerance Angle: 5.00 \n');
fprintf(filePh,'# Minimum Grain Size: 5 \n');
fprintf(filePh,'# Minimum Confidence Index: 0.00 \n');
fprintf(filePh,'# Multiple Rows Requirement: Off \n');
fprintf(filePh,'# Column 1-3: phi1, PHI, phi2 (orientation of point in
radians) \n');
fprintf(filePh,'# Column 4-5: x, y (coordinates of point in microns)
\n');
fprintf(filePh,'# Column 6:   IQ (image quality) \n');
fprintf(filePh,'# Column 7:   CI (confidence index) \n');
fprintf(filePh,'# Column 8:   Fit (degrees)\n');
fprintf(filePh,'# Column 9:   Grain ID (integer)\n');
fprintf(filePh,'# Column 10:  edge (1 for grains at edges of scan and 0
for interior grains)\n');
fprintf(filePh,'# Column 11:  phase name \n');


scrPrnt('Step', 'ebsdGrid dx', (ebsdGrid.dx))
scrPrnt('Step', 'Ncols odd', (ebsdGrid.size(2)-1))


%Get data order x
if ebsdGrid.prop.x(1,1)< ebsdGrid.prop.x(1,2)
  dim.x = 2;
elseif ebsdGrid.prop.x(1,1)> ebsdGrid.prop.x(1,2)
  dim.x = -2;
elseif ebsdGrid.prop.x(1,1)< ebsdGrid.prop.x(2,1)
  dim.x = 1;
elseif ebsdGrid.prop.x(1,1)> ebsdGrid.prop.x(2,1)
  dim.x = -1;
end
%Get data order y
if ebsdGrid.prop.y(1,1)< ebsdGrid.prop.y(1,2)
  dim.y = 2;
elseif ebsdGrid.prop.y(1,1)> ebsdGrid.prop.y(1,2)
  dim.y = -2;
```

```
elseif ebsdGrid.prop.y(1,1)< ebsdGrid.prop.y(2,1)
  dim.y = 1;
elseif ebsdGrid.prop.y(1,1)> ebsdGrid.prop.y(2,1)
  dim.y = -1;
end

fprintf('EBSD grid data after order x(2) is %d\n', ebsdGrid.prop.x(2));
fprintf('EBSD grid data after order y(2) is %d\n', ebsdGrid.prop.y(2));

%Gather data
% Changed this from RAW data export
flds{1} = ebsd.rotations.phi1;
flds{2} = ebsd.rotations.Phi;
flds{3} = ebsd.rotations.phi2;
flds{4} = ebsd.prop.x;
flds{5} = ebsd.prop.y;
flds{6} = ebsd.prop.iq;
flds{7} = ebsd.prop.ci;
flds{8} = ebsd.prop.fit;
flds{9} = ebsd.grainId;
flds{10} = edgesList;
flds{11} = phaseList;


% Find empty coordinates in hexGrid
idDel = false(size(ebsdGrid));
if length(ebsd.unitCell)==6 %hex Grid
    idDel(:,end) = true;
    idDel(2:2:end,end-1) = true;
end

%Write data
phi1 = round(ebsd.rotations.phi1, 6);
Phi = round(ebsd.rotations.Phi, 6);
phi2 = round(ebsd.rotations.phi2, 6);
x = round(ebsd.prop.x, 6);
y = -round(ebsd.prop.y, 6);
IQ = ebsd.prop.iq;
CI = ebsd.prop.ci;
Fit = ebsd.prop.fit;
GrainID = ebsd.grainId;
edge = edgesList;
phase = phaseList;

A = zeros(ebsdGrid.length,11); %initialize
% A = zeros(length(flds{1}),10); %initialize
for i = 1:length(flds)
  temp = flds{i};
  temp(idDel) = nan;
  %Transpose matrices if required
  if abs(dim.x) == 2 && abs(dim.y) == 1
    temp = temp';
  end
```

```
  %Flip matrices if required
  if dim.x < 0, temp = fliplr(temp); end
  if dim.y < 0, temp = flipud(temp); end
  fprintf('Flds # is %d\n', i);
  %Make vector
  A(:,i) = temp(:);
end


%Fix coordinates
A(all(isnan(A),2),:) = [];        % Delete empty coordinates from hex
grid
A(isnan(A)) = 0;                  % Set remaining NaN values to 0
A(:,4) =  A(:,4) - A(1,4);        % Set first x-value to 0
A(:,5) =  A(:,5) - A(1,5);        % Set first y-value to 0
A(:,4) = round(A(:,4),roundOff);  % Round of x-values
% write data array
scrPrnt('Step','Writing data array to ''ang'' file');
%fileID = fopen(filePh, 'w');

varNames = {'phi1', 'Phi', 'phi2', 'x', 'y', 'IQ', 'CI', 'Fit',
'GrainID', 'edge', 'phase'};
A2 = table(phi1, Phi, phi2, x, y, IQ, CI, Fit, GrainID, edge, phase,
'VariableNames', varNames);
%sort the table so that x steps before y
A3 = sortrows(A2, {'y', 'x'});
writetable(A3, fName, 'delimiter', ' ', 'WriteVariableNames', false,
'WriteRowNames', false);
%
fprintf(filePh ,'%9.5f %9.5f %9.5f %12.5f %12.5f %6.1f %6.3f %2.0f %6.0
f %6.3f %11.6f\n',A.');


% close ctf file
scrPrnt('Step','Closing file');
fclose(filePh );
scrPrnt('Step','All done',filePh );

end

% *** Function scrPrnt - Screen Printing
function scrPrnt(mode,varargin)
%function scrPrnt(mode,varargin)
switch mode
  case 'SegmentStart'
    titleStr = varargin{1};
    fprintf('\n-----------------------------------------------------
');
    fprintf(['\n     ',titleStr,' \n']);
    fprintf('-----------------------------------------------------
\n');
  case 'Step'
```

```
    titleStr = varargin{1};
    fprintf([' -> ',titleStr,'\n']);
  case 'SubStep'
    titleStr = varargin{1};
    fprintf(['    - ',titleStr,'\n']);
end
end
```

Appendix C

Kikuchi Pattern Image Processing Script

Below is the script run in ImageJ version 1.53c that performs image corrections on all the Kikuchi patterns in one folder.

```
//First need to correct background image to match bit number of kikuchi
tiff files (Image ->Type)
//then need to go to Image -> adjust -> Brightness/Constrast -> Hit
auto and then apply
//save new background image. That is the one we will use in this script
open("D:/EBSD Data/N205D/N205DF/Area
10/Background_N205DF_exp115_Gain0_20kV_0_10uA_2_16bit_withThresholdCorr
ected.tif");
dir1 = getDirectory("D:/EBSD Data/N205D/N205DF/Area 10/EBSPs Renamed");
dir2 = getDirectory("D:/EBSD Data/N205D/N205DF/Area 10/EBSPs Corrected
Method 2 20210830");
list = getFileList(dir1);
setBatchMode(true);
for (i=0; i<list.length; i++) {
//for (i=0; i<1; i++) {
      open("D:/EBSD Data/N205D/N205DF/Area
10/Background_N205DF_exp115_Gain0_20kV_0_10uA_2_16bit_withThresholdCorr
ected.tif");
      rename("background");
      showProgress(i+1, list.length);
      open(dir1+list[i]);
      title = getTitle();
      //title = getImageID();
      print("now working on..." + title);
      rename("XX");
      // Correct brightness contrast on individual kikuchi pattern
      run("Enhance Contrast", "saturated=0.35");
      run("Apply LUT");
      filename = dir1 + list[i];
      print("about to do subtraction");
      imageCalculator("Subtract 32-bit", "XX","background");
      print("finished image subtraction");
      selectWindow("Result of XX");
      setOption("ScaleConversions", true);
    run("16-bit");
      run("Enhance Contrast", "saturated=0.35");
      //selectWindow("Result of XX");
      run("Apply LUT");
      rename("result");
      //run("Close");
      outFile = dir2+File.separator+title;
      selectWindow("result");
      saveAs("Tiff", outFile);
      //run("Close");
```

```
      print("Done");
      run("Close All");
      //close();
}
print("All done");
```

Appendix D

Renaming Script for Kikuchi TIF files

Below is the script run in Matlab R2019b that renames all the Kikuchi files in a folder extracted using “Thermo Extract PAT” using the naming scheme “Name_r[#y]c[#x].tif” where [#y] and [#x] describe the position of the Kikuchi pattern in the EBSD scan and are taken from the original naming scheme used by “Thermo Extract PAT”, “X = [#x], Y = [#y].tif”.

```
%script to rename tif files
%format SpecimenName_r#c#
% r is row (y) and c is column (x)
%This takes the file names that ThermoPAT extracter spits out and
renames
%them so OpenXY can understand the format and ordering of the images
with
%respect to the ang file

%path to folder
d = 'D:\EBSD Data\N205D\N205DF\Area 10\EBSPs';  % path to files
d3 = 'D:\EBSD Data\N205D\N205DF\Area 10\EBSPs Renamed';

files = dir(fullfile([d], '*.tif'));
files = {files(~[files.isdir]).name};

%rename in the loop
for id = 1:length(files)+1
% get the file name
    oldname = files{id};
    xpos = extractBetween(oldname, 'X=', ';');
    ypos = extractBetween(oldname, 'Y=', '.tif');
    newname = sprintf('N205DFArea10_r%sc%s.tif', ypos{1}, xpos{1});
    movefile(fullfile(d, files{id}), fullfile(d3, newname))

end
```

Appendix E

Instructions for EBSD data collection using Thermo Fisher Scientific system and HR-EBSD analysis using OpenXY

On PathFinder (at EER computer)

1. Before starting the scan:
    a. Right click on the background image and save as a .tif file. This is import because the kikuchi patterns saved are not the corrected kikuchi patterns.
    b. Check "Save Patterns to Disc" before acquiring the EBSD data. This saves the kikuchi patterns from the scan in the pat file.
2. Save/record the pattern center values (x,y,l). These are found in the View -> Attributes -> EBSD tab in Pathfinder.
3. Open EBSDFileConverter on the Pathfinder computer and convert the ebsd file to an ang file.
4. Upload the ang and pat files to Google drive or UT Box. UT Box does have a file limit so uploading to Google Drive might be the only option.

In the Office

1. Extract the kikuchi patterns:
    a. Open ThermPAT/Thermo Extract PAT software.
    b. Click "Extract EBSPs from PAT file" and select .pat file from scan
    c. Check "Force 8-bit EBSP to 16-bit Word". This creates a new folder called "EBSPs" in the directory where the ang file. Note: extracted kikuchi patterns will have an 8-bit threshold despite being 16-bit files. This results in completely black images. The kikuchi patterns are still there, this will be remedied in ImageJ/FIJI.
2. Rename the kikuchi patterns

a. Open “RenameTifFiles.m” in Matlab. Make sure to change the directories to match the “EBSPs” directory and the new directory where the renamed images should go, and change the SpecimenName in the for loop.
b. Run this program to rename all the kikuchi patterns. This takes the images in one folder, renames them using the format “SpecimenName_rycx.tif” where r is the row (y value) and c is the column (x value), and moves these renamed files to a new directory.

3. Kikuchi image processing: correct threshold and subtract the background
    a. Open ImageJ/FIJI. Open your background image. If not a 16-bit image, go to Image -> Type and select 16-bit. Then go to Image -> Adjust -> Brightness/Contrast. In the B&C window, click “Auto” to auto adjust and click “Apply”. Save this corrected background image.
    b. Open ImageJ/FIJI. File -> Open -> “Kikuchi_Correction_Method2.ijm”
        i. This program takes each kikuchi pattern, auto corrects the Brightness/Contrast (like in a.), then subtracts the corrected background image and creates a 32-bit float result, changes the result to a 16-bit image and auto corrects the Brightness/Contrast. This final image gets saved to the new directory.
    c. Make sure to update the directories at the beginning of the file to the directory with the renamed kikuchi images and to the directory where you want the image corrected kikuchi tifs to go. Also change the background image location (line 12) to the corrected background image.
    d. Hit Run and select the directory for Renamed EBSPs and then select the directory for the Corrected EBSPs (this should be a blank folder you created). This process can take awhile (mine with 43520 images, took 30

minutes on the ETC desktop computer). Make sure to check some of the corrected images to see that the kikuchi lines match the original image.

4. Create Grain File for ang file
    a. Open Grain Analysis for "N205DF_Area10" and navigate to the MTEX folder. This file, opens the ang file, segments the grains (5 degree misorientation) and creates a grain file. The "export_GrainFile" function created by Emily Brady is needed to run this program.
    b. Note: the header for the Grain file isn't included in the current code, but can be manually added from the example. Also lines with data in both files should match the number of kikuchi patterns.
        i. It is critical for the Grain file and ang file to step up by x first then y (i.e. $x_1 = 0$ $y_1 = 0$, $x_2 = 1.6$ $y_2 = 0$)
5. Run OpenXY
    a. Set OpenXY code folder as current folder in Matlab
    b. Open and run MainGUI.m
        i. "Select Scan File" select original ang file from ThermoFisher. Make sure file name is ang and not ANG. To change to ang: right click on file -> Properties and change .ANG to .ang.
        ii. Manually select matching grain file created in step 4.
        iii. If "material detection failed" pops up, manually select material (in my case Nb for both indexed and non-indexed points).
        iv. "Select First Image" go to corrected kikuchi patterns and select the first pattern in the folder.
        v. "Select Output File" navigate to the folder with the ang file and specify the name you want the data to be saved as and click save.

vi. OpenXY Main GUI Window Settings

1. Scan type: Square
2. Material: Scan File
3. Processors: 3

c. Settings

i. Microscope Settings: double check then hit save and close

1. Accel. Volt.: 20
2. Sample tilt: 70
3. Sample Azimuthal: 0
4. Camera Elevation: 0 (will need to change)
5. Camera Azimuthal: 0
6. Screen Size (microns/pixel): 80.64 (software taken from tiff patterns)

ii. Advanced Settings: double check then hit save and close

1. Check Calculate Strain
2. Ref Image Type: “Real-Grain Ref”
3. Std Dev.: 2
4. Misorientation Tot (degrees): 5
5. “Real Ref Selection”: “IQ>Fit>CI”
6. Grain ID Method: Grain File
7. Check “Calculate Dislocation Density”
8. GND Method: Full Cross-Correlation
9. Number of points to skip 0
10. IQ cutoff 0
11. Leave Split Dislocation Density unchecked

12. Edit Ref Points: here you can manually select the reference patterns for OpenXY to use to run the Cross Correlation Analysis on. Select IQ>Fit>CI for the "Automatic Selection (for leftover grains)"

iii. Pattern Center Calibration

1. Click default and click Edit PC. Put in values from Pathfinder using equations below to convert them to OIM format.

$$PC_x = 0.5 + 0.5(^{PC_{TFx} - 15.8}/_{20}), \quad \text{(E.1)}$$

$$PC_y = 1 - (^{PC_{TFy}}/_{20}), \quad \text{(E.2)}$$

$$PC_z = (^{PC_{TFL}}/_{20}), \quad \text{(E.3)}$$

Where PF values are the values from the ThermoFisher Pathfinder software. Once corrected, close this window

iv. ROI Settings: double check simulated pattern to see if it matches Original Image.

1. ROI Size: 25
2. Number of ROIs: 48
3. ROI Style: Annular (I had an error pop up when used Grid)
4. ROI Filtering: 2, 50, 1, 1
5. Image Filter Type: standard
6. Image Filter values: 9, 90, 0, 0
7. Save and close

v. Pattern Center Calibration: have already put in PC from Pathfinder, now want to see if can refine
    1. Under “New Pattern Center” select “Strain Minimization” and click “Add New PC”.
    2. In the new “PCEdit” window, the x y z star values should be the PC values inputted previously. Make sure Plane Fit: Naïve, and Name: StrainMin then click Done.
    3. When the “Select Type” window pops up, select “Manual” for point selection. Click “IPF” in the Resize scan window.
    4. In the new window with the IPF map, select at least one point per grain. And if there are distinguishable subgrains, select one point per subgrain. Take a snip/screenshot to save the areas selected for your own notes. Then reselect the window and hit the return key to start the PC calibration.

vi. Test Geometry (under Settings)
    1. Have Test Geometry and Pattern Center Calibration windows side-by-side to check PC results.
    2. In the PC Calibration window, select “StrainMin” from the Pattern Center List.
    3. In the Test Geometry window, select several points in the scan map with your cursor. Check that the green overlay line match well with the pattern underneath. Make sure that the pattern selected is a clear and good pattern.

vii. Click “Run” in the OpenXY main window.

Appendix F

Process for selecting data from HR-EBSD analyses

Below are instructions for producing .png images that show the data to take from each HR-EBSD analysis. IPF maps produced from an OpenXY HR-EBSD analysis using MTEX are opened in GIMP (version 2.10.8). The regions to keep from each HR-EBSD analysis are blacked out by hand. The rest of the image is made transparent. Make .png images for each HR-EBSD analysis in OpenXY. To make sure the HR-EBSD analyses provide data for the entire scan area where the cross-correlation method is calculated correctly, open the IPF map from the EBSD data and overlay the png images. The png overlays should black out the entire IPF map when the HR-EBSD analyses provide good HR-EBSD data for the entire scan.

In GIMP

1. Open one of the IPF maps from an HR-EBSD analysis.
2. Right click layer and hit “Add Alpha Channel”
3. Use rope and/or paintbrush to black out areas to keep
4. Convert image to black and white: Colors -> Threshold
    a. Before thresholding, make sure you have a way to keep the image the same size. You might need to draw on the corners of the image.
5. Remove white background: Select Fuzzy tool, select the background and hit the delete button. You should have a transparent background now
6. Crop the image to only include the scan area. Image -> Crop to selection. Make sure to get rid of the white border produced by MTEX. This can be done with the fuzzy tool.
7. Scale the image: Set the scale of the image to match the number of x and y positions in the ang file. For example, for an ang file that has 256 different x positions (noted

as NCOLS in the top of the ang file) and 170 y positions (noted as NROWS in the top of the ang file), the layer should be 256 x 170 pixels.

8. Export as a png and make sure to not keep the background.

Appendix G

HR-EBSD Compiler Script

Below is the script run in Matlab R2019b with MTEX version 5.6.0 that compiles all the OpenXY HR-EBSD analyses. This script requires the ang files from all the HR-EBSD analyses along with black and transparent png images created in GIMP of the data selected from each HR-EBSD analysis. The process for producing the png images is described in Appendix F.

```
% Takes mulitple HR-EBSD datasets of same scan (where the points of
interest
% have been hand selected for each dataset)and creates a compiled ang
file
% of all the "corrected data"

%%  read in all the ang files as ebsd datasets
clear all
close all
% start up mtex
startup_mtex

% specify output file name
fName = 'N205DF_Area10_HREBSD_Compiled_OpenXY_20211005.ang';

% crystal symmetry
CS = {'notIndexed', crystalSymmetry('cubic', [3 3 3], 'mineral',
'Generic BCC', 'color', 'LightSkyBlue')};
SS=specimenSymmetry('orthorhombic');
% plotting convention
setMTEXpref('xAxisDirection','east');
setMTEXpref('zAxisDirection','outOfPlane');

% Specify File Names
pname_Hraw = 'D:\EBSD Data\N205D\N205DF\Area 10';  % path to files
fname_1 = [pname_Hraw
'\Corr_N205DF_Area10_HREBSD_OpenXY_OriginalAng_ManuallySelectedRefPatte
rns_v1_20210927.ang'];
fname_2 = [pname_Hraw
'\Corr_N205DF_Area10_HREBSD_OpenXY_OriginalAng_ManuallySelectedRefPatte
rns_v2_20210926.ang'];
fname_3 = [pname_Hraw
'\Corr_N205DF_Area10_HREBSD_OpenXY_OriginalAng_ManuallySelectedRefPatte
rns_v3_20210926.ang'];
```

```
fname_4 = [pname_Hraw
'\Corr_N205DF_Area10_HREBSD_OpenXY_OriginalAng_ManuallySelectedRefPatte
rns_v4_20210928.ang'];
fname_5 = [pname_Hraw
'\Corr_N205DF_Area10_HREBSD_OpenXY_OriginalAng_ManuallySelectedRefPatte
rns_v5_20210928.ang'];
fname_6 = [pname_Hraw
'\Corr_N205DF_Area10_HREBSD_OpenXY_OriginalAng_ManuallySelectedRefPatte
rns_v6_20210928.ang'];
fname_7 = [pname_Hraw
'\Corr_N205DF_Area10_HREBSD_OpenXY_OriginalAng_ManuallySelectedRefPatte
rns_v7_20210928.ang'];
fname_8 = [pname_Hraw
'\Corr_N205DF_Area10_HREBSD_OpenXY_OriginalAng_ManuallySelectedRefPatte
rns_v8_20211001.ang'];

% Import the Data
% create the EBSD variables containing the data
ebsd1 = EBSD.load(fname_1,CS,'interface','ang',...
  'convertSpatial2EulerReferenceFrame', 'setting 2')
ebsd2 = EBSD.load(fname_2,CS,'interface','ang',...
  'convertSpatial2EulerReferenceFrame', 'setting 2')
ebsd3 = EBSD.load(fname_3,CS,'interface','ang',...
  'convertSpatial2EulerReferenceFrame', 'setting 2')
ebsd4 = EBSD.load(fname_4,CS,'interface','ang',...
  'convertSpatial2EulerReferenceFrame', 'setting 2')
ebsd5 = EBSD.load(fname_5,CS,'interface','ang',...
  'convertSpatial2EulerReferenceFrame', 'setting 2')
ebsd6 = EBSD.load(fname_6,CS,'interface','ang',...
  'convertSpatial2EulerReferenceFrame', 'setting 2')
ebsd7 = EBSD.load(fname_7,CS,'interface','ang',...
  'convertSpatial2EulerReferenceFrame', 'setting 2')
ebsd8 = EBSD.load(fname_8,CS,'interface','ang',...
  'convertSpatial2EulerReferenceFrame', 'setting 2')

%rotate all the ebsd data
rot = rotation.byAxisAngle(zvector, 90*degree);

ebsd1 = rotate(ebsd1, rot, 'keepEuler');
ebsd2 = rotate(ebsd2, rot, 'keepEuler');
ebsd3 = rotate(ebsd3, rot, 'keepEuler');
ebsd4 = rotate(ebsd4, rot, 'keepEuler');
ebsd5 = rotate(ebsd5, rot, 'keepEuler');
ebsd6 = rotate(ebsd6, rot, 'keepEuler');
ebsd7 = rotate(ebsd7, rot, 'keepEuler');
ebsd8 = rotate(ebsd8, rot, 'keepEuler');

% %plot a few of the datasets to make sure its imported correctly
% oM=ipfHSVKey(ebsd1('Generic BCC')) %coloring for inverse pole figure
maps
%
% figure                 % printing the standard triangle to go with
the data
```

```
% plot(oM)
% print('IPF_Triangle_cubic','-dtiffn','-r0')
%
%
% % x = TLTD(RD) y = TD z = STD
% oM.inversePoleFigureDirection=xvector;
% colorx=oM.orientation2color(ebsd1('Generic BCC').orientations);
% oM.inversePoleFigureDirection=yvector;
% colory=oM.orientation2color(ebsd1('Generic BCC').orientations);
% oM.inversePoleFigureDirection=zvector;
% colorz=oM.orientation2color(ebsd1('Generic BCC').orientations);
%
% %plot IPF map wrt X/
TLTD(RD)                                        %Figure 1
% figure
% set(gcf,'renderer','zbuffer');
% [~,mP]=plot(ebsd1('Generic BCC'),colorx);
% mP.micronBar.visible='on'
% set(0,'defaultfigurepaperpositionmode','auto')
% print('IPF_TLTD_RD_N205DF_Area10_ebsd1','-dtiffn','-r0')
%
% %plot IPF map wrt X/
TLTD(RD)                                        %Figure 2
% figure
% set(gcf,'renderer','zbuffer');
% [~,mP]=plot(ebsd8('Generic BCC'),colorx);
% mP.micronBar.visible='on'
% set(0,'defaultfigurepaperpositionmode','auto')
% print('IPF_TLTD_RD_N205DF_Area10_ebsd8','-dtiffn','-r0')


%% read in the png files from GIMP that are edited (these are black and
white
% images with a transparent background
path2PNG = 'D:\EBSD Data\N205D\N205DF\Area 10\MTEX Results after
OpenXY';
[image1, map, alphachannel] = imread([path2PNG '\Ref
V1\IPF_TD_N205DF_Area10_OpenXYCorrected_v1_unfilled_GIMP.png']);
[image2, map2, alphachannel2] = imread([path2PNG '\Ref
V2\IPF_TD_N205DF_Area10_OpenXYCorrected_v2_unfilled_GIMP.png']);
[image3, map3, alphachannel3] = imread([path2PNG '\Ref
V3\IPF_TD_N205DF_Area10_OpenXYCorrected_v3_unfilled_GIMP.png']);
[image4, map4, alphachannel4] = imread([path2PNG '\Ref
V4\IPF_TD_N205DF_Area10_OpenXYCorrected_v4_unfilled_GIMP.png']);
[image5, map5, alphachannel5] = imread([path2PNG '\Ref
V5\IPF_TD_N205DF_Area10_OpenXYCorrected_v5_unfilled_GIMP.png']);
[image6, map6, alphachannel6] = imread([path2PNG '\Ref
V6\IPF_TD_N205DF_Area10_OpenXYCorrected_v6_unfilled_GIMP.png']);
[image7, map7, alphachannel7] = imread([path2PNG '\Ref
V7\IPF_TD_N205DF_Area10_OpenXYCorrected_v7_unfilled_GIMP.png']);
[image8, map8, alphachannel8] = imread([path2PNG '\Ref
V8\IPF_TD_N205DF_Area10_OpenXYCorrected_v8_unfilled_GIMP.png']);
```

```
%reading in one of the corrected IPF maps
image1Og = imread([path2PNG '\Ref
V1\IPF_TD_N205DF_Area10_OpenXYCorrected_v1_unfilled.tif']);

%convert the black and white image matrices to 0 and 1's
image1B = imbinarize(image1);
image2B = imbinarize(image2);
image3B = imbinarize(image3);
image4B = imbinarize(image4);
image5B = imbinarize(image5);
image6B = imbinarize(image6);
image7B = imbinarize(image7);
image8B = imbinarize(image8);

figure
imshow(image1)

%create 2d matrices from the images
mat1 = ~image1B(:,:,1);
mat2 = ~image2B(:,:,1).*2;
mat3 = ~image3B(:,:,1).*3;
mat4 = ~image4B(:,:,1).*4;
mat5 = ~image5B(:,:,1).*5;
mat6 = ~image6B(:,:,1).*6;
mat7 = ~image7B(:,:,1).*7;
mat8 = ~image8B(:,:,1).*8;

%% find out which points I want to take from each image

mat2Pop = zeros(size(mat1)); %matrix that I will populate with values

% Just do 1 > 2 > 3 > 4 > 5 > 6 > 7 > 8
for i = 1:size(mat1,1) %rows
    for j = 1:size(mat1,2) %columns
        if mat1(i,j) == 1
            mat2Pop(i,j) = 1;
        elseif mat2(i,j) == 2
            mat2Pop(i,j) = 2;
        elseif mat3(i,j) == 3
            mat2Pop(i,j) = 3;
        elseif mat4(i,j) == 4
            mat2Pop(i,j) = 4;
        elseif mat5(i,j) == 5
            mat2Pop(i,j) = 5;
        elseif mat6(i,j) == 6
            mat2Pop(i,j) = 6;
        elseif mat7(i,j) == 7
            mat2Pop(i,j) = 7;
        elseif mat8(i,j) == 8
            mat2Pop(i,j) = 8;
        else
            mat2Pop(i,j) = 0;
        end
```

```
    end
end
%make sure there are no overlapping points & no large gaps

imageMat2Pop = imbinarize(mat2Pop);
figure
imshow(mat2Pop) % in this plot, white means there is data there and
black means no data

%convert matrix to a single array where x increases then y increases

array2Pop = [];
for i = 1:size(mat2Pop,1) %rows
    row = transpose(mat2Pop(i,:));
    array2Pop = [array2Pop; row];
end


%% correlate numbers in matrix to ang file rows to pull
% will create a matrix for each ebsd data set and be ready to
% pull from each row

% ebsd1
phi11 = round(ebsd1.rotations.phi1, 6);
Phi1 = round(ebsd1.rotations.Phi, 6);
phi21 = round(ebsd1.rotations.phi2, 6);
x1 = round(ebsd1.prop.x, 6);
y1 = -round(ebsd1.prop.y, 6);
IQ1 = ebsd1.prop.iq;
CI1 = ebsd1.prop.ci;
phase1 = ebsd1.phase;
SEM1 = ebsd1.prop.sem_signal;
Fit1 = ebsd1.prop.fit;

varNames1 = {'phi11', 'Phi1', 'phi21', 'x1', 'y1', 'IQ1', 'CI1',
'phase1', 'SEM1', 'Fit1'};
A1 = table(phi11, Phi1, phi21, x1, y1, IQ1, CI1, phase1, SEM1, Fit1,
'VariableNames', varNames1);
A1 = sortrows(A1, {'y1', 'x1'});

%ebsd2
phi12 = round(ebsd2.rotations.phi1, 6);
Phi2 = round(ebsd2.rotations.Phi, 6);
phi22 = round(ebsd2.rotations.phi2, 6);
x2 = round(ebsd2.prop.x, 6);
y2 = -round(ebsd2.prop.y, 6);
IQ2 = ebsd2.prop.iq;
CI2 = ebsd2.prop.ci;
phase2 = ebsd2.phase;
SEM2 = ebsd2.prop.sem_signal;
Fit2 = ebsd2.prop.fit;
```

```
varNames2 = {'phi12', 'Phi2', 'phi22', 'x2', 'y2', 'IQ2', 'CI2',
'phase2', 'SEM2', 'Fit2'};
A2 = table(phi12, Phi2, phi22, x2, y2, IQ2, CI2, phase2, SEM2, Fit2,
'VariableNames', varNames2);
A2 = sortrows(A2, {'y2', 'x2'});

%ebsd3
phi13 = round(ebsd3.rotations.phi1, 6);
Phi3 = round(ebsd3.rotations.Phi, 6);
phi23 = round(ebsd3.rotations.phi2, 6);
x3 = round(ebsd3.prop.x, 6);
y3 = -round(ebsd3.prop.y, 6);
IQ3 = ebsd3.prop.iq;
CI3 = ebsd3.prop.ci;
phase3 = ebsd3.phase;
SEM3 = ebsd3.prop.sem_signal;
Fit3 = ebsd3.prop.fit;

varNames3 = {'phi13', 'Phi3', 'phi23', 'x3', 'y3', 'IQ3', 'CI3',
'phase3', 'SEM3', 'Fit3'};
A3 = table(phi13, Phi3, phi23, x3, y3, IQ3, CI3, phase3, SEM3, Fit3,
'VariableNames', varNames3);
A3 = sortrows(A3, {'y3', 'x3'});

%ebsd4
phi14 = round(ebsd4.rotations.phi1, 6);
Phi4 = round(ebsd4.rotations.Phi, 6);
phi24 = round(ebsd4.rotations.phi2, 6);
x4 = round(ebsd4.prop.x, 6);
y4 = -round(ebsd4.prop.y, 6);
IQ4 = ebsd4.prop.iq;
CI4 = ebsd4.prop.ci;
phase4 = ebsd4.phase;
SEM4 = ebsd4.prop.sem_signal;
Fit4 = ebsd4.prop.fit;

varNames4 = {'phi14', 'Phi4', 'phi24', 'x4', 'y4', 'IQ4', 'CI4',
'phase4', 'SEM4', 'Fit4'};
A4 = table(phi14, Phi4, phi24, x4, y4, IQ4, CI4, phase4, SEM4, Fit4,
'VariableNames', varNames4);
A4 = sortrows(A4, {'y4', 'x4'});

%ebsd5
phi15 = round(ebsd5.rotations.phi1, 6);
Phi5 = round(ebsd5.rotations.Phi, 6);
phi25 = round(ebsd5.rotations.phi2, 6);
x5 = round(ebsd5.prop.x, 6);
y5 = -round(ebsd5.prop.y, 6);
IQ5 = ebsd5.prop.iq;
CI5 = ebsd5.prop.ci;
phase5 = ebsd5.phase;
SEM5 = ebsd5.prop.sem_signal;
Fit5 = ebsd5.prop.fit;
```

```
varNames5 = {'phi15', 'Phi5', 'phi25', 'x5', 'y5', 'IQ5', 'CI5',
'phase5', 'SEM5', 'Fit5'};
A5 = table(phi15, Phi5, phi25, x5, y5, IQ5, CI5, phase5, SEM5, Fit5,
'VariableNames', varNames5);
A5 = sortrows(A5, {'y5', 'x5'});

%ebsd6
phi16 = round(ebsd6.rotations.phi1, 6);
Phi6 = round(ebsd6.rotations.Phi, 6);
phi26 = round(ebsd6.rotations.phi2, 6);
x6 = round(ebsd6.prop.x, 6);
y6 = -round(ebsd6.prop.y, 6);
IQ6 = ebsd6.prop.iq;
CI6 = ebsd6.prop.ci;
phase6 = ebsd6.phase;
SEM6 = ebsd6.prop.sem_signal;
Fit6 = ebsd6.prop.fit;

varNames6 = {'phi16', 'Phi6', 'phi26', 'x6', 'y6', 'IQ6', 'CI6',
'phase6', 'SEM6', 'Fit6'};
A6 = table(phi16, Phi6, phi26, x6, y6, IQ6, CI6, phase6, SEM6, Fit6,
'VariableNames', varNames6);
A6 = sortrows(A6, {'y6', 'x6'});

%ebsd7
phi17 = round(ebsd7.rotations.phi1, 6);
Phi7 = round(ebsd7.rotations.Phi, 6);
phi27 = round(ebsd7.rotations.phi2, 6);
x7 = round(ebsd7.prop.x, 6);
y7 = -round(ebsd7.prop.y, 6);
IQ7 = ebsd7.prop.iq;
CI7 = ebsd7.prop.ci;
phase7 = ebsd7.phase;
SEM7 = ebsd7.prop.sem_signal;
Fit7 = ebsd7.prop.fit;

varNames7 = {'phi17', 'Phi7', 'phi27', 'x7', 'y7', 'IQ7', 'CI7',
'phase7', 'SEM7', 'Fit7'};
A7 = table(phi17, Phi7, phi27, x7, y7, IQ7, CI7, phase7, SEM7, Fit7,
'VariableNames', varNames7);
A7 = sortrows(A7, {'y7', 'x7'});

%ebsd8
phi18 = round(ebsd8.rotations.phi1, 6);
Phi8 = round(ebsd8.rotations.Phi, 6);
phi28 = round(ebsd8.rotations.phi2, 6);
x8 = round(ebsd8.prop.x, 6);
y8 = -round(ebsd8.prop.y, 6);
IQ8 = ebsd8.prop.iq;
CI8 = ebsd8.prop.ci;
phase8 = ebsd8.phase;
SEM8 = ebsd8.prop.sem_signal;
```

```
Fit8 = ebsd8.prop.fit;

varNames8 = {'phi18', 'Phi8', 'phi28', 'x8', 'y8', 'IQ8', 'CI8',
'phase8', 'SEM8', 'Fit8'};
A8 = table(phi18, Phi8, phi28, x8, y8, IQ8, CI8, phase8, SEM8, Fit8,
'VariableNames', varNames8);
A8 = sortrows(A8, {'y8', 'x8'});

%%  create table of values from ebsd data files -> will use to export
to new ang file

compiledTable = zeros(size(array2Pop,1), 10);
for i = 1:size(array2Pop, 1)
%for i = 1:10
    if array2Pop(i) == 1
        row = A1(i,:);
    elseif array2Pop(i) == 2
        row = A2(i,:);
    elseif array2Pop(i) == 3
        row = A3(i,:);
    elseif array2Pop(i) == 4
        row = A4(i,:);
    elseif array2Pop(i) == 5
        row = A5(i,:);
    elseif array2Pop(i) == 6
        row = A6(i,:);
    elseif array2Pop(i) == 7
        row = A7(i,:);
    elseif array2Pop(i) == 8
        row = A8(i,:);
    else
        % fill with A1 matrix but set ci to 0 so it can be removed
later
        row = A1(i,:);
        row{1,7} = 0;
    end
    row = table2array(row);
    compiledTable(i,1) = row(1,1);
    compiledTable(i,2) = row(1,2);
    compiledTable(i,3) = row(1,3);
    compiledTable(i,4) = row(1,4);
    compiledTable(i,5) = row(1,5);
    compiledTable(i,6) = row(1,6);
    compiledTable(i,7) = row(1,7);
    compiledTable(i,8) = row(1,8);
    compiledTable(i,9) = row(1,9);
    compiledTable(i,10) = row(1,10);
end

%export new ang file
filePh = fopen(fName,'w'); %Open new txt file for writing
roundOff = 3; %Rounding coordinates to 'roundOff' digits
```

```
fprintf(filePh,'# %-22s%.6f\n','TEM_PIXperUM',1);
fprintf(filePh,'# %-22s%.6f\n','x-star',0);
fprintf(filePh,'# %-22s%.6f\n','y-star',0);
fprintf(filePh,'# %-22s%.6f\n','z-star',0);
fprintf(filePh,'# %-22s%.6f\n','WorkingDistance',0);
fprintf(filePh,'#\n');

% Write phase info
for phaseId = fliplr(ebsd1.indexedPhasesId)
  cs = ebsd1.CSList{phaseId};
  fprintf(filePh,'# %s %.0f\n','Phase',ebsd1.phaseMap(phaseId));
  fprintf(filePh,'# %s  \t%s\n','MaterialName',cs.mineral);
  fprintf(filePh,'# %s     \t%s\n','Formula','');
  fprintf(filePh,'# %s \t\t%s\n','Info','');
  fprintf(filePh,'# %-22s%s\n','Symmetry',cs.pointGroup);
  fprintf(filePh,'# %-22s %4.3f %5.3f %5.3f %7.3f %7.3f %7.3f\n',...
    'LatticeConstants',cs.aAxis.abs,cs.bAxis.abs,cs.cAxis.abs,...
    cs.alpha/degree,cs.beta/degree,cs.gamma/degree);
  fprintf(filePh,'# %-22s%.0f\n','NumberFamilies',0);
  for jj = 1:6
    fprintf(filePh,'# %s \t%.f %.f %.f %.f %.6f %.f\n',...
      'hklFamilies',0,0,0,0,0,0);
  end
end

% Write map info
if length(ebsd1.unitCell)==6 %hex Grid
  fprintf(filePh,'# %s: %s\n','GRID','HexGrid');
else
  fprintf(filePh,'# %s: %s\n','GRID','SqrGrid');
end

% get gridified version of ebsd map
ebsdGrid = ebsd1.gridify;
fprintf(filePh,'# %s: %.6f\n','XSTEP',round(ebsdGrid.dx,roundOff));
fprintf(filePh,'# %s: %.6f\n','YSTEP',round(ebsdGrid.dy,roundOff));
if length(ebsd1.unitCell)==6 %hex Grid
  fprintf(filePh,'# %s: %.0f\n','NCOLS_ODD',ebsdGrid.size(2)-1);
  fprintf(filePh,'# %s: %.0f\n','NCOLS_EVEN',ebsdGrid.size(2)-2);
else
  fprintf(filePh,'# %s: %.0f\n','NCOLS_ODD',ebsdGrid.size(2));
  fprintf(filePh,'# %s: %.0f\n','NCOLS_EVEN',ebsdGrid.size(2));
end
fprintf(filePh,'# %s: %.0f\n','NROWS',ebsdGrid.size(1));
fprintf(filePh,'#\n');
fprintf(filePh,'# %s: \t%s\n','OPERATOR','Administrator');
fprintf(filePh,'#\n');
fprintf(filePh,'# %s: \t%s\n','SAMPLEID','');
fprintf(filePh,'#\n');
fprintf(filePh,'# %s: \t%s\n','SCANID','');
fprintf(filePh,'#\n');
```

```
fprintf(filePh,'%9.6f %9.6f %9.6f %12.6f %12.6f %6.1f %6.3f %2.0f %6.0f
%6.3f\n',compiledTable.');

fclose(filePh);
```

Appendix H

MTEX Analysis Script

Below is the script run in Matlab R2019b using MTEX version 5.6.0 that produces all the graphical visualization for the OpenXY HR-EBSD result, which includes the subgrain boundary segmentation. This script can be altered to produce standard EBSD texture plots. It also produces the edges List and phase List which are required for the Grain File Script in Appendix B.

```
%%
clear all
close all
% start up mtex
startup_mtex

%% Specify Crystal and Specimen Symmetries

% crystal symmetry
CS = {'notIndexed', crystalSymmetry('cubic', [3 3 3], 'mineral',
'Generic BCC', 'color', 'LightSkyBlue')};
SS=specimenSymmetry('orthorhombic');
% plotting convention
setMTEXpref('xAxisDirection','east');
setMTEXpref('zAxisDirection','outOfPlane');

%% Specify File Names
pname_Hraw = 'D:\EBSD Data\N205D\N205DF\Area 10';  % path to files
fname_Hraw = [pname_Hraw
'\N205DF_Area10_HREBSD_Compiled_OpenXY_20211005.ang']; % files to be
imported

%% Import the Data

% create an EBSD variable containing the data
ebsd_Hraw = EBSD.load(fname_Hraw,CS,'interface','ang',...
  'convertSpatial2EulerReferenceFrame', 'setting 2')

% found it wasn't plotting correctly, so I need to rotate the data
rot = rotation.byAxisAngle(zvector, 90*degree);
ebsd_Hraw = rotate(ebsd_Hraw, rot, 'keepEuler');

%getting rid of 'missing data points' that got filled in with the
%exportEERdataset
ebsd_Hraw = ebsd_Hraw(ebsd_Hraw.prop.ci>0)
```

```
%% Plot Inverse Pole Figure Maps
oM=ipfHSVKey(ebsd_Hraw('Generic BCC')) %coloring for inverse pole
figure maps

figure                  % printing the standard triangle to go with the
data
plot(oM)
print('IPF_Triangle_cubic','-dtiffn','-r0')


% x = TD  y = TLTD(RD) z = STD
oM.inversePoleFigureDirection=xvector;
colorx=oM.orientation2color(ebsd_Hraw('Generic BCC').orientations);
oM.inversePoleFigureDirection=yvector;
colory=oM.orientation2color(ebsd_Hraw('Generic BCC').orientations);
oM.inversePoleFigureDirection=zvector;
colorz=oM.orientation2color(ebsd_Hraw('Generic BCC').orientations);

%plot IPF map wrt X/
TD                                          %Figure 1
figure
set(gcf,'renderer','zbuffer');
[~,mP]=plot(ebsd_Hraw('Generic BCC'),colorx);
mP.micronBar.visible='on'
set(0,'defaultfigurepaperpositionmode','auto')
print('IPF_TD_N205DF_Area10_Compiled_OpenXY','-dtiffn','-r0')

%plot IPF map wrt Y/ TLTD
RD                                         %Figure 2
figure
set(gcf,'renderer','zbuffer');
[~,mP]=plot(ebsd_Hraw('Generic BCC'),colory);
mP.micronBar.visible='on'
set(0,'defaultfigurepaperpositionmode','auto')
print('IPF_TLTD_RD_N205DF_Area10_Compiled_OpenXY','-dtiffn','-r0')

%plot IPF map wrt Z/
STD                                         %Figure 3
figure
set(gcf,'renderer','zbuffer');
[~,mP]=plot(ebsd_Hraw('Generic BCC'),colorz);
mP.micronBar.visible='on'
set(0,'defaultfigurepaperpositionmode','auto')
print('IPF_STD_N205DF_Area10_Compiled_OpenXY','-dtiffn','-r0')

%% Reconstruct the grains
%rename ebsd data set
ebsdG=ebsd_Hraw
mis_ang=5*degree;
% detect grains
[grains, ebsdG.grainId,
ebsdG.mis2mean]=calcGrains(ebsdG,'angle',mis_ang)
% number of grains
```

```
number_of_calcGrains=grains.length

% commented out when you want the number of pixels to match number of
kikuchi
% patterns -> necessary for producing the Grain File

% remove grains containing less than a critical number of indexed
points
min_g_size = 8;
selected_grains=grains(grains.grainSize>min_g_size);
removed_grains=grains(grains.grainSize<min_g_size);
ebsdG(removed_grains)=[]

% number of small grains removed from all phase
number_of_small_grains_removed=number_of_calcGrains-
selected_grains.length
[grains,ebsdG.grainId]=calcGrains(ebsdG,'angle',mis_ang);
SS=specimenSymmetry('orthorhombic');

%end of commented out region

% Plot Inverse Pole Figure Maps
% IPF X
%oM=ipdfOrientationMap                                          %Figu
re 4
figure
plot(ebsdG)
hold on
plot(grains.boundary,'linewidth',2)
hold off


%% Clean up the EBSD data (lots of misindexed points coming up as
individual grains)
ebsd_Hraw1 = ebsd_Hraw;
ebsd_Hraw = fill(ebsdG, grains);
mis_ang=5*degree;
% detect grains
[grains_Hraw, ebsd_Hraw.grainId,
ebsd_Hraw.mis2mean]=calcGrains(ebsd_Hraw,'angle',mis_ang)
% number of grains
number_of_calcGrains= grains_Hraw.length

% remove grains containing less than a critical number of indexed
points
min_g_size = 8;
selected_grains=grains_Hraw(grains_Hraw.grainSize>min_g_size);
removed_grains=grains_Hraw(grains_Hraw.grainSize<min_g_size);
ebsd_Hraw(removed_grains)=[]

% number of small grains removed from all phase
number_of_small_grains_removed=number_of_calcGrains-
selected_grains.length
```

```
[grains_Hraw,ebsd_Hraw.grainId]=calcGrains(ebsd_Hraw,'angle',mis_ang);
SS=specimenSymmetry('orthorhombic');

% detecting subgrains
ebsd_subgrains = ebsd_Hraw1;
mis_angSub=0.2*degree;
[subgrains, ebsd_subgrains.grainId,
ebsd_subgrains.mis2mean]=calcGrains(ebsd_subgrains,'angle',mis_angSub)
% number of grains
number_of_calcSubgrains= subgrains.length

% remove subgrains containing less than a critical number of indexed
points
min_subg_size = 8;
selected_subgrains=subgrains(subgrains.grainSize>min_subg_size);
removed_subgrains=subgrains(subgrains.grainSize<min_subg_size);
ebsd_subgrains(removed_subgrains)=[]

% number of small grains removed from all phase
number_of_small_subgrains_removed=number_of_calcSubgrains-
selected_subgrains.length
[subgrains,ebsd_subgrains.grainId]=calcGrains(ebsd_subgrains,'angle',mi
s_angSub);
SS=specimenSymmetry('orthorhombic');

% redefining colors after the fill
oM.inversePoleFigureDirection=xvector;
colorx=oM.orientation2color(ebsd_Hraw('Generic BCC').orientations);
oM.inversePoleFigureDirection=yvector;
colory=oM.orientation2color(ebsd_Hraw('Generic BCC').orientations);
oM.inversePoleFigureDirection=zvector;
colorz=oM.orientation2color(ebsd_Hraw('Generic BCC').orientations);

%plot of grains and subgrain boundaries only
figure                                                          %Figu
re
plot(subgrains.boundary,'linecolor','blue','linewidth',2)
hold on
plot(grains.boundary,'linecolor','black','linewidth',2 )
hold off
mP.micronBar.visible='on'
set(0,'defaultfigurepaperpositionmode','auto')
print('SubgrainandGrainBoundarySkeleton_N205DF_Area10_Compiled_OpenXY_0
_2deg','-dtiffn','-r0')

%plot of grains and subgrain boundaries with IPF
figure                                                          %Figu
re
set(gcf,'renderer','zbuffer');
[~,mP]=plot(ebsd_Hraw('Generic BCC'),colory);
hold on
plot(subgrains.boundary,'linecolor','blue','linewidth',2)
plot(grains.boundary,'linecolor','black','linewidth',2 )
```

```
hold off
mP.micronBar.visible='on'
set(0,'defaultfigurepaperpositionmode','auto')
print('SubgrainandGrainBoundaryIPF_N205DF_Area10_Compiled_OpenXY_0_2deg
','-dtiffn','-r0')

%plot IPF map wrt X/
TD                                          %Figure 1
figure
set(gcf,'renderer','zbuffer');
[~,mP]=plot(ebsd_Hraw('Generic BCC'),colorx);
mP.micronBar.visible='on'
set(0,'defaultfigurepaperpositionmode','auto')
print('IPF_TD_N205DF_Area10_Compiled_OpenXY','-dtiffn','-r0')

%plot IPF map wrt Y/ TLTD
RD                                         %Figure 2
figure
set(gcf,'renderer','zbuffer');
[~,mP]=plot(ebsd_Hraw('Generic BCC'),colory);
mP.micronBar.visible='on'
set(0,'defaultfigurepaperpositionmode','auto')
print('IPF_TLTD_RD_N205DF_Area10_Compiled_OpenXY','-dtiffn','-r0')

%plot IPF map wrt Z/
STD                                         %Figure 3
figure
set(gcf,'renderer','zbuffer');
[~,mP]=plot(ebsd_Hraw('Generic BCC'),colorz);
mP.micronBar.visible='on'
set(0,'defaultfigurepaperpositionmode','auto')
print('IPF_STD_N205DF_Area10_Compiled_OpenXY','-dtiffn','-r0')

% x = TD  y = TLTD(RD) z = STD

figure                                  %plot IPF map wrt X/ TD
Figure 5
set(gcf,'renderer','zbuffer');
[~,mP]=plot(ebsd_Hraw('Generic BCC'),colorx);
hold on
plot(grains.boundary,'linewidth',2)
hold off
mP.micronBar.visible='on'
set(0,'defaultfigurepaperpositionmode','auto')
print('IPFgb_TD_N205DF_Area10_Compiled_OpenXY','-dtiffn','-r0')

figure                                   %plot IPF map wrt Y/ TLTD RD
Figure 6
set(gcf,'renderer','zbuffer');
[~,mP]=plot(ebsd_Hraw('Generic BCC'),colory);
hold on
plot(grains.boundary,'linewidth',2)
hold off
```

```
mP.micronBar.visible='on'
set(0,'defaultfigurepaperpositionmode','auto')
print('IPFgb_TLTD_RD_N205DF_Area10_Compiled_OpenXY','-dtiffn','-r0')

figure                                  %plot IPF map wrt Z/ STD
Figure 7
set(gcf,'renderer','zbuffer');
[~,mP]=plot(ebsd_Hraw('Generic BCC'),colorz);
hold on
plot(grains.boundary,'linewidth',2)
hold off
mP.micronBar.visible='on'
set(0,'defaultfigurepaperpositionmode','auto')
print('IPFgb_STD_N205DF_Area10_Compiled_OpenXY','-dtiffn','-r0')

% plot mean orientations
oM.inversePoleFigureDirection=zvector;
colorzM=oM.orientation2color(grains('Generic BCC').meanOrientation);

figure                                                              %Figu
re 8
plot(grains('Generic BCC'), colorzM)
hold on
plot(grains.boundary,'linewidth',2)
hold off
set(0,'defaultfigurepaperpositionmode','auto')
print('MeanOrientation_N205DF_Area10_Compiled_OpenXY','-dtiffn','-r0')

%% Remove subgrain boundary grains
% duplicate the subgrains object
% subgrains will be the unmodified object of the reconstructed EBSD
data set
% subgrainNB will be the modified oject to remove all boundary grains

subgrainsNB=subgrains %NB=nonboundary
subouterBoundary_id = any(subgrainsNB.boundary.grainId==0,2); % ids of
the outer boundary segment

figure                                                              %Figu
re 9
plot(subgrainsNB)
hold on
plot(subgrainsNB.boundary(subouterBoundary_id),'linecolor','red','linew
idth',2)
hold off

% Now grains.boundary(outerBoundary_id).grainId is a list of grain ids
where
% the first column is zero, indicating the outer boundary, and the
second
% column contains the id of the boundary grain. Hence, it remains to
remove
% all grains with these ids.
```

```
% next we compute the corresponding grain_id
subgrain_id = subgrainsNB.boundary(subouterBoundary_id).grainId;
subgrain_id(subgrain_id==0) = [];       % remove all zeros

figure                          % and plot the boundary grains
Figure 10
plot(subgrainsNB(subgrain_id))
set(0,'defaultfigurepaperpositionmode','auto')
print('BoundarySubgrains_N205DF_Area10_Compiled_OpenXY','-dtiffn','-
r0')

subgrainsNB(subgrain_id) = [];  %removing the boundary grains

% grainsNB -> non-boundary grains
% get grain area
% -> get grain lineal intercept from area
figure                                                          %Figur
e 11
plot(subgrainsNB)
set(0,'defaultfigurepaperpositionmode','auto')
print('NonBoundarySubgrains_N205DF_Area10_Compiled_OpenXY','-dtiffn','-
r0')

subareaNB = area(subgrainsNB);  % grain area for non-boundary grains
subavgArea = mean(subareaNB);
sublinInterNB = sqrt((pi/4)*subareaNB); %ASTM (with error)

submatOut = [transpose(subgrainsNB.id); transpose(subareaNB);
transpose(sublinInterNB)];
submatOutT = transpose(submatOut);
numNBsubgrains = length(subgrainsNB.id);

%write these values to an output file
fileID =
fopen('N205DF_Area10_Compiled_OpenXY_SubgrainAreaNB_LinealIntercept.txt
', 'w');
fprintf(fileID, 'Total number of subgrains: ')
fprintf(fileID, '%s\r\n', num2str(subgrains.length));
fprintf(fileID, 'Number of non-boundary grains: ')
fprintf(fileID, '%s\r\n', num2str(numNBsubgrains));
fprintf(fileID, 'Average grain area (um^2): ')
fprintf(fileID, '%s\r\n', num2str(subavgArea));
fprintf(fileID, 'SubgrainID; Area; LinealInterceptNB \n');
dlmwrite('N205DF_Area10_Compiled_OpenXY_SubgrainAreaNB_LinealIntercept.
txt', submatOutT, '-append');
fclose(fileID);



%% Remove boundary grains
% duplicate the grains object
```

```
% grains will be the unmodified object of the reconstructed EBSD data
set
% grainNB will be the modified oject to remove all boundary grains

grainsNB=grains %NB=nonboundary
outerBoundary_id = any(grainsNB.boundary.grainId==0,2); % ids of the
outer boundary segment

figure                                                          %Figu
re 9
plot(grainsNB)
hold on
plot(grainsNB.boundary(outerBoundary_id),'linecolor','red','linewidth',
2)
hold off

% Now grains.boundary(outerBoundary_id).grainId is a list of grain ids
where
% the first column is zero, indicating the outer boundary, and the
second
% column contains the id of the boundary grain. Hence, it remains to
remove
% all grains with these ids.
% next we compute the corresponding grain_id
grain_id = grainsNB.boundary(outerBoundary_id).grainId;
grain_id(grain_id==0) = [];       % remove all zeros

figure                          % and plot the boundary grains
Figure 10
plot(grainsNB(grain_id))
set(0,'defaultfigurepaperpositionmode','auto')
print('BoundaryGrains_N205DF_Area10_Compiled_OpenXY','-dtiffn','-r0')

grainsNB(grain_id) = [];  %removing the boundary grains

% grainsNB -> non-boundary grains
% get grain area
% -> get grain lineal intercept from area
figure                                                          %Figur
e 11
plot(grainsNB)
set(0,'defaultfigurepaperpositionmode','auto')
print('NonBoundaryGrains_N205DF_Area10_Compiled_OpenXY','-dtiffn','-
r0')

areaNB = area(grainsNB);  % grain area for non-boundary grains
avgArea = mean(areaNB);
linInterNB = sqrt((pi/4)*areaNB); %ASTM (with error)

matOut = [transpose(grainsNB.id); transpose(areaNB);
transpose(linInterNB)];
matOutT = transpose(matOut);
numNBgrains = length(grainsNB.id);
```

```
%write these values to an output file
fileID =
fopen('N205DF_Area10_Compiled_OpenXY_GrainAreaNB_LinealIntercept.txt',
'w');
fprintf(fileID, 'Total number of grains: ')
fprintf(fileID, '%s\r\n', num2str(grains.length));
fprintf(fileID, 'Number of non-boundary grains: ')
fprintf(fileID, '%s\r\n', num2str(numNBgrains));
fprintf(fileID, 'Average grain area (um^2): ')
fprintf(fileID, '%s\r\n', num2str(avgArea));
fprintf(fileID, 'GrainID; Area; LinealInterceptNB \n');
dlmwrite('N205DF_Area10_Compiled_OpenXY_GrainAreaNB_LinealIntercept.txt
', matOutT, '-append');
fclose(fileID);

% %Export data with new grains (i.e. got rid of grains less than 5 pts)
% disp('Starting EBSD grain data export')
%
export_ang(ebsdG,'N205DF_Area10_Compiled_OpenXY_HREBSD_OpenXY_ebsdG_202
10817.ang')

% % Uncomment out this section in order to produce the Grain File for
OpenXY HR-EBSD analysis
% %% Create grain txt file for OpenXY
% % create list for edge grains and list of phases
% i = 1;
% edgesList = [];
% phaseList = [];
% for i = 1:(length(ebsdG.id))
%     % grainsNB -> non-boundary grains
%     if ismember(ebsdG.grainId(i),grainsNB.id)
%         edgesList = [edgesList; 0];
%     else
%         edgesList = [edgesList; 1];
%     end
%     if ebsdG.phaseId(i) == 2
%         phaseList = [phaseList; string('Niobium')];
%     else
%         phaseList = [phaseList; string('NotIndexed')];
%     end
%     i = i + 1;
% end
%
% disp('Starting grain file export')
%
export_GrainFile(ebsdG,'N205DF_Area10_Compiled_OpenXY_HREBSD_OpenXY_Gra
inFile20210817.txt', edgesList, phaseList)
%
% % End of section to comment out

%% Grain Orientation Try 5
%% {111}<110>
```

```
grainsNB_nb=grainsNB('Generic BCC');
SS='triclinic';
CS = ebsdG('Generic BCC').CS;
ori_111_110 = orientation.byMiller([1 1 1], [1 1 0], CS, SS);
grains_selected = findByOrientation(grainsNB_nb, ori_111_110,
15*degree);


% x = TD  y = TLTD(RD) z = STD

%plot raw ebsd data wrt xvector + outlining grains with {111}<110>
%orientation
figure                                                          %Figur
e 12
set(gcf,'renderer','zbuffer');
[~,mP]=plot(ebsd_Hraw('Generic BCC'),colorx);
hold on
plot(grains.boundary,'linewidth',2)
plot(grains_selected.boundary,'linecolor','w','linewidth',1.5)
hold off
mP.micronBar.visible='on';
set(0,'defaultfigurepaperpositionmode','auto')
print('IPFgb_TD_GrainsSelected_111_110_N205DF_Area10_Compiled_OpenXY','
-dtiffn','-r0')

%plot raw ebsd data wrt zvector + outlining grains with {111}<110>
%orientation
figure                                                          %Figur
e 13
set(gcf,'renderer','zbuffer');
[~,mP]=plot(ebsd_Hraw('Generic BCC'),colorz);
hold on
plot(grains.boundary,'linewidth',2)
plot(grains_selected.boundary,'linecolor','w','linewidth',1.5)
hold off
mP.micronBar.visible='on';
set(0,'defaultfigurepaperpositionmode','auto')
print('IPFgb_STD_GrainsSelected_111_110_N205DF_Area10_Compiled_OpenXY',
'-dtiffn','-r0')

% Plotting histogram of grain sizes for grains with orientation
{111}<110>
d_111_110=grains_selected.diameter();
%N = histcounts(d_111_110, edges);
%centers = (edges(1:end-1) + edges(2:end))/2;
%bar(centers, N)
bound=130;
nbins=10;
edges = linspace(0,bound,nbins);
hist_c = histcounts(d_111_110,edges);
figure                                                          %Figur
e 14
bar(edges(1:nbins-1),hist_c);
```

```
xlabel('grain size, um') % x-axis label
ylabel('number of grains') % y-axis label
set(0,'defaultfigurepaperpositionmode','auto')
print('111_110_BarPlot_N205DF_Area10_Compiled_OpenXY','-dtiffn','-r0')

%% Growth Selection Try 4

% limit grain boundaries to those between Nb grains
gB_Nb=grains.boundary('Generic BCC','Generic BCC');

%$%$%%$%$%$%
% This code produces the same results as Nick's Code
gB3=gB_Nb(angle(gB_Nb.misorientation,CSL(3,ebsd_Hraw('Generic
BCC').CS))<8.67*degree);
gB5=gB_Nb(angle(gB_Nb.misorientation,CSL(5,ebsd_Hraw('Generic
BCC').CS))<6.71*degree);
gB7=gB_Nb(angle(gB_Nb.misorientation,CSL(7,ebsd_Hraw('Generic
BCC').CS))<5.67*degree);
gB9=gB_Nb(angle(gB_Nb.misorientation,CSL(9,ebsd_Hraw('Generic
BCC').CS))<5.01*degree);
gB11=gB_Nb(angle(gB_Nb.misorientation,CSL(11,ebsd_Hraw('Generic
BCC').CS))<4.53*degree);
%gB19=gB_Fe(angle(gB_Fe.misorientation,CSL(19,ebsd_Hraw('Fe').CS))<3.45
*degree);
% overlay CSL grain boundaries with the existing plot
plot(gB_Nb)                                                    %Figur
e 15
hold on
plot(gB3,'lineColor','r','linewidth',2','DisplayName','CSL 3')
hold on
plot(gB5,'lineColor',[0.9100    0.4100
0.1700],'linewidth',2','DisplayName','CSL 5')
hold on
plot(gB7,'lineColor','y','linewidth',2','DisplayName','CSL 7')
hold on
plot(gB9,'lineColor','g','linewidth',2','DisplayName','CSL 9')
hold on
plot(gB11,'lineColor','b','linewidth',2','DisplayName','CSL 11')
hold on
%plot(gB19,'lineColor','m','linewidth',2','DisplayName','CSL 19')
hold off
print('GrainBoundaries_CSLmap_N205DF_Area10_Compiled_OpenXY','-
dtiffn','-r0')
%$%$%$%$%$%$%$%$%$%$%$%
%*%*%*%*%*%*%*%*%*%*%*
% This code matches Nick's and the code above for which grain
boundaries
% are CSL3
%Sigma 3 check
theta_3=60; % in degrees
directions_111=[1 1 1; -1 1 1; 1 -1 1; 1 1 -1; -1 -1 1; -1 1 -1; 1 -1 -
1;-1 -1 -1];
```

```
rot_3=rotation('axis',Miller(1,1,1,grains('Generic
BCC').CS),'angle',60*degree);
ind_3=angle(gB_Nb.misorientation,rot_3)<8.67*degree;
for i=1:length(directions_111)
rotTemp_3=rotation('axis',Miller(directions_111(i,1),directions_111(i,2
),directions_111(i,3),grains('Generic
BCC').CS),'angle',theta_3*degree);
indTemp_3=angle(gB_Nb.misorientation,rotTemp_3)<8.67*degree;
indComb_3=ind_3+indTemp_3;
end
for p=1:size(indComb_3,1)
    if indComb_3(p)==0
        indComb_3(p)=0;
    else
        indComb_3(p)=1;
    end
end
indLog_3=logical(indComb_3);

figure                                                          %Figur
e 16
plot(gB_Nb)
hold on
plot(gB_Nb(indLog_3),'lineWidth',2,'lineColor','r')
hold off
%legend('<10^\circ','27^\circ/[110]')
set(0,'defaultfigurepaperpositionmode','auto')
print('GrainBoundaries_CSL3_N205DF_Area10_Compiled_OpenXY','-dtiffn','-
r0')
%*%*%*%*%*%*%*%*%*%*%*%*
%#%#%#%#%#%#%#%#%#%#%#%#
% Calculate CSL19 boundaries
theta_19=27; % in degrees
directions_110=[1 1 0; -1 1 0; 1 -1 0; -1 -1 0; 1 0 1; -1 0 1; 1 0 -1;
-1 0 -1; 0 1 1; 0 -1 1; 0 1 -1; 0 -1 -1];
rot_19=rotation('axis',Miller(1,1,0,grains('Generic
BCC').CS),'angle',theta_19*degree);
ind_19=angle(gB_Nb.misorientation,rot_19)<3.441*degree;
for i=1:length(directions_110)
rotTemp_19=rotation('axis',Miller(directions_110(i,1),directions_110(i,
2),directions_110(i,3),grains('Generic
BCC').CS),'angle',theta_19*degree);
indTemp_19=angle(gB_Nb.misorientation,rotTemp_19)<3.441*degree;
indComb_19=ind_19+indTemp_19;
end
for p=1:size(indComb_19,1)
    if indComb_19(p)==0
        indComb_19(p)=0;
    else
        indComb_19(p)=1;
    end
end
indLog_19=logical(indComb_19);
```

```
figure                                                          %Figur
e 17
plot(gB_Nb)
hold on
plot(gB_Nb(indLog_19),'lineWidth',2,'lineColor','r')
hold off
%legend('<10^\circ','27^\circ'/[110]')
set(0,'defaultfigurepaperpositionmode','auto')
print('GrainBoundaries_CSL19_N205DF_Area10_Compiled_OpenXY','-
dtiffn','-r0')
%#%#%#%#%#%#%#%#%#%#%#%#
%@%@%@%@%@%@%@%@%@%@%@%@
% Calculate the boundaries that Lucke observes
theta_Lucke=35; % in degrees
%directions_110=[1 1 0; -1 1 0; 1 -1 0; -1 -1 0; 1 0 1; -1 0 1; 1 0 -1;
-1 0 -1; 0 1 1; 0 -1 1; 0 1 -1; 0 -1 -1];
rot_Lucke=rotation('axis',Miller(1,1,0,grains('Generic
BCC').CS),'angle',theta_Lucke*degree);
ind_Lucke=angle(gB_Nb.misorientation,rot_Lucke)<3.441*degree;
for i=1:length(directions_110)
rotTemp_Lucke=rotation('axis',Miller(directions_110(i,1),directions_110
(i,2),directions_110(i,3),grains('Generic
BCC').CS),'angle',theta_Lucke*degree);
indTemp_Lucke=angle(gB_Nb.misorientation,rotTemp_Lucke)<3.441*degree;
indComb_Lucke=ind_Lucke+indTemp_Lucke;
end
for p=1:size(indComb_Lucke,1)
    if indComb_Lucke(p)==0
        indComb_Lucke(p)=0;
    else
        indComb_Lucke(p)=1;
    end
end
indLog_Lucke=logical(indComb_Lucke);

figure                                                          %Figur
e 18
plot(gB_Nb)
hold on
plot(gB_Nb(indLog_Lucke),'lineWidth',2,'lineColor','r')
hold off
%legend('<10^\circ','27^\circ'/[110]')
set(0,'defaultfigurepaperpositionmode','auto')
print('GrainBoundaries_Lucke_N205DF_Area10_Compiled_OpenXY','-
dtiffn','-r0')

% plot ROD map
figure                                                          %Figur
e 19
plot(ebsd_Hraw(grains_Hraw),
ebsd_Hraw(grains_Hraw).mis2mean.angle./degree, 'colorrange',[0,13])
hold on
```

```
plot(grains.boundary,'linewidth',2)
mtexColorbar
set(0,'defaultfigurepaperpositionmode','auto')
print('ROD_N205DF_Area10_Compiled_OpenXY','-dtiffn','-r0')
hold off

%% Select grains with a certain orientation
% % want to use the data set that excludes boundary grains
% % restict to the "Fe" phase
% grainsNB_fe=grainsNB('Fe')
% %the reference orientation
% % ori=orientation('Miller',[111],[110],grains('Fe').CS,SS)
% % Define the {111}<110> orientation
% ori=orientation('Euler',0*degree,54.7356*degree,45*degree,
grainsNB('Fe').CS)
% % Define the {111}<112> orientation
% %ori=orientation('Euler',90*degree,54.7356*degree,45*degree,
grainsNB('Fe').CS)
%
grains_selected=grainsNB_fe(angle(grainsNB_fe.meanOrientation,ori)<15*d
egree)
% figure
% plot(grains_selected)
% % figure
% % hist(grains_selected)
% %d_111_110=grains_selected.diameter();
% %dlmwrite('d_111_110.txt',d_111_110,'delimiter','\t')
%
% % Define the (111)<011> orientation
% ori2=orientation('Euler',60*degree,54.7356*degree,45*degree,
grainsNB('Fe').CS)
%
grains_selected2=grainsNB_fe(angle(grainsNB_fe.meanOrientation,ori2)<15
*degree)
% figure
% plot(grains_selected2)
%
% % Define the (1n11)<110> orientation
% ori3=orientation('Euler',0*degree,54.7356*degree,135*degree,
grainsNB('Fe').CS)
% % Define the {111}<112> orientation
% %ori=orientation('Euler',90*degree,54.7356*degree,45*degree,
grainsNB('Fe').CS)
%
grains_selected3=grainsNB_fe(angle(grainsNB_fe.meanOrientation,ori3)<15
*degree)
% figure
% plot(grains_selected3)

% find all the variants of the {111}<110>
%oriS=symmetrise(ori,'antipodal')
% for i=1:length(oriS)
%     i
```

```
%     oriS(i)
%
grains_selected=grainsNB_fe(angle(grainsNB_fe.meanOrientation,oriS(i))<
15*degree)
%     figure
%     plot(grains_selected)
%     i=i+1;
% end

%
grains_selected=grainsNB_fe(angle(grainsNB_fe.meanOrientation,ori)<15*d
egree)
% figure
% plot(grains_selected)
% figure
% hist(grains_selected)
% d_111_110=grains_selected.diameter();
% dlmwrite('d_111_110.txt',d_111_110,'delimiter','\t')
%
% %the reference orientation
% ori=orientation('Miller',[111],[110],grains('Fe').CS,SS)
% ori_111_011=orientation('Euler',60*degree,54.7356*degree,45*degree,
grainsNB('Fe').CS)
% % select all grains with orientation angle to ori less than 15 degree
% %oriS=symmetrise(ori_111_011,'antipodal')
%
grains_111_011=grainsNB_fe(angle(grainsNB_fe.meanOrientation,ori_111_01
1)<15*degree)
% figure
% plot(grains_111_011)
% figure
% hist(grains_111_011)
% d_111_011=grains_111_011.diameter();
% dlmwrite('d_111_011.txt',d_111_011,'delimiter','\t')
%
% %the reference orientation
% % ori=orientation('Miller',[111],[110],grains('Fe').CS,SS)
% ori_11n1_110=orientation('Euler',0*degree,125.2644*degree,45*degree,
grainsNB('Fe').CS)
% % select all grains with orientation angle to ori less than 15 degree
% oriS=symmetrise(ori_11n1_110,'antipodal')
%
grains_11n1_110=grainsNB_fe(angle(grainsNB_fe.meanOrientation,ori_11n1_
110)<15*degree)
% figure
% plot(grains_11n1_110)
% figure
% hist(grains_11n1_110)
% d_11n1_110=grains_11n1_110.diameter();
% dlmwrite('d_11n1_110.txt',d_11n1_110,'delimiter','\t')

% figure
% hist(grains)
```

```
% d_all=grains.diameter()
% dlmwrite('d_all.txt',d_all,'delimiter','\t')

% the reference orientation
% ori=orientation('Miller',[111],[110],grains('Fe').CS)
% oriS=symmetrise(ori,'antipodal')
% % select all grains with orientation angle to ori less than 15 degree
%
grains_selected=grains_fe(angle(grains_fe.meanOrientation,oriS)<15*degr
ee)
% plot(grains_selected)
%%
%%%%%%%%%%%%%%%%%%%%%%%%%%%%%%%%%%%%%%%%%%%%%%%%%%%%%%%%%%%%%%%%%%%%%%%
%%%%
%%%%%%%%%%%%%%%%%%%%%%%%%%%%%%%%%%%%%%%%%%%%%%%%%%%%%%%%%%%%%%%%%%%%%%%
%%%%
%%%%%%%%%%%%%%%%%%%%%%%%%%%%%%%%%%%%%%%%%%%%%%%%%%%%%%%%%%%%%%%%%%%%%%%
%%%%
%%%%%%%%%%%%%%%%%%%%%%%%%%%%%%%%%%%%%%%%%%%%%%%%%%%%%%%%%%%%%%%%%%%%%%%
%%%%
% % remove grains containing less than a critical number of indexed
points
% min_g_size=5
% selected_grains=grains(grains.grainSize>min_g_size);
% removed_grains=grains(grains.grainSize<min_g_size)
% ebsdG(removed_grains)=[]

% remove grains containing less than a critical number of indexed
points
% min_g_size=5
% selected_grains=grains(grains.grainSize>min_g_size);
% removed_grains=grains(grains.grainSize<min_g_size)
% ebsdG(removed_grains)=[]

%remove grains containing less than a critical number of indexd points
%minGsize=5;
%toRemove=grains.grainSize<minGsize;
%selected_grains=grains(grains.grainSize>min_g_size);`
%removed_grains=grains(grains.grainSize<minGsize)
%ebsd_Hraw(removed_grains)=[]
%selected_grains=grains(grains.grainSize>5);
%ebsd_HrawCor=ebsd_Hraw.grinID,ebsd_Hraw.mis2mean]=calcGrains(ebsd_Hraw
Cor('indexed'),'angle',5*degree)

%number of small grains removed from all phase
%number_of_small_grains_removed=number_of_calcGrains-
selected_grains.length
%[grains,ebsd_Hraw.grainId]=calcGrains(ebsdHraw,'angle',5*degree)

% figure
% plot(ebsd_HrawCor)
% hold on
% plot(grains.boundary,'linewidth',2)
```

```
% hold off

%% Plot Pole figure of the raw
Nb_N205DF_Area10_Compiled_OpenXY_20190730 EBSD Data
% T = 1500C, annealed for 67 min
% x = TD  y = TLTD(RD) z = STD

%plotting convention
setMTEXpref('xAxisDirection','east');
setMTEXpref('zAxisDirection','outOfPlane');

% % plotting convention
% setMTEXpref('xAxisDirection','east'); TLTD (RD)
% setMTEXpref('zAxisDirection','outOfPlane'); STD

cs_Hraw=ebsd_Hraw('Generic BCC').CS;
h_Hraw = [Miller(1,0,0, cs_Hraw), Miller(1,1,0, cs_Hraw), Miller(1,1,1,
cs_Hraw)];

% Pole Figure no color
figure                                                              %
Figure 20
plotPDF(ebsd_Hraw('Generic BCC').orientations,h_Hraw,
'antipodal','all','MarkerSize',1)
annotate(xvector,'label',{'TD'})
annotate(yvector,'label',{'TLTD (RD)'})
set(0,'defaultfigurepaperpositionmode','auto')
print('PF_Hraw_N205DF_Area10_Compiled_OpenXY','-dtiffn','-r0')

% Pole Figure with color bar (contour plots)
figure                                                              %
Figure 21
plotPDF(ebsd_Hraw('Generic
BCC').orientations,h_Hraw,'colorrange',[0,5], 'contourf',
'antipodal','all','MarkerSize',1)
annotate(xvector,'label',{'TD'})
annotate(yvector,'label',{'TLTD(RD)'})
CLim(gcm, 'equal')
mtexColorbar
set(0,'defaultfigurepaperpositionmode','auto')
print('PF_Hraw_colorbar_N205DF_Area10_Compiled_OpenXY','-dtiffn','-r0')

%% Plot Inverse Pole Figure of the
Nb_N205DF_Area10_Compiled_OpenXY_20190801 EBSD Data
%plotting convention
setMTEXpref('xAxisDirection','east');
setMTEXpref('zAxisDirection','outOfPlane');

%use raw crystal symmetry
figure                                                              %
Figure 22
plotIPDF(ebsd_Hraw('Generic BCC').orientations,[xvector, yvector,
zvector], 'antipodal','all','MarkerSize',1)
```

```
annotate([Miller(1,0,0,cs_Hraw),Miller(1,1,0,cs_Hraw),Miller(1,1,1,cs_H
raw)],'symmetrised','labeled','BackgroundColor','w','textAboveMarker')
set(0,'defaultfigurepaperpositionmode','auto')
print('IPF_Hraw_N205DF_Area10_Compiled_OpenXY','-dtiffn','-r0')

%use raw crystal symmetry with colorbar (contour plots)
figure                                                              %
Figure 23
plotIPDF(ebsd_Hraw('Generic BCC').orientations,[xvector, yvector,
zvector], 'colorrange',[0,13], 'contourf',
'antipodal','all','MarkerSize',1)
CLim(gcm, 'equal')
mtexColorbar
annotate([Miller(1,0,0,cs_Hraw),Miller(1,1,0,cs_Hraw),Miller(1,1,1,cs_H
raw)],'symmetrised','labeled','BackgroundColor','w','textAboveMarker')
set(0,'defaultfigurepaperpositionmode','auto')
print('IPF_Hraw_colorbar_N205DF_Area10_Compiled_OpenXY','-dtiffn','-
r0')

%% Calculate ODF of the Nb_N205DF_Area10_Compiled_OpenXY_20190801 EBSD
Data

odf_Hraw=calcODF(ebsd_Hraw('Generic BCC').orientations)

%% Plot pole figures from ODF of the
Nb_N205DF_Area10_Compiled_OpenXY_20190801 EBSD data
odf_Hraw.SS=specimenSymmetry('orthorhombic')
cs_odfHraw=odf_Hraw.CS
h_odfHraw=[Miller(1,0,0, cs_odfHraw), Miller(1,1,0, cs_odfHraw),
Miller(1,1,1, cs_odfHraw)];

% plotting convention
setMTEXpref('xAxisDirection','east');
setMTEXpref('zAxisDirection','outOfPlane');

% % this is for plotting the Pole Figure for "rotated" data
% figure
% plotPDF(odf_Hrot,h_odfHrot,'antipodal','complete')
% colorbar
% annotate(xvector,'label',{'RD'})
% annotate(yvector,'label',{'LTD'})
% set(0,'defaultfigurepaperpositionmode','auto')
% print('odfPF_Hrot_N205DF_Area10_Compiled_OpenXY','-dtiffn','-r0')

% The way this plots is strange. I think it plots both upper and
% lower spheres, with the order:
% (100) upper (100) lower (110) upper
% (110) lower (111) upper (111) lower


% x = TD  y = TLTD(RD) z = STD
figure                                                              %
Figure 24
```

```
plotPDF(odf_Hraw,h_odfHraw,'colorrange',[0,5],'antipodal','complete','u
pper')
annotate(xvector,'label',{'TD'})
annotate(yvector,'label',{'TLTD(RD)'})
CLim(gcm, 'equal')
mtexColorbar
set(0,'defaultfigurepaperpositionmode','auto')
print('PF_odfHraw_N205DF_Area10_Compiled_OpenXY','-dtiffn','-r0')

%% Plot Inverse Pole Figure of ODF of the
Nb_N205DF_Area10_Compiled_OpenXY_20190801 EBSD Data
% plotting convention
setMTEXpref('xAxisDirection','east');
setMTEXpref('zAxisDirection','outOfPlane');

figure                                                              %
Figure 25
plotIPDF(odf_Hraw,[xvector, yvector,
zvector],'colorrange',[0,13],'antipodal')
CLim(gcm, 'equal')
mtexColorbar
annotate([Miller(1,0,0,cs_odfHraw),Miller(1,1,0,cs_odfHraw),Miller(1,1,
1,cs_odfHraw)],'colorrange',[0,13],
'symmetrised','labeled','BackgroundColor','w','textAboveMarker')
set(0,'defaultfigurepaperpositionmode','auto')
print('odfIPF_Hraw_N205DF_Area10_Compiled_OpenXY','-dtiffn','-r0')
%% Plot Euler Slice
figure                                                              %
Figure 26
plot(odf_Hraw,'phi2',[45]*degree,'contourf','silent', 'colorrange',[0,
25])
mtexColorbar
set(0,'defaultfigurepaperpositionmode','auto')
print('EulerSpace_Hraw_N205DF_Area10_Compiled_OpenXY','-dtiffn','-r0')
```

References

[1] T. H. Schofield: *J. Inst. Met.*, 1956, vol. 85, pp. 372–74.

[2] J. B. Lambert and J. J. Rausch: *Prop. Sel. Nonferrous Alloy. Spec. Mater.*, 2018, vol. 2, pp. 557–85.

[3] W. Chang: in *Refract. Met. Alloy.*, J.J. Semchyshen, M. and Harwood, ed., Metallurgical Society of AIME, 1958, pp. 83–117.

[4] G.D. Gemmel: in *Metall. Columbium Its Alloy.*, AIME, 1958.

[5] J. Weertman: *Nav. Res. Lab Repot 5123*, 1958.

[6] A. N. Behera, R. Kapoor, A. Sarkar, and J. K. Chakravartty: *Energy Mater. Mater. Sci. Eng. Energy Syst.*, 2014, vol. 9, pp. 637–44.

[7] G. Brinson and B.B. Argent: *J. Inst. Met.*, n.d., vol. 91, pp. 293–98.

[8] J.D.W. Rawson and B.B. Argent: *J. Inst. Met.*, 1967, vol. 95, pp. 212–16.

[9] M. J. Klein and M.E. Gulden: *Metall. Trans.*, 1973, vol. 4, pp. 2175–80.

[10] Robert A. Schwarzer and Jarle Hjelen: *Micros. Today*, 2015, vol. 23, pp. 12–17.

[11] Angus J. Wilkinson: *Scr. Mater.*, 2001, vol. 44, pp. 2379–85.

[12] D.A. Molodov: *Microstructual Design of Advanced Engineering Materials*, John Wiley & Sons, 2013.

[13] P. J. Noell: The University of Texas at Austin, 2014.

[14] J.P. Poerier: *Creep of Crystals: High-Temperature Deformation Processes in Metals, Ceramics and Minerals*, Cambridge University Press, 1985.

[15] D.J. Dingley: *Anal. Par Diffr. Des Electrotrons Retrodiffuses*, 2015, pp. 217–76.

[16] T. Japel: Rheinish-Westfalischen Tehcnischen Hochschule Aachen, 2014.

[17] CrossCourt: *Http://Www.Hrebsd.Com/Wp/Crosscourt/*, n.d.

[18] BYU Microstructure of Materials Group: n.d.

[19] ASTM: *ASTM B393-18*, 2015, vol. 03, pp. 14–17.

[20] F. Bachmann, R. Hielscher, and H. Schaeben: 2021.

[21] E.A.D. Brady and E.M. Taleff: *Metall. Mater. Trans. A Phys. Metall. Mater. Sci.*, 2021, vol. 52, pp. 1095–1105.

[22] J. Stoop and P. Shahinian: *Rep. No. NRL-6095*, 1964, pp. 407–32.

[23] J. Stoop and P. Shahinian: *Rep. No. NRL-6464*, 1966, pp. 1–15.

[24] A. C. Lewis, D. van Heerden, C. Eberl, K. J. Hemker, and T. P. Weihs: *Acta Mater.*, 2008, vol. 56, pp. 3044–52.

[25] D. P. Gregory and G. H. Rowe: *Columbium Metall. AIME Metall. Soc. Conf.*, 1960, vol. 10, pp. 309–41.

[26] C. R. Tottle: *J. Inst. Met.*, 1956, vol. 85, pp. 375–78.

[27] L.R. Williams and T. J. Heal: *Met. Plansee Proceedings1*, 958, vol. F. Benesov, pp. 350–70.

[28] T. J. Heal: *Second United Nationa Int. Conf. Peac. Uses At. Energy1*, 958, pp. 208–19.

[29] M. J. Davidson, M. Biberger, and A. K. Mukherjee: *Scr. Metall.*, 1992, vol. 27, pp. 1829–34.

[30] Plansee: *Https://Www.Plansee.Com/En/Materi%0Aals/Niobium.Html*, n.d.

[31] ASTM INTERNATIONAL: *ASTM E112-10*, 2010, pp. 1–27.
[32] O. D. Sherby and P.M. Burke: *Prog. Mater. Sci.*, 1968, vol. 13, pp. 325–90.
[33] J. Ciulik and E. M. Taleff: *Scr. Mater.*, 2009, vol. 61, pp. 895–98.
[34] Daniel L. Worthington, Nicholas A. Pedrazas, Philip J. Noell, and Eric M. Taleff: *Metall. Mater. Trans. A Phys. Metall. Mater. Sci.*, 2013, vol. 44, pp. 5025–38.
[35] Nicholas A. Pedrazas, Thomas E. Buchheit, Elizabeth A. Holm, and Eric M. Taleff: *Mater. Sci. Eng. A*, 2014, vol. 610, pp. 76–84.
[36] Philip J. Noell, Daniel L. Worthington, and Eric M. Taleff: *Metall. Mater. Trans. A Phys. Metall. Mater. Sci.*, 2015, vol. 46A, pp. 5708–18.
[37] Philip J. Noell and Eric M. Taleff: *JOM*, 2015, vol. 67, pp. 2642–45.
[38] O.A. Ruano and O.D. Sherby: *Rev. Phys. Appl.*, 1988, vol. 23, pp. 625–37.
[39] M.E. Kassner: *Fundamentals of Creep in Metals and Alloys*, Butterworth Heinemann, Wal Tham, MA, 2015.
[40] P.E. Armstrong and H.L. Brown: *Trans. ASM*, 1965, vol. 58, pp. 30–37.
[41] D.J. Livesey: *J. Inst. Met.*, 1959, vol. 88, p. 144.
[42] M. B. Reynolds: *Trans. ASM*, 1953, vol. 45, pp. 839–61.
[43] H. A. Wriedt and R. A. Oriani: *Scr. Mater.*, 1974, vol. 8, pp. 203–8.
[44] D. P. Laverty and E. B. Evans: *Columbium Metall. AIME Metall. Soc. Conf.*, 1960, vol. 10, pp. 299–307.
[45] J. J. Harwood: *Aircr. Missiles*, 1958, pp. 32–38.
[46] W. S. Hazelton: *Aircr. Missiles*, 1958, pp. 41–45.
[47] Colin James Smithells: *Smithells Metals Reference Book*, 2004.
[48] Landolt-Bornstein: *No Title*, New Series, Springer-Verlag, Berlin, 1969.
[49] E. Walker and M. Peter: *J. Appl. Phys.*, 1977, vol. 48, pp. 2820–26.
[50] D. M. Schlader and J. F. Smith: *J. Appl. Phys.*, 1977, vol. 48, pp. 5062–66.
[51] A .I. Artemov, A .E. Kissil, E. M. Lyutyi, and O. S. Zvikilevich: 1983, vol. 1, pp. 14–17.
[52] C. Zener and J.H. Hollomon: *J. Appl. Phys.*, 1944, vol. 15, pp. 22–32.
[53] ASTM B392-18: *Standard Specification for Niobium and Niobium Alloy Bar , Rod , and Wire*, ASTM International, West Conshokocken, PA, 2018.
[54] E.A.D. Brady and E.M. Taleff: *Metall. Mater. Trans. A Phys. Metall. Mater. Sci. Submitt. Rev.*, 2021.
[55] E. Orowan: in *Symp. Intern. Stress. Met. Alloy.*, Institue of Metals, London, 1948.
[56] J.C. Fisher, E.W. Hart, and R.H. Pry: *Acta Metall.*, 1953, vol. 1.
[57] Ralph Hielscher: *MTEX Github, Https//Github.Com/Mtex-Toolbox/Mtex/Blob/Develop/EBSDAnalysis/@EBSD/Fill.M*, n.d.
[58] T. R. McNelley, K. Oh-Ishi, A. P. Zhilyaev, S. Swaminathan, P.E. Krajewski, and E.M. Taleff: *Metall. Mater. Trans. A Phys. Metall. Mater. Sci.*, 2008, vol. 39, pp. 50–64.
[59] S.R. Shatynski: *Oxid. Met.*, 1979, vol. 13, pp. 105–18.
[60] O. D. Sherby, R. H. Klundt, and A. K. Miller: *Metall. Mater. Trans. A*, 1977, vol. 8, pp. 843–50.
[61] Ya. S. Malakhov and G. V. Samsonov: *Poroshkovaya Metall.*, 1966, pp. 84–91.

[62] F. A. Mohamed and T. G. Langdon: *Acta Metall.*, 1974, vol. 22, pp. 779–88.
[63] W.R. Cannon and O.D. Sherby: *Metall. Mater. Trans. A Phys. Metall. Mater. Sci.*, 1970, vol. 1, pp. 1030–32.
[64] MathWorks: *Https://Www.Mathworks.Com/Products/Matlab.Html*, n.d.
[65] C. Colliex, J. M. Cowley, S. L. Dudarev, M. Fink, J. Gjonnes, R. Hilderbrandt, A. Howie, D. F. Lynch, L.M. Peng, G Ren, A. W. Ross, V. H. Smith Jr, J. C. H. Spence, J. W. Steeds, J. Wang, M. J. Whelan, and B. B. Zvyagin: *Int. Tables Crystallogr.*, 2006, vol. C, pp. 259–429.
[66] B. D. Cullity: *Elements of X-Ray Diffraction*, 2nd ed., Pearson, 1978.
[67] ImageJ: *Https://Imagej.Nih.Gov/Ij/*, n.d.

Vita

Emily Brady graduated in the top ten of her class in 2013 class from Stony Point High School in Round Rock, Texas. She started at the University of Texas at Austin in Mechanical Engineering in the fall of 2013. A summer internship at Austin Energy and the Materials Science class in her undergraduate curriculum sparked Emily's interest in materials science. She graduated in 2017 with honors, during her undergraduate Emily worked in the Maker Studio (now called Texas InnovationWorks) and also participated in undergraduate research in Dr. Wei Li's group and Dr. Eric Taleff's group. She started her graduate degree at the Texas Materials Institute at the University of Texas at Austin in Dr. Eric Taleff's group in the fall of 2017. Emily is the first in her family to earn a Doctorate in Philosophy. She will work as an Associate in the Mechanical Engineering team at Exponent Engineering Consulting in their Houston office after graduation.

Email address: emily.dukes@utexas.edu

This dissertation was typed by Emily Ann Dukes Brady.